Universiteit Utrecht

MAJOR ROTATION DIFFERENCE ALONG THE "MID-CYCLADIC LINEAMENT" ON PAROS, CENTRAL GREECE

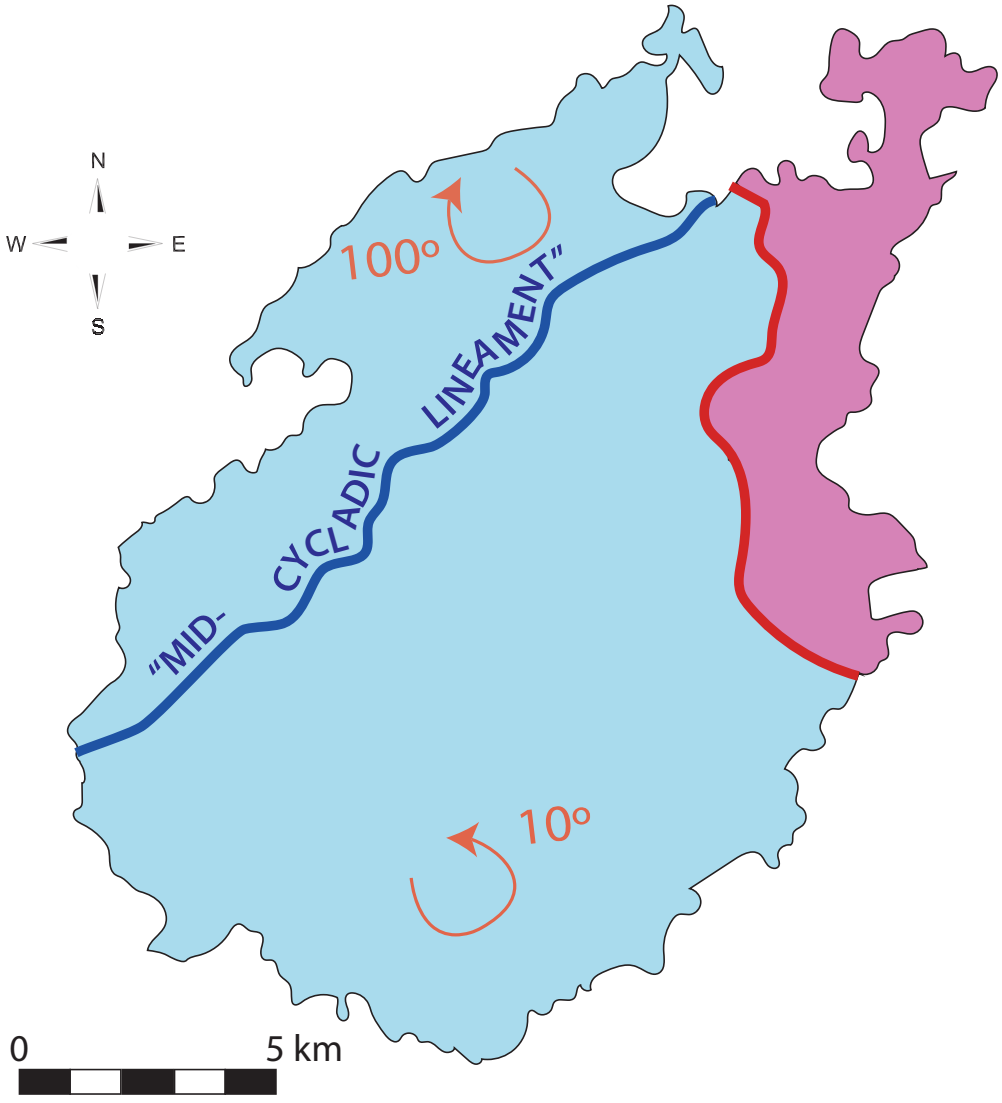

MSc student Christina Malandri 3736733

Supervisors Dr. D. van Hingsbergen, Dr. L. Kriegsman, Dr. K. Soukis

TABLE OF CONTENTS

LIST OF ABBREVIATIONS

AF	Alternating field
AMS	Anisotropy of the magnetic susceptibility
CBU	Cycladic Blue Schists
ChRM	Characteristic remnant magnetization
F	Magnetic foliation
HP	High pressure
LT	Low temperature
MCL	Mid Cycladic Lineament
PT	Pressure-Temperature
VGP	Virtual Geomagnetic Pole

Mineral abbreviations based on Whitney and Evans, 2010

PART 1: INTRODUCTION

1.1 Introduction

Studying and recording the dynamics and kinematics of the tectonic plates has, since the 60s, been one of the major issues when approaching the geological history of our planet. Spectacular mountain ranges, volcanic arcs and renewed oceanic crust are formed, progressively subducted into the mantle and eventually partly exhumed back to the surface as a consequence of the global tectonic motions. Reconstructing the tectono-metamorphic evolution of an area contributes to explain geological processes back in time.

The Cycladic islands (central Aegean region) (Fig. 1.1), widely known for their well-preserved metamorphic rocks, provide one of the most appropriate locations to study the burial and exhumation history of rocks at a subduction contact, through analysis of their metamorphism and tectonic history.

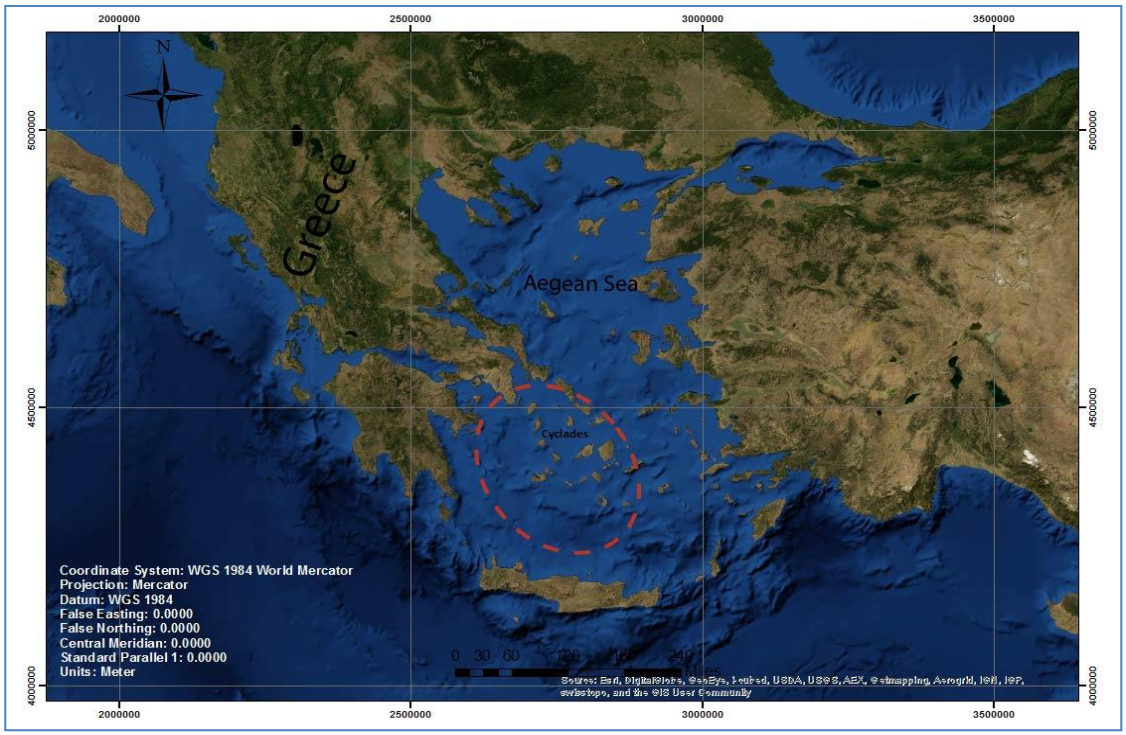

Figure 1.1: Location of Cyclades, Greece (source: CGIARCSI, Srtm 90m digital elevation Database v4.1, srtm 42_05).

The Cyclades lay upon the Hellenic orogenic Belt which comprises a previously stacked nappe pile, reworked and exhumed in in two different stages in extensional metamorphic complexes (Ring et al., 2007; Jolivet et al., 2010; Philipon et al., 2010). The first stage involved exhumation due to decompression, with no any clear surface expression and occurred from 25 to 15 Ma (Jolivet et al., 2003; Ring et al., 2010; van Hinsbergen and Schmid 2012). During the second stage, after 15 Ma, the underthrusted nappes exhumed along major detachment faults as a result of crustal thinning (Lister et al., 1999; Jolivet et al., 2003). The most noticeable feature of the later stage is the

different orientations of the stretching lineations characterizing the northwestern and the southeastern part of the Cyclades.

The sudden change in orientation of the lineations in the Cycladic metamorphic units remains a puzzling feature though. From the present paleomagnetic evidence, it follows this transition should correspond to the tectonic border between two oppositely rotating blocks, each with their own stretching lineation directions. The boundary between these two domains is defined by a conceptual line known as "Mid Cycladic Lineament" (Walcott and White, 1998) (Fig.1.2). The kinematic restoration of rotations and extension of the Aegean region showed that no curved extensional back-arc can form without arc-parallel extension (van Hinsbergen and Schmid, 2012) and an extensional nature for the Mid-Cycladic Lineament was therefore proposed by these authors. Although the necessity of such structure is being supported by structural (observed systematic change in stretching lineations) and paleomagnetic indications (recorded opposite rotational directions), a pronounced structure to confirm its presence in the field has not been discovered so far.

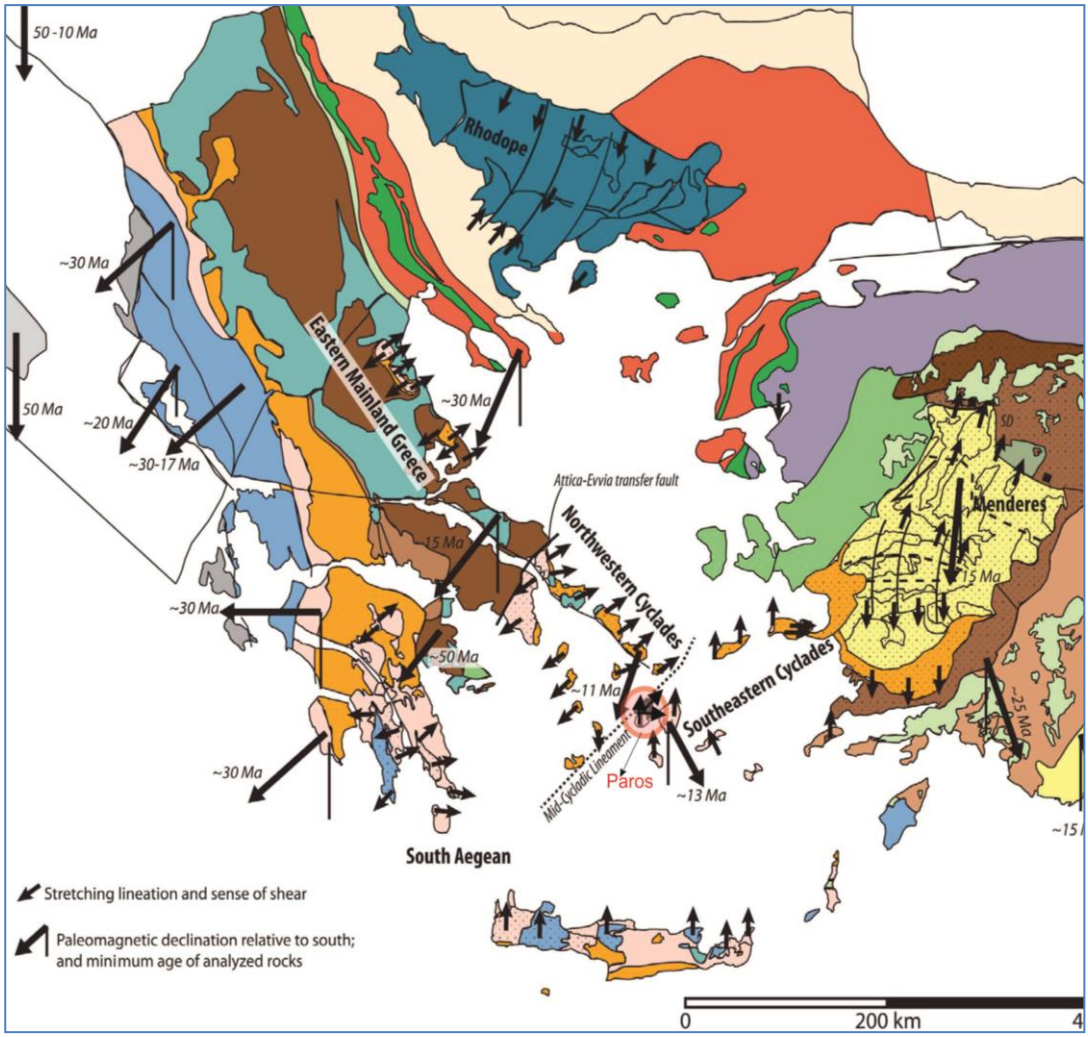

Figure 1.2: Geological map of Greece indicating the patterns of stretching lineations (small arrows) and the paleomagnetic declinations (large arrows) as they have been recorded in metamorphic core complexes. The lineation patterns striking NE-SW while there is a change in their strike direction to N-S, passing through the island of Paros (red marked area). Also as it is obvious there are no paleomagnetic indications concerning the island of Paros. The dotted line on the map represents the schematic illustration of the "Mid Cycladic

Therefore, I attempted to decipher whether such a border corresponds to an actual structure on the only island of the Cyclades where both stretching lineation trends has been identified: Paros. The aim of this study is two-fold: First, I aim to investigate whether the change of the stretching lineations on Paros is the result of post-formational vertical axis rotations, or reflect two different generations of formation. To achieve, the paleomagnetic declinations as well as the magnetic lineations of the sampled rocks are obtained and compared with orientations of the stretching lineations. Second, I aim to examine the possible structures of the island (low angle detachment faults) that could accommodate the vertical axis rotation. For this purpose, petrological analysis will be performed in order to determine any metamorphic gap between the mapped hanging wall and footwall sequences of the detachments as they exposed in Paros, suggesting that there is indeed a border separating two different domains represented by different metamorphic regimes. To this end, I collected samples from Miocene granites that intruded the metamorphic rocks of Paros for the paleomagnetic study and rock samples from different parts of the island for petrological analysis. Finally the results are developed in context of the role of the "Mid-Cycladic lineament" in the kinematic evolution of the Aegean Region, testing the "opening" scenario between two different rotated blocks as speculated by van Hinsbergen and Schmid (2012).

1.2 Geological setting

Geological setting of Cyclades

A sequence of contraction and burial followed by extension and exhumation has shaped the Aegean geology active from Mesozoic to recent times (Dewey et al., 1989; Faccena and Becker 2010; Ring et al., 2010; van Hinsbergen and Schmid, 2012). The onset of progressive convergence and subduction of the Adriatic-African plate beneath Eurasia started in Cretaceous times, and resulted in the development of a crustal accretionary wedge forming the Hellenic orogenic Belt. The build-up of the Hellenic Belt comprises a previously stacked pile of continental and oceanic units that was subsequently underthrusted, accompanied by high pressure metamorphism during their burial (van Hinsbergen et al., 2005b ;Ring et al., 2007; Jolivet et al., 2010; Phillipon et al., 2012). The Hellenic Belt composes an elongated NNW-SSE trending, WSW-verging thin-skinned fold-thrust belt (van Hinsbergen et al., 2005a; Vanderhaeghe et al., 2007), involving the following units from northeast to southwest **(Fig.1.3)**: a) Rhodope, b) Vardar- Axios, c) Pelagonian, d) Pindos, e) Gavrovo-Tripolitza, f) Ionian, and g) Pre-Apulia (Van Hinsbergen et al., 2005a; Ring et al., 2010; Kilias et al., 2010).

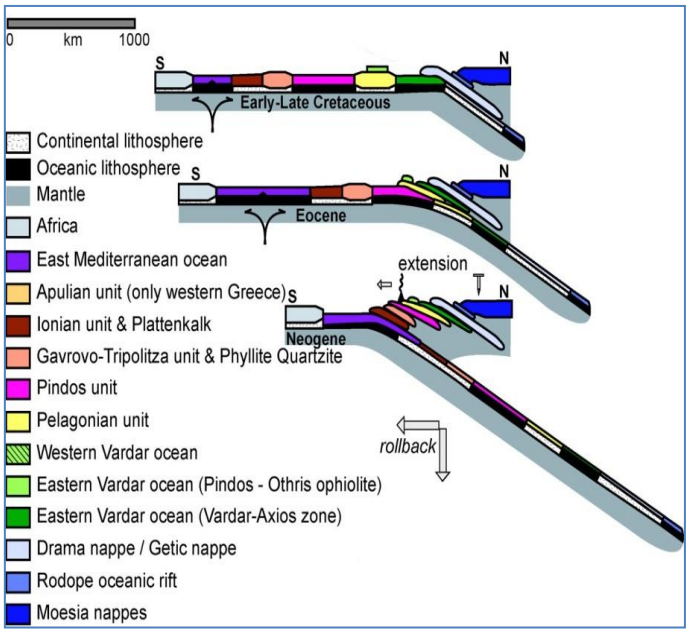

Figure 1.3: Depiction of nape accretion during the formation of the Hellenic Belt (van Hinsbergen et al., 2005a)

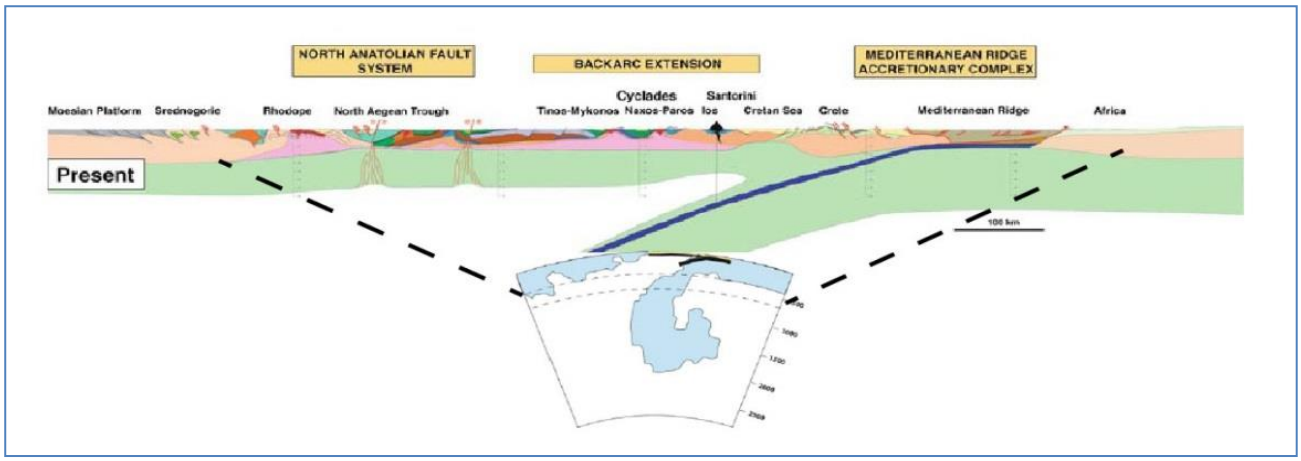

Figure 1.4: Cross section showing the ongoing extension in the Aegean region and tomographic picture showing the roll back of the subducted plate beneath the Aegean Sea (Jolivet and Brun 2008, after Bijwaard et al. 1998)

During the Late Eocene a radical change in the boundary conditions changed the tectonic framework in the Aegean region (Jolivet et al; 2001). Retreat of the subducted slab relative to Eurasia started to create extensional deformation in the overriding plate (Jolivet et al., 1999; Faccenna et al., 2003; van Hinsbergen and Schmid, 2012) (Fig.1.4). The extensional regime resulted in crustal thinning dominated by low-angle detachment faults and exhumation of the previously underthrusted nappes in extensional core complexes (Lister et al., 1985; Forster and Lister, 1999; Mehl et al., 2005; Jolivet et al., 2010). The exhumation of these metamorphic complexes occurred in two different stages (Foster and Lister 1999; van Hinsbergen et al., 2005b; Jolivet and Brun 2010).

The first stage involved exhumation of rocks buried under high-pressure- low-temperature metamorphic conditions during their underthrusting (Cycladic Blueschists), reaching pressures varying from 8-20 Kbar. HP blueschist to eclogite facies rocks are well preserved in the Cyclades, in areas away from the centers of core complexes, where PT conditions during exhumation were cool and deformation intensity was low (Avigad 2001; Jolivet et al., 2003; Ring et al., 2010). This first stage of decompression occurred without a clear surface expression or exhumation of metamorphic rocks to the surface (syn-orogenic extension) (Jolivet et al 2003; Tirel et al., 2009; Jolivet and Brun 2010), coevally with the subduction of the Pindos unit (Boven and Beccaletto 2007; Brun and Faccena 2008). In the second stage, exhumation of Cycladic Blueschists to the surface, took place along low-angle normal faults as a result of crustal thinning (post-orogenic extension) (Jolivet et al., 2003; jolivet and Brun 2010). During that stage asthenospheric upwelling led to an increase of the geothermal gradient and resulted in a high-temperature metamorphic overprint reaching in extreme cases to partial melting (migmatites) (Jansen and Schuiling 1976, Vanderhaeghe et al., 2007). Both stages are characterized by non – coaxial ductile deformation exemplified by a series of low angle detachment faults (Gautier and Brun 1994; Vandenberg and Lister 1996; Avigad et al, 2001). The first stage is associated with a top to the east sense of shear, while the second stage is defined by top to the north sense of shear (Gautier and Brun 1994; Jolivet 2001, Jolivet et al., 2010; Jolivet and Brun 2010). Extension in the Aegean region is

associated with ongoing widespread arc-related plutonic and volcanic activity, which follows the migrating trench southwards relative to Eurasia (Pe-Piper and Piper 2002). The final geometry and location of the various tectonostratigraphic units is related to the slow migration of the subduction front towards the African margin and the penetration of the large North Anatolian fault within the Aegean domain (Taymaz et al 1991; Jackson 1994; Mehl et al., 2004; Lacombe et al., 2013).

Tectonostratigraphy

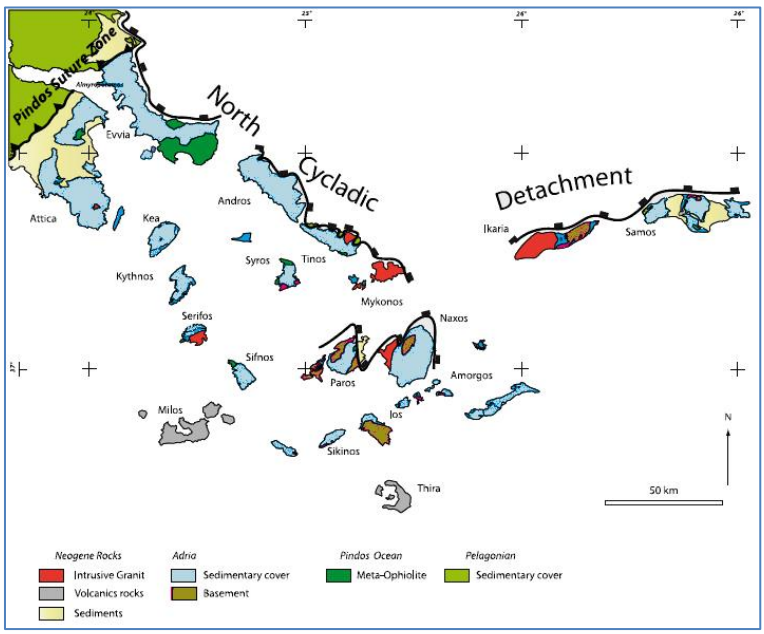

Figure 1.5: Geologicla interpretive map of the lithological units of Cyclades (after Phillipon et al., 2012)

In the central Aegean region (Cyclades) three main tectonic units have been recognized, from bottom to the top composed of the Basal Unit, the Cycladic Blueschists Unit (CBU) and the Upper Cycladic Nappe (Fig.1.5). The Basal Unit is composed of Triassic sedimentary sequences, overlain by Eocene neritic carbonates and flysch (Ring et al., 2010). A composite rock association, formed by metabasic rocks intercalated within metapelites and marbles, compose the CBU (Avigad and Garfunkel, 1991; Keiter et al., 2004; Bricheau et al., 2006). Sedimentary and volcanic protoliths show Triassic to Cretaceous ages (Bröcker and Pidgeon, 2007) and are generally considered as the lateral equivalent of the Pindos zone in the Hellenides (Bonneau, 1984). Furthermore according to lithostratigraphic and paleogeographic criteria the CBU can be subdivided in two parts, involving Pre-Alpine basement meta-sediments topped by deep marine volcano-sedimentary formation. The Basal Unit and the CBU are intruded by Miocene plutonic rocks that cut the regional foliation, but are deformed by exhumation related extensional detachments. These detachments separate the Basal Unit and the CBU from the Upper Cycladic nappe which is interpreted to be the equivalent of the Pelagonian unit, representing the overriding plate during Alpine underthrusting (Jolivet et al 2010; Ring et al., 2010; Bargnesi et al, 2012). It is a highly heterogeneous formation (Tectono-Sedimentary Unit) defined by Jurassic and Cretaceous ophiolithic rocks and Mesozoic marbles within an alternating sequences of pelitic and psammitic schists and gneisses (Buick and Holland, 1989; Ring et al., 1999; Jolivet et al., 2010).

Metamorphism

The Cycladic islands are characterized by a complex metamorphic evolution recording an early burial stage followed by a retrograde overprint (Altherr et al., 1979, 1982; Wijbrans and

McDougall, 1986; Wijbrans and McDougall, 1988). The Basal Unit and the CBU experienced an early Eocene subduction down to HP–LT conditions. The HP event is dated between 55 and 34 Ma with peak metamorphic conditions around 15–20 kbar and 550°C in the stability field of blueschist and eclogite (van Hinsbergen et al., 2005b; Ring et al., 2001; Laurent et al., 2015). This early event is quickly followed by a greenschist–facies overprint in the Oligocene–Miocene during a later exhumation stage recorded in the most external Cycladic islands (Okrusch eyt al., 1990; Trotet et al., 2001). In the center of the metamorphic dome (Paros and Naxos) the rise of the temperature reached amphibolitic to granulitic conditions resulting occasionally in partial melting and formation of migmatitic bodies (Jansen and Shuiling 1976; Buick and Holland, 1989; Vanderhaeghe 2004) in association with incipient presence of granitic intrusions (Altherr et al., 1982; Bröcker et al., 1993; Parra et al., 2002; Schliestedt et al., 1987; Keay et al., 2001) (Fig 1.6). The Upper Cycladic Unit comprises a non-to-low grade metamorphic unit, which was part of the upper crustal plate during Eocene subduction (Gautier and Brun 1994; Jolivet et al., 2001).

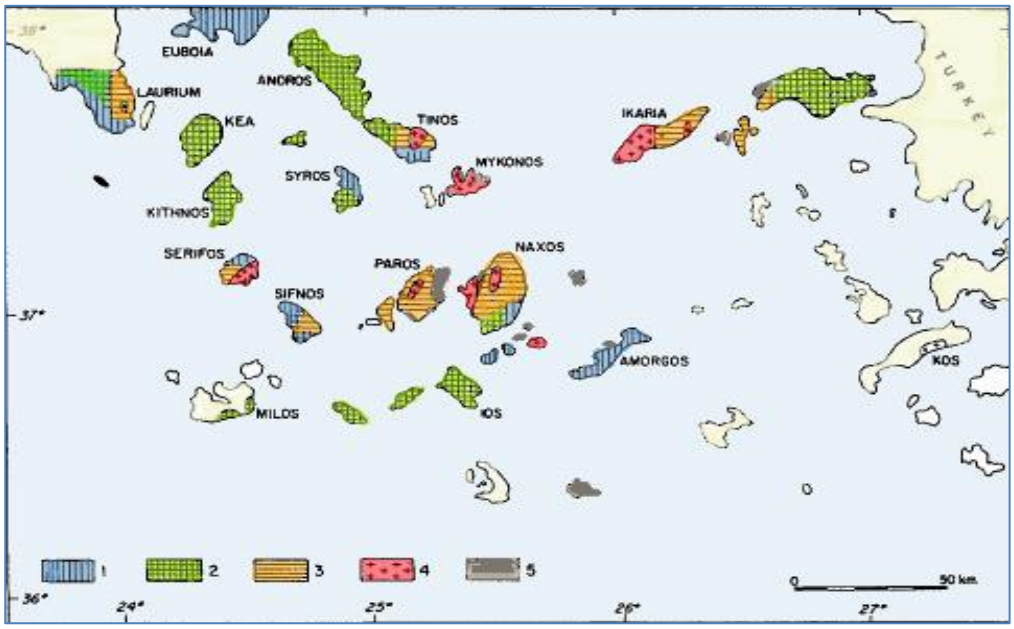

Figure 1.6: Geological map of Cyclades showing the metamorphic domains: 1: High pressure metamorphic rocks. 2: High temperature overprint, 3: High temperature rocks, 4: Miocene granites, 5: non to low metamorphic rocks of the Upper Unit (after Avigad, 1993)

Regional tectonics

The metamorphic formations in the Cyclades show two distinct families of the stretching lineation trends, which are pervasive in the metamorphic rocks of the Cycladic core complexes (Gautier at al., 1993; Walcott and White, 1998); the northwestern part shows NE – SW trending lineations, while in the southeast the lineations trend in a N – S direction (Gautier and Brun 1994; Jolivet et al., 2004) (Fig.1.2). These trends are likely the result of a post-formational vertical axis rotation difference between the northwestern and southeastern Cycladic region. Paleomagnetic data from granites intruded into the Cycladic Blueschist unit revealed that during extensional exhumation in the Miocene the southeastern part of the Cyclades underwent counter-clockwise rotation around 30^{o}, while the northwestern part experienced clockwise rotation of at least 20-30^{o} after the cooling of the granites (Morris and Anderson 1996; Avigad et al., 1998). This fits a regional pattern

of vertical axis rotations in the Aegean-west Anatolian area, whereby the western Aegean region underwent 40-50° clockwise rotations (Kissel and Laj, 1988; van Hinsbergen et al., 2005), and southwestern Anatolia underwent ~20-25° counterclockwise vertical axis rotations (Kissel and Poisson, 1987; Morris et al, 1993; van Hinsbergen et al 2010). The extensional exhumation history of the Aegean region opening metamorphic core complexes including the Cyclades was shown to be consistent with this pattern of vertical axis rotations through a double saloon-door style formation of the Aegean arc (van Hinsbergen and Schmid, 2012).

Geology of Paros

Paros is located in the southern Cyclades and contains Cycladic basement, Cycladic blueschist, and ophiolite (Papanikolaou 1980) (Fig.1.7). The Cycladic basement is locally known as the Marathi Unit and consists of orthogneisses. The Cycladic Blueschist unit retains little of its original HP-LT metamorphism (and its assignment to this unit is hence based on its lithostratigraphic position relative to the Cycladic basement), but is in a dominant HT-LP metamorphic facies (amphibolites, marbles and meta-bauxites) (Bargnesi et al., 2012). The Marathi Unit underlies a low-grade, intensely sheared metamorphic unit (Dryos Unit) characterized by limited and strongly tectonized calc-schist, marbles and metabasites (Papanikolaou 1980). The uppermost tectonostratigraphic, Marmara Unit, is separated by a low – angle detachment fault from the Marathi and Dryos units and comprises a non-metamorphic, heterogeneous unit consisting of ophiolitic formations, limestones (Gautier et al., 1993; Bargnesi et al.,2012) and Miocene supra-detachment basin sediments (Sanchez-Gomez et al., 2002). All the above-mentioned units are overlain by Quaternary deposits including travertine (Evelpidou et al., 2010).

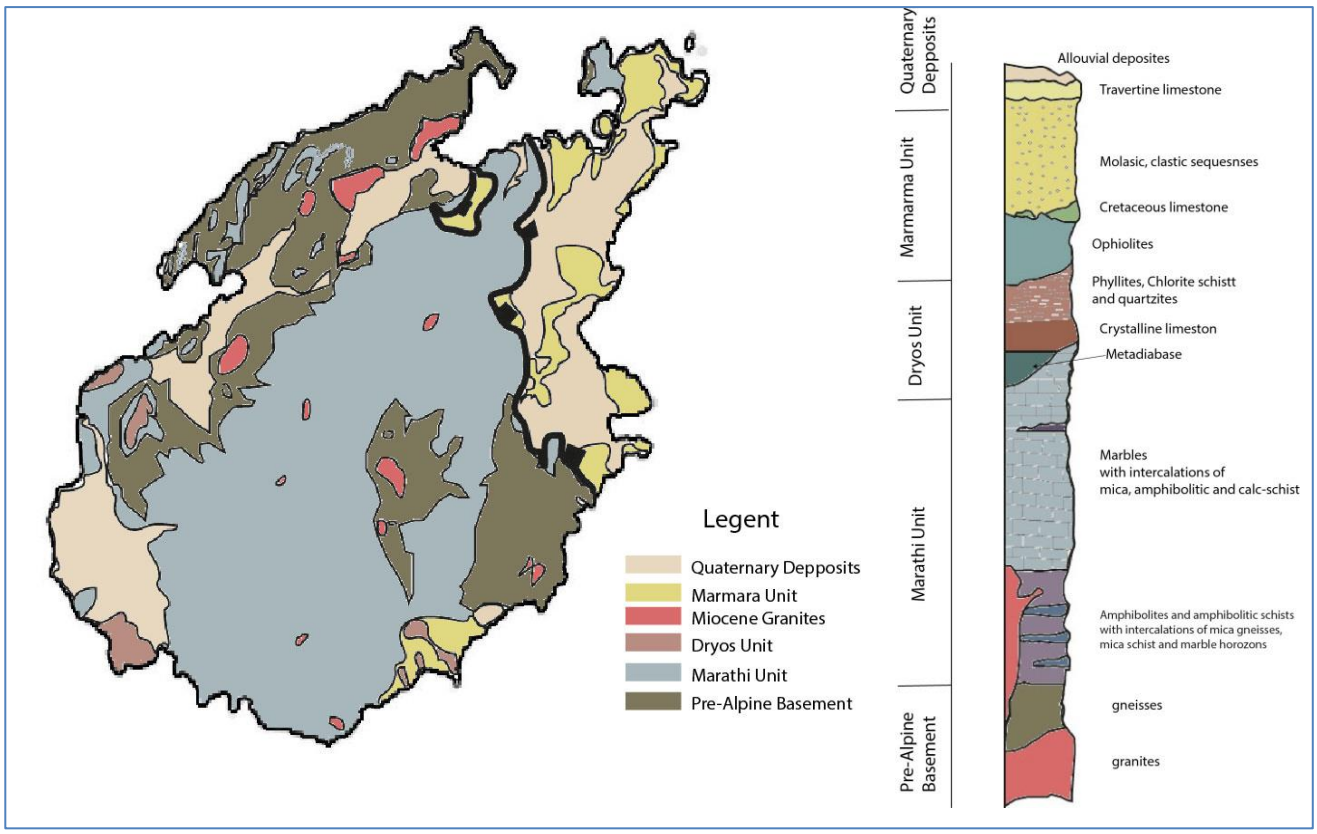

Figure 1.7: Simplified geological map and stratigraphic column of Paros (after Papanikolou 1980).

The observation of the structural characteristics of the rock formations in Paros reveals four deformation events associated with different metamorphic conditions (Gautier et al., 1993). The most striking structural feature on the island is a notable change in the orientation of the stretching lineations. A N-S trending stretching lineation is observed on the central and southeastern part of the island while in the NW part records a NW-SE to E-W trend (Gautier at al., 1993) (Fig. 1.8).

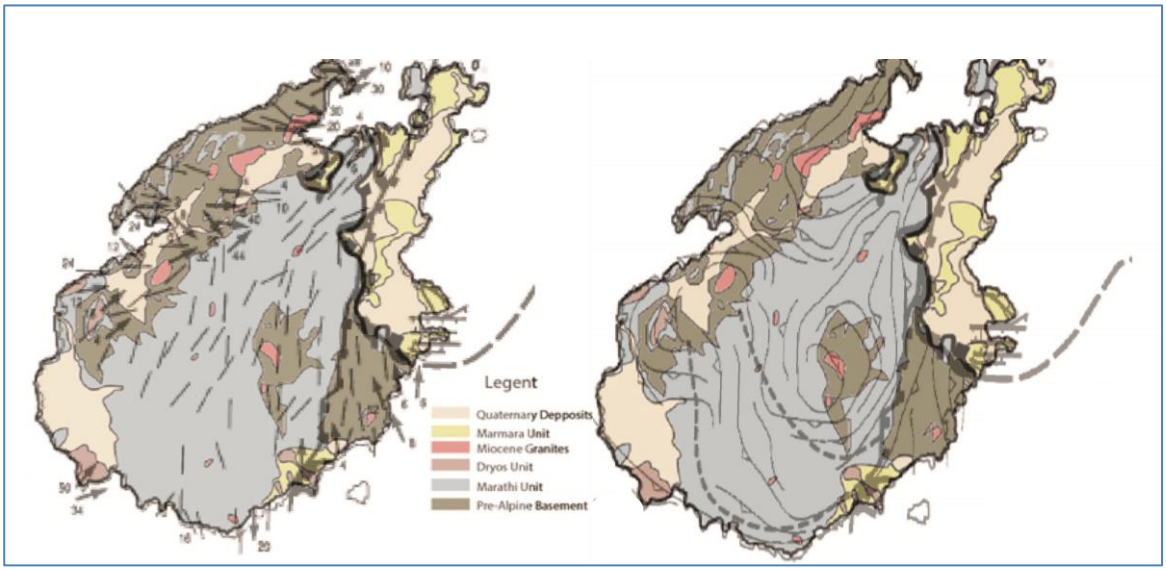

Figure 1.8: structural map of Paros showing the stretching lineation with (arrows) and without (lines) sense of sear (Left) (Gautier et al., 1993).

PART 2: PALEOMAGNETIC STUDY

2 .1 Sampling

The samples for the paleomagnetic study involve 160 core samples which were gathered of sixteen different locations on Paros (Fig.2.1). The samples were drilled using a gasoline powered portable drilling machine. The diameter of the drilled cores was 2.5 cm while the samples were orientated on the field with a magnetic compass determining the dip and the azimuth of the core axis. Additional sample orientation was measured with a sun compass. Samples were marked for their orientation in situ. All core samples were cut to the same size of approximately 2.2 centimeters, according to the laboratory standards, which resulted in multiple specimens per sample.

The samples comprise post tectonic intrusions (granites, aplitic and quartzitic veins and ryolithic dykes). Miocene S-granites (location P1, P2, P3, P4, P6, P9, P10, P11, P14, P15 and P16), intruded to the pre- Aline ortho-gneisses, are slightly deformed displaying a foliation plane with an associate stretching lineation. The main minerals of this rock type are Qz, Pl, Bt, K-Fs and Ms. The emplacement of the aplitic veins (location P5 apart from the samples P48 – P50, P7 and P8) and quartzitic veins (location P12) is related with granitic intrusions and they exhibit foliation and stretching lineation in their surface. The main mineralogy of the aplitic veins is Qz, Fs and Ms and they are dated similar or younger to granites. The rylothithes of Pliocene age (location P13) are composed of a fine grained leucocratic matrix
with phenocrysts of Bt, K-Fs and Pl.

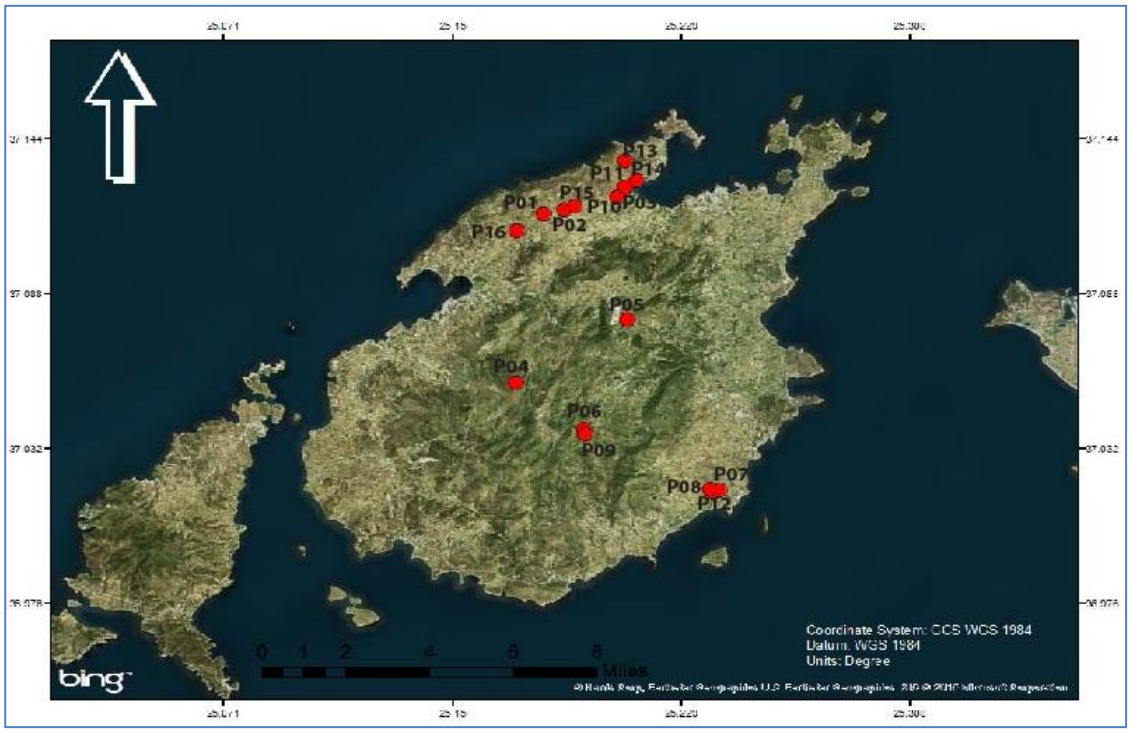

Figure 2.1.: Map showing the location from the drill sites.

2.2 Methods

2.2.1 Thermomagnetic Measurements (Curie Balance)

Curie Balance analyses alongside with the decay of the magnetization during demagnetization experiments were used to gain information about the Curie temperatures of the samples. For this purpose, one sample from each location (16 samples) were crushed to powder and heated up to temperature of 700°C using a horizontal translation Curie balance (Mullender et al., 1993).

2.2.2 Anisotropy of the magnetic susceptibility (AMS)

Petrofabric analysis were performed to define the preferred orientation of the magnetic minerals in the samples. The magnetic fabric was measured using an AGICO MFK1 susceptibily bridge and the AMS was evaluated according to Jelinek statistics (Jelinek, 1977, 1988). The AMS is expressed geometrically with an ellipsoid whose shape is determined by three axis; the maximum (Kmax), the intermediated (Kint) and the minimum (Kmin), where the long axis (Kmax) represent the greatest susceptibility and the short axis (Kmin) the weakest susceptibility. The magnetic lineation (L) of a rock is represented by the orientation of the long axis, while the magnetic foliation (F) (plane perpendicular to the main foliation plane) by the short axis.

2.2.3 Thermal demagnetization

In order to determine the natural remnant magnetization (NRM) of the samples, progressive thermal demagnetization was performed in a 2G Enterprises DC SQUID cryogenic magnetometer (noise level 3 x 10-12 Am2). This method is based on the relationship between the relaxation time and the temperature. When a sample is heated to a temperature T, then all the grains with blocking temperature lower than T, will be reset to zero magnetization. Temperature increments of 30°C were applied from a minimum temperature of 20°C to a maximum temperature of about 690°C (Appendix, table 2). After the samples were successively heated in higher temperatures, they cooled in a null magnetic field environment after each heating and the NMR being measured at each step. For this method one specimen of each core sample was measured.

2.2.4 Alternating Field Demagnetization

In order to confirm the reliability of the information gained by the thermal demagnetization technique the samples were additionally subjected to Alternating Field (AF) demagnetization. This method uses an oscillating field in a magnetic free space. The grains with coercivities below the peak AF follows the alternating field and as the alternating field progressively decreases to zero the coercive force obtains different orientation and the samples are demagnetized along three orthogonal axis. AF demagnetization was performed from 0 to 100 mT in 15 steps of 5 mT in a robotized 2G DC-SQUID cryogenic magnetometer (noise level 12x10-12 Am2) with demagnetization coils attached to the system.

2.3 Results

2.3.1 Curie Balance

The measured magnetization of each sample is plotted as a function of the temperature. The results are described below side by side.

PA1

Various steps in the decay curves of the magnetization reveal multiple fractions characterized by different Curie temperatures. The magnetization is decreasing upon heating up to 350°C, while smaller steps in the demagnetization cuves are observed at 200°C and 240°C. Such steps in the decay curve probably resulted from the breakdown of a high-Ti tinanomagnetite and the presence of iron sulfides such as pyrrhotite. The Curie Balance diagram shows a weak magnetic signal for that site (Fig.2.1)

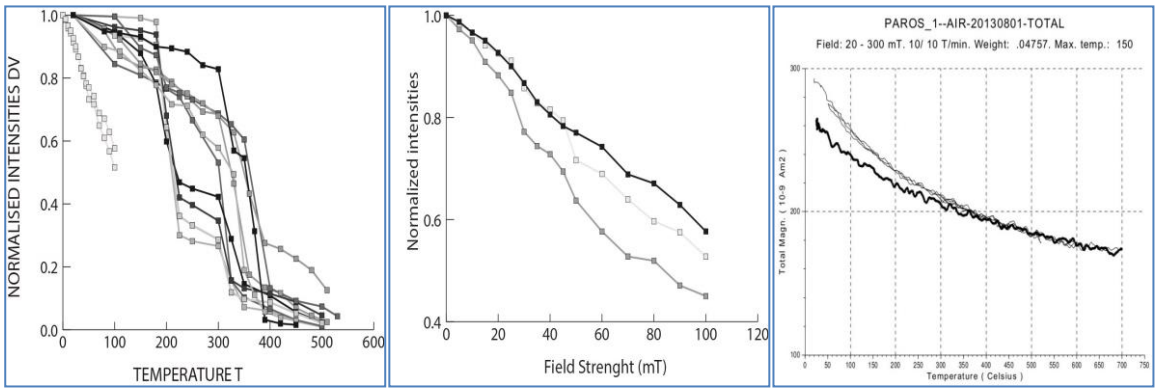

A B C

Figure 2.1: a) decay curves from thermal demagnetization; b) decay curves from Alternating field; c) Curie balance diagram from site PA1.

PA2

From the decay curves it is observed that there is a major decrease from 200°C to 250°C while occasionally in some specimens up to 350°C. Such steps in the decay curves can be interpreted with the presence of high-Ti titanomagnetites (Fig.2.2).

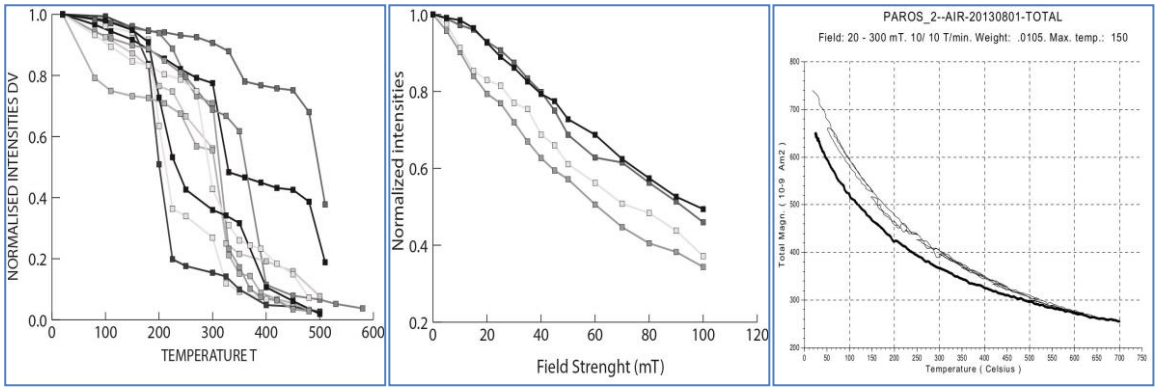

A B C

Figure 2.2: a) decay curves from thermal demagnetization; b) decay curves from Alternating field; c) Curie balance diagram from site PA2.

PA3

Most of the magnetization intensities shows a sudden decrease between 350C° and 440°C, although, some samples reveal smaller steps in their decay curves at 270°C, 300°C and 330°C. Such an observation indicates the presence of low Ti titanomagnetites, while some fractions of iron sulfides are contained as well in that sample (Fig.2.3).

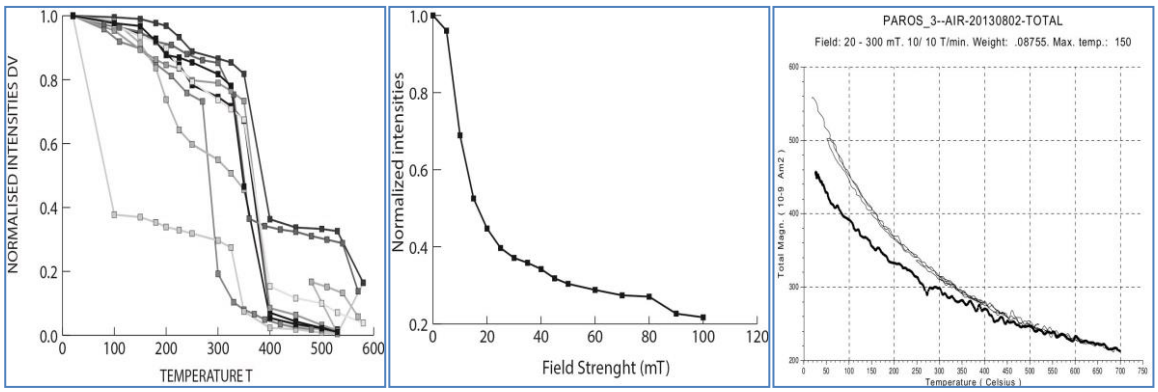

A B C

Figure 2.3: a) decay curves from thermal demagnetization; b) decay curves from Alternating field; c) Curie balance diagram from site PA3.

PA4

The decay curves from that sample, present a notable fall in the magnetization intensities from 300°C to 350°C, indicating the breakdown of low-Ti titanomagnetites (Fig.2.4).

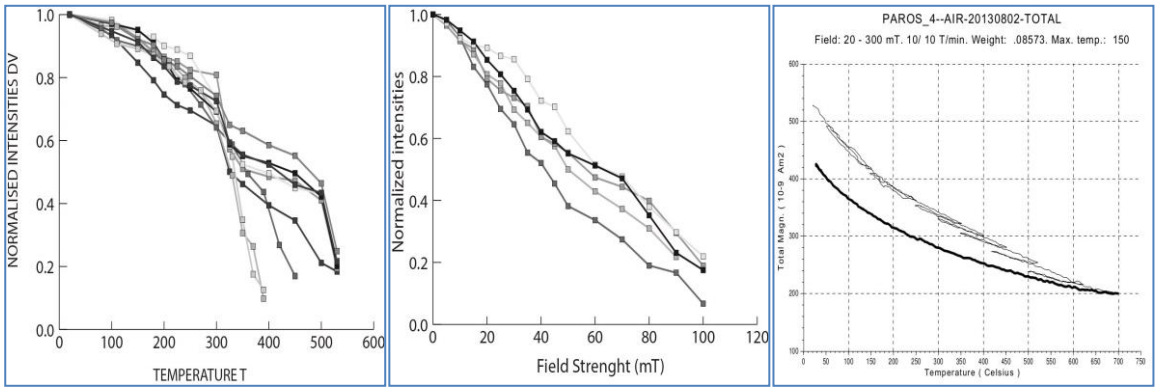

A B C

Figure 2.4: a) decay curves from thermal demagnetization; b) decay curves from Alternating field; c) Curie balance diagram from site PA4.

PA5

The magnetization of that sample is progressively decreased up to 580 °C. At times there is a sudden decay at 240°C and 330°C. The indications from the demagnetization diagrams reveal a low Ti tinanomagnetite component while the Curie temperatures , at around 580°C, suggests the presence of magnetite(Fig.2.5).

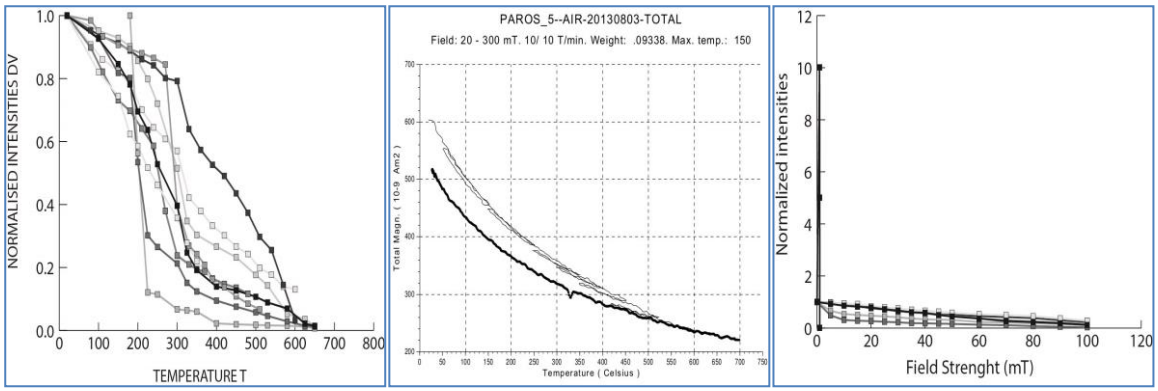

A B C

Figure 2.5: a) decay curves from thermal demagnetization; b) decay curves from Alternating field; c) Curie balance diagram from site PA5.

PA6

From the demagnetization curves it is observed that the magnetization undergoes subsequent increases and decreases up to 500°C, after which it declines up to 530°C. Such a behavior can be explained by the decomposition of the contained iron sulfides, probably pyrite, and the production of a new magnetic phase. The mineral that is formed is broken down again at 530°C, which is the Curie temperature of low-Ti titanomagnetites (Fig.2.6)

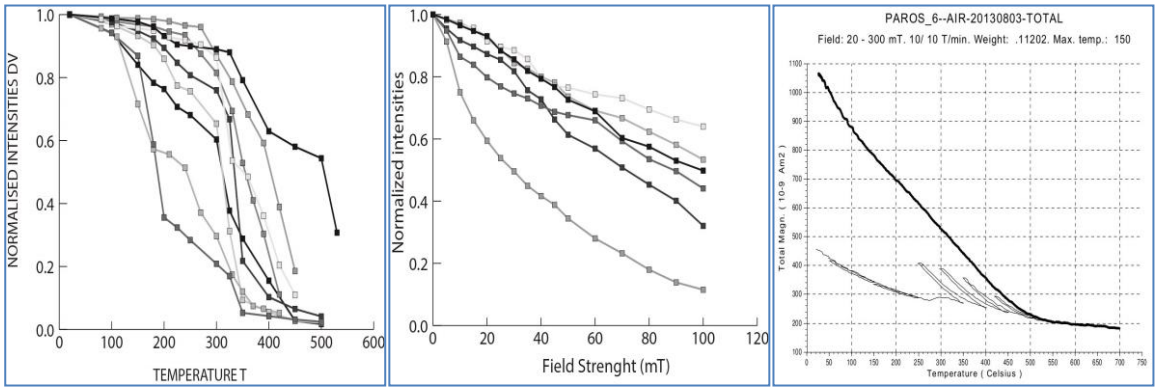

A B C

Figure 2.6: a) decay curves from thermal demagnetization; b) decay curves from Alternating field; c) Curie balance diagram from site PA6.

PA7

The magnetization is decreasing gradually upon heating up to 450°C and occasionally 370°C and reaching the lowest values at 580°C, indicating the transition from the low-Ti titanomagnetite phase to hight-Ti phase (magnetite) (Fig.2.7).

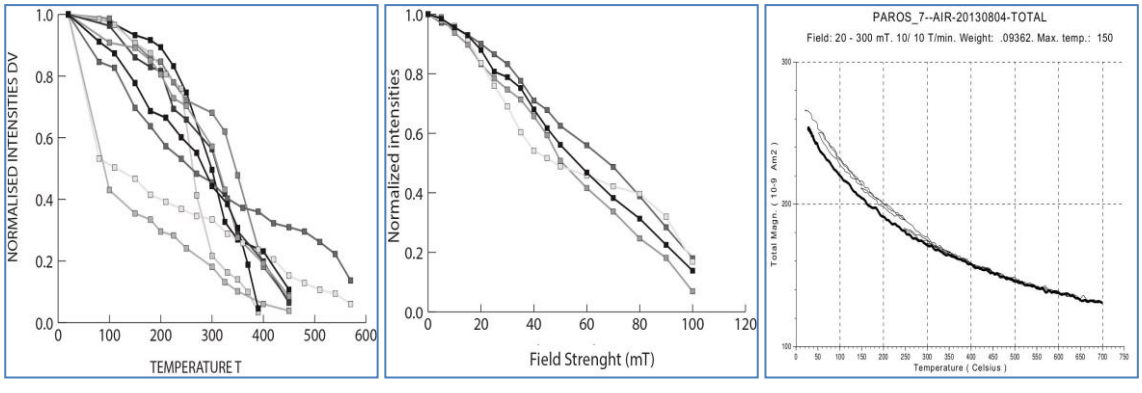

A B C

Figure 2.7: a) decay curves from thermal demagnetization; b) decay curves from Alternating field; c) Curie balance diagram from site PA7.

PA8

The sample is demagnetized gradually with the increase of the temperature, up to 400°C . Although, three samples show a large step in their decay curves from 330°C to 350°C. Such a behavior indicates the decomposition of high-Ti titanomagnetites (Fig.2.8).

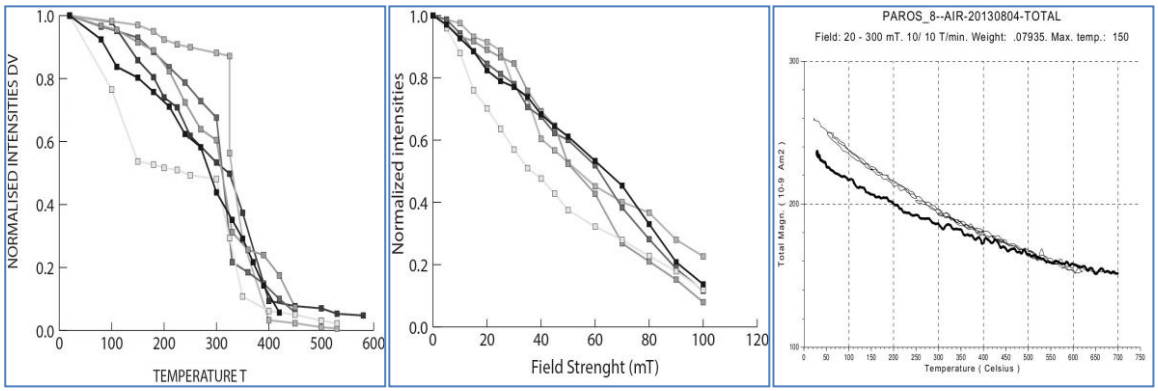

A B C

Figure 2.8: a) decay curves from thermal demagnetization; b) decay curves from Alternating field; c) Curie balance diagram from site PA8.

PA9

The magnetization intensities of that sample show a fall from 250°C to 330°C demonstrating the presence of iron sulfides, as pyrrhotite in the sample, while some fractions of high Ti titanomagnetites can be present as well (Fig.2.8).

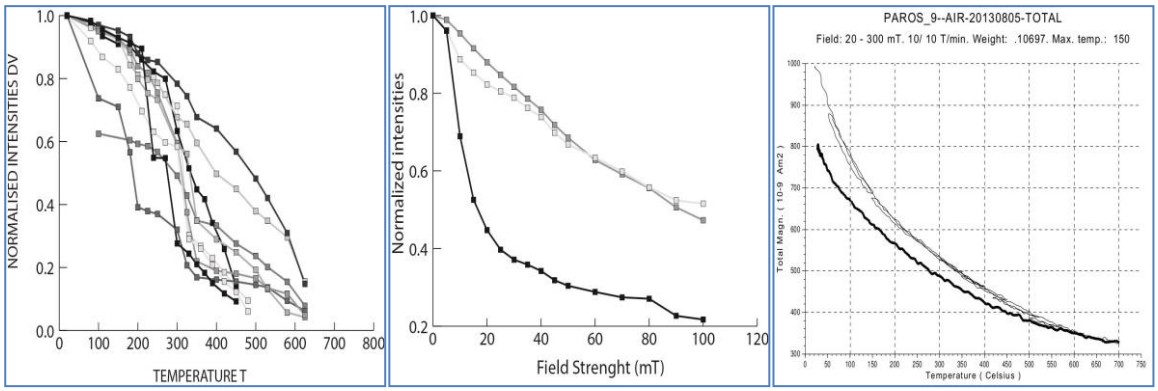

A B C

Figure 2.9: a) decay curves from thermal demagnetization; b) decay curves from Alternating field; c) Curie balance diagram from site PA9.

PA10

The decay curves present a remarkable fall from 300°C to 330°C and occasionally there is a drop from 370°C to 400°C revealing as magnetic components iron sulfides and low-Ti titanomagnetires respectively (Fig.2.10).

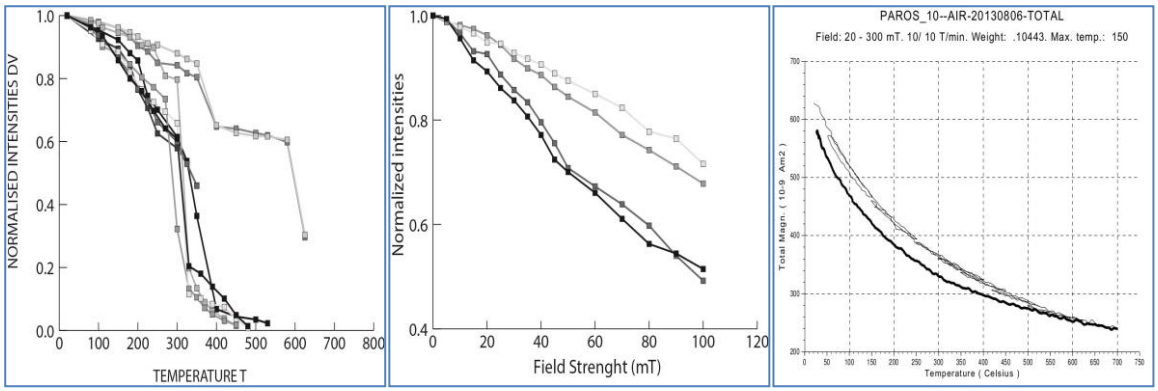

A B C

Figure 2.10: a) decay curves from thermal demagnetization; b) decay curves from Alternating field; c) Curie balance diagram from site PA10.

PA11

According to the decay curves a noticeable decline occurs from 270°C to 330 °C implying the presence of low-Ti titanomognetites in the composition of the samples(Fig. 2.11).

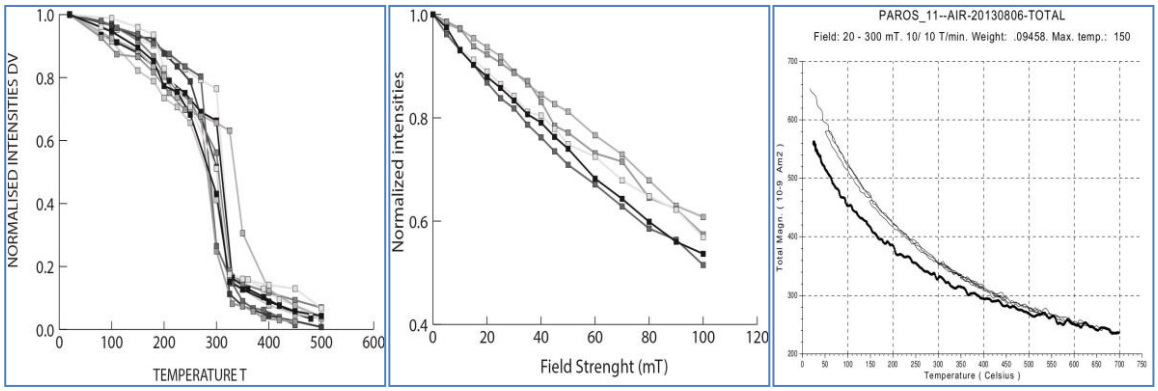

A B C

Figure 2.11: a) decay curves from thermal demagnetization; b) decay curves from Alternating field; c) Curie balance diagram from site PA11.

PA12

The magnetization of that site decays constantly with the rise of the temperature up to 690°C, which corresponds to the Curie point of hematite Although the existence of pyrrhotite can be concluded as well from the sudden fall of the magnetization intensities from 300°C to 330°C in two specimens(Fig. 2.12).

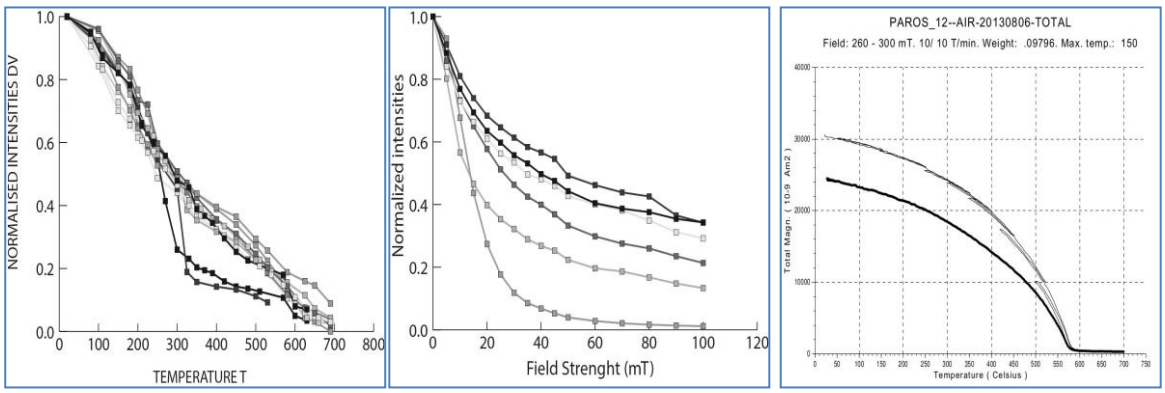

A B C

Figure 2.12: a) decay curves from thermal demagnetization; b) decay curves from Alternating field; c) Curie balance diagram from site PA12.

PA13

The decay curves follow a discontinuous path until reaching the temperature of 680°C where acquires zero values, which corresponds to the Curie temperature of hematite (Fig. 2.13).

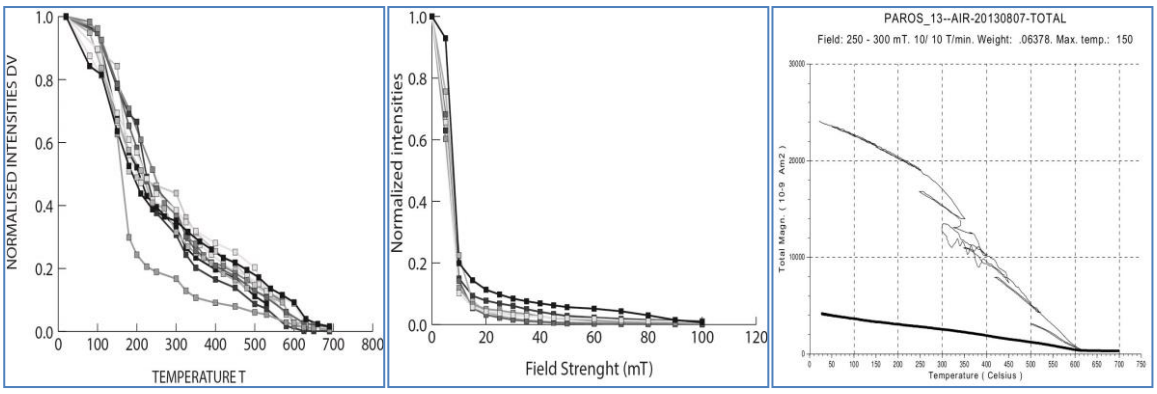

A B C

Figure 13: a) decay curves from thermal demagnetization; b) decay curves from Alternating field; c) Curie balance diagram from site PA13.

PA14

The discrete shape of the decay curves presents a notable drop from 300°C to 330°C, while smaller steps in the demagnetization curves are observed at 225°C and 100°C. This behavior can be explained with the presence of high Ti titanomagnetites, while some fraction of iron sulfides can be present as well (Fig. 2.14).

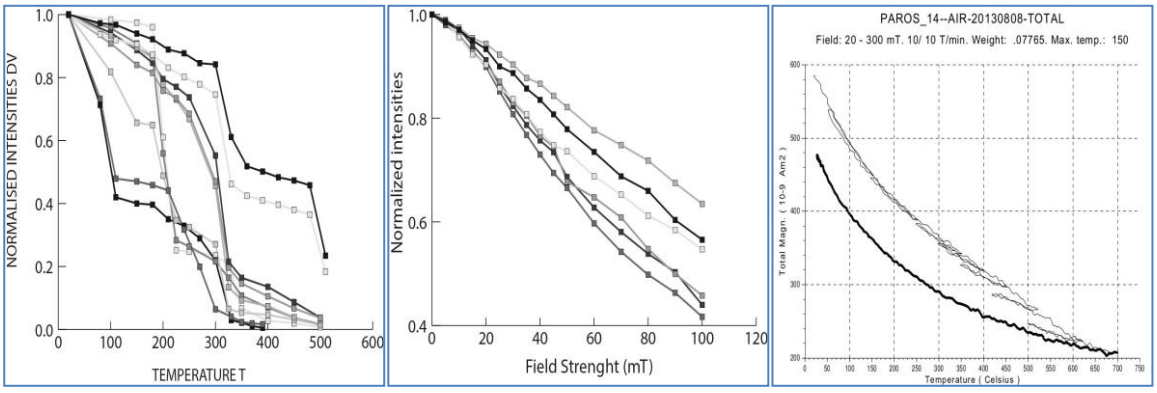

A B C

Figure 2.14: a) decay curves from thermal demagnetization; b) decay curves from Alternating field; c) Curie balance diagram from site PA14.

PA15

The thermal behavior of that site shows a decay on the magnetization intensities from 300°C to around 500°C concluding the presence of low-Ti titanomagnetites, while the occurance of iron sulfides is possible as well (Fig. 2.15).

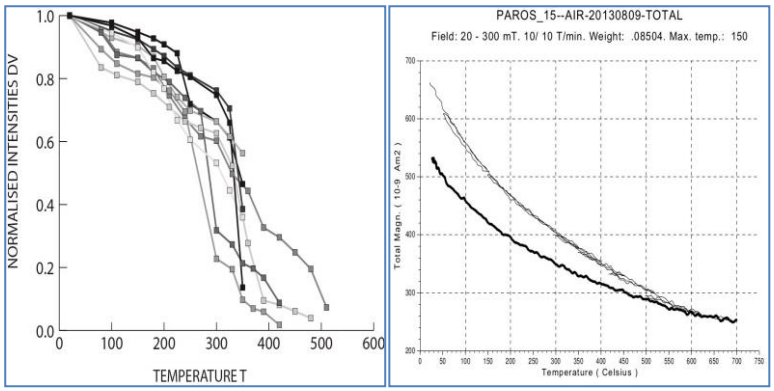

A B

Figure 2.15: a) decay curves from thermal demagnetization; b) Curie balance diagram from site PA15.

PA16

This site indicates mainly a steady demagnetization behavior up to 500°C and at times large decay steps from 370°C to 400°C which conforms to the decomposition temperatures of iron sulfides. A decay is marked at 180°C as well, which is linked with a rich Ti phase of titanomagnetite component (Fig. 2.15).

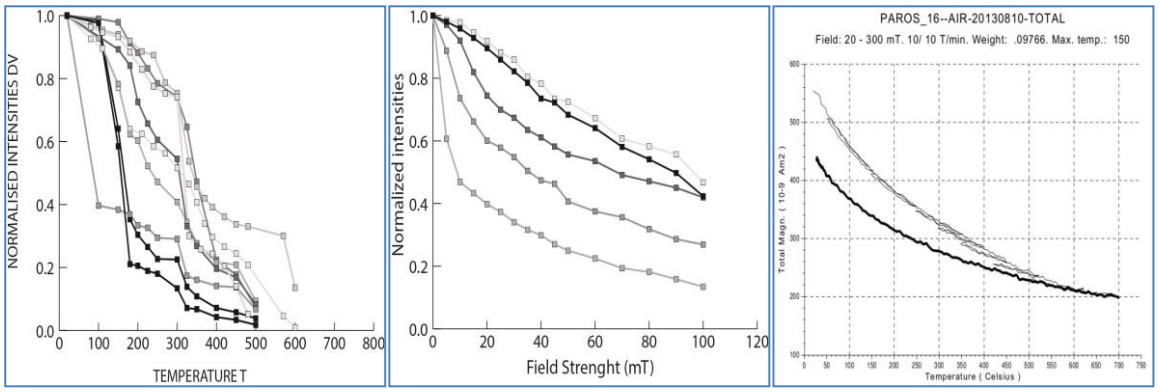

A B C

Figure 2.16: a) decay curves from thermal demagnetization; b) decay curves from Alternating field; c) Curie balance diagram from site PA16.

2.3.2 AMS

A) Magnetic Lineation (L)

The measured results from the anisotropy of the magnetic susceptibility (AMS) are plotted in an equal area projection illustrating the directions of the Kmax axis (magnetic lineation) (Fig 2.17) and magnetic foliation (Fig.2.18) (table1). The potted magnetic lineations for sites PA2, PA4, PA5, PA6, PA13, PA14, PA15 and PA16 are highly distributed and therefore no preferred orientation for the Kmax axis can be concluded from that sites. Although, the Kmax axis from sites PA7 and PA12 are clearly aligned N-S. Additionally, the orientations of the magnetic lineation from sites PA1 and PA11 are highly clustered at NNW-SSE direction. Finally site PA3 indicates an E-W orientation of the Kmax axis. The determined acceptable directions of the magnetic lineation are plotted in the geological map of Paros **(Fig.3.1).**

B) Magnetic foliation (F)

The plotted magnetic foliations represented by the Kmin axis are presented in figure 2. From the following diagrams it can be observed that the majority of the sites show a well-developed foliation plane and only sites PA5, PA8, and PA6 exhibit a scattered orientation for the Kmin axis. Besides the obtained T values (table 1) reveal an oblate fabric for sites PA1, PA2, PA3, PA10, PA10, PA11, PA14 and PA15, while sites PA 4 and PA7 display triaxial fabric. Finally prolate fabric is determined for sites PA6 and PA12 according to the T values

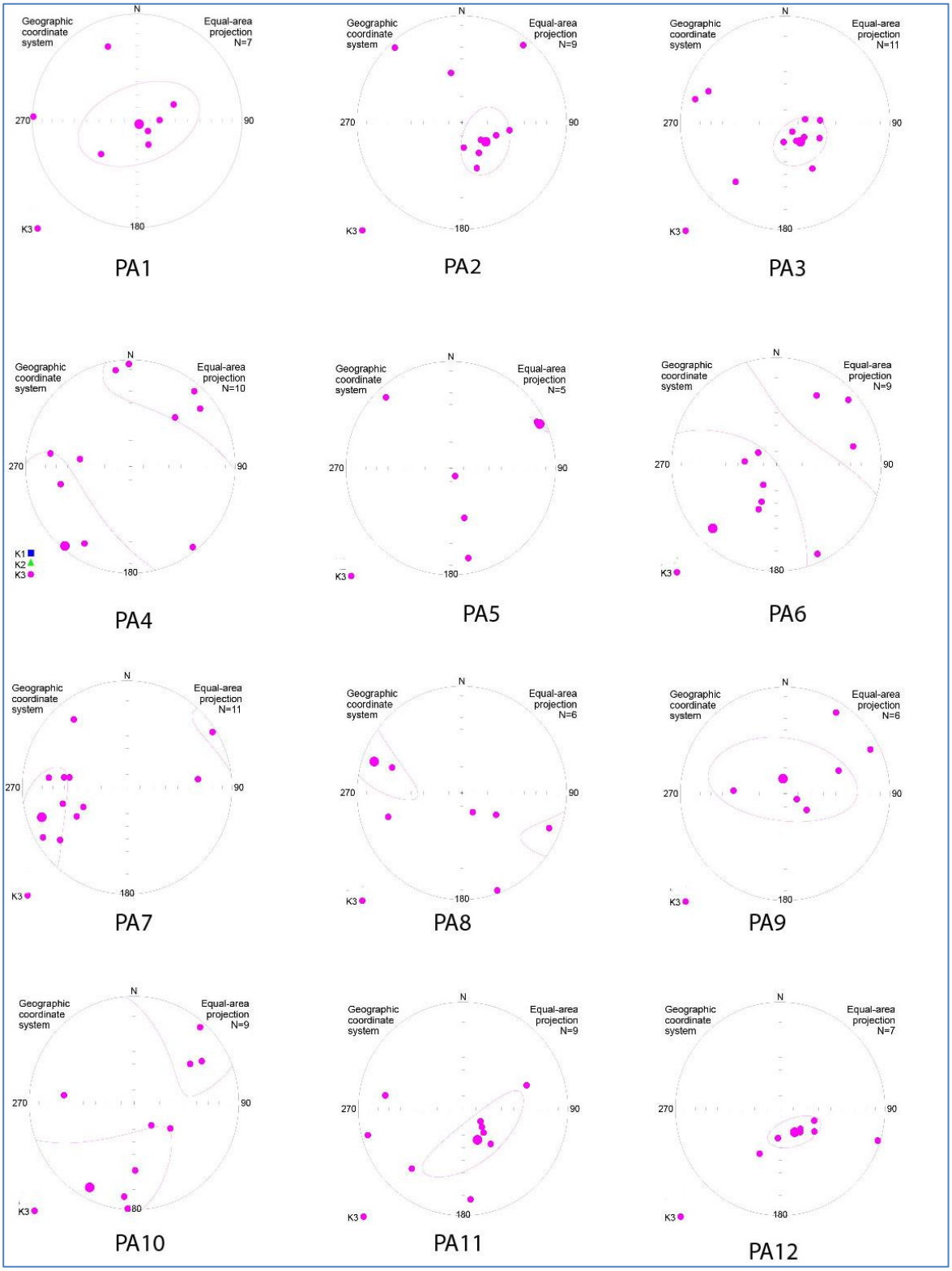

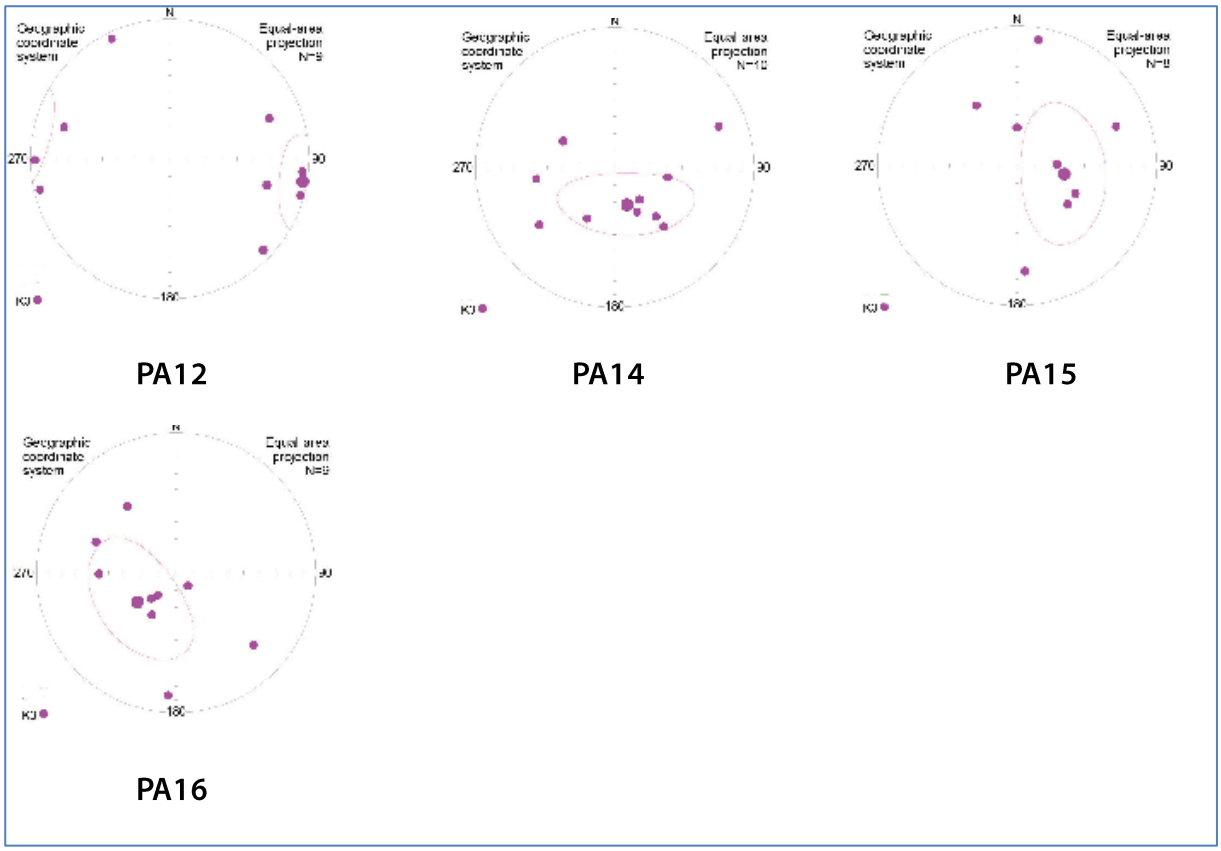

Figure 2.17: plotted magnetic lineation (L) in an equal area projection.

. site	Magnetic Lineation (L)	Magnetic foliation(F)	P	T
PA1	1.023	1.027	1.050	0.0079
PA2	1.008	1.069	1.077	0.798
PA3	1.015	1.069	1.086	0.624
PA4	1.008	1.011	1.019	0.180
PA5	1.626	1.917	3.115	0.145
PA6	1.005	1.006	1.001	0.117
PA7	1.036	1.021	1.058	-0.261
PA8	1.045	1.031	1.077	-0.175
PA9	1.022	1.015	1.038	-0.184
PA10	1.029	1.011	1.041	-0.431
PA11	1.030	1.034	1.056	0.059
PA12	1.096	1.067	1.170	-0.172
PA13	1.007	1.024	1.031	0.537
PA14	1.022	1.051	1.074	0.358
PA15	1.030	1.045	1.007	0.195
PA16	1.032	1.043	1.076	0.146

Table 1: measure values for AMS

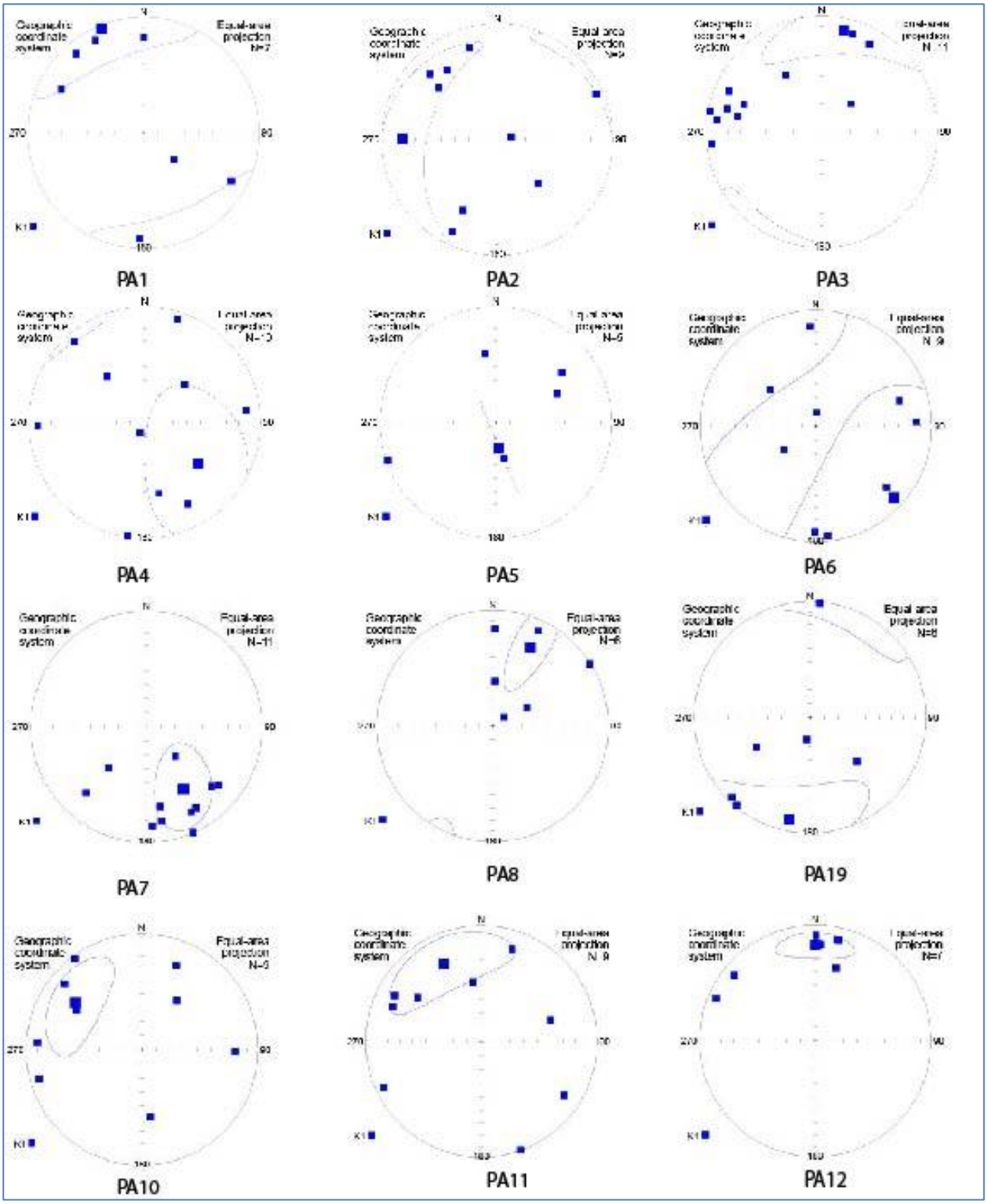
PA1
PA2
PA3
PA4
PA5
PA6
PA7
PA8
PA19
PA10
PA11
PA12

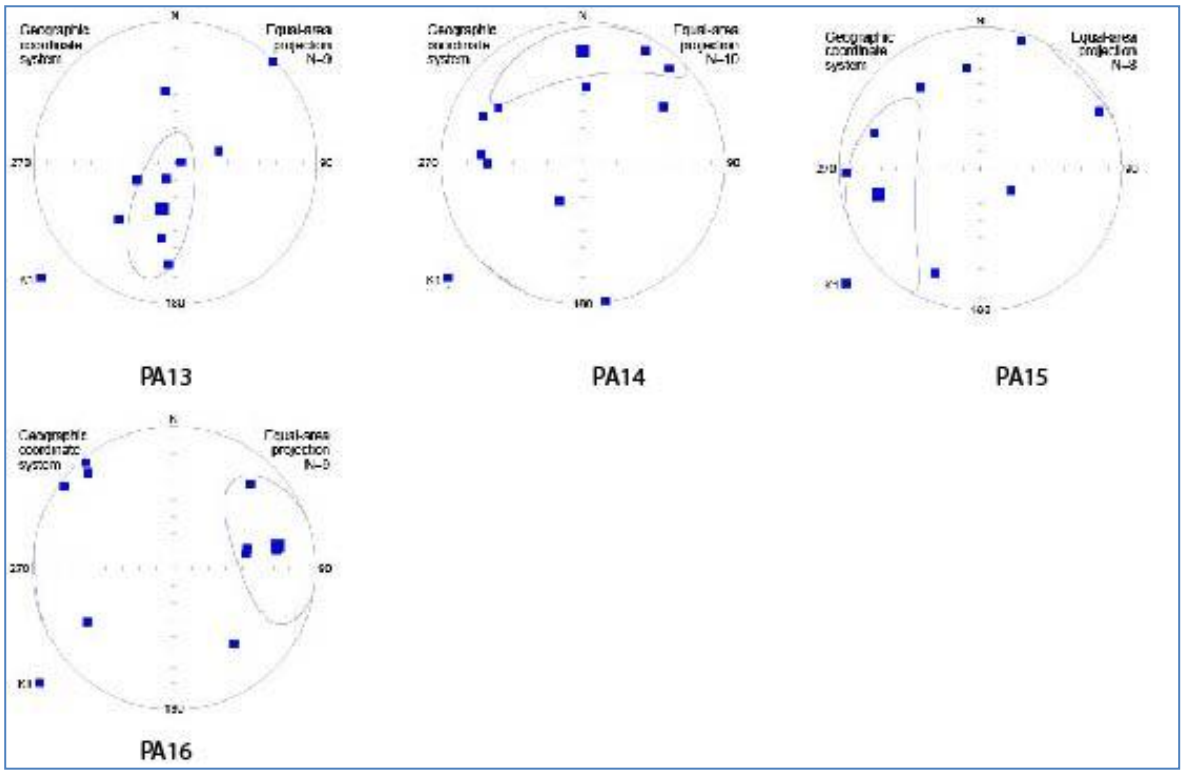

Figure 2.18: plotted magnetic foliation (F) in an equal area projection.

2.3.3 ChRM Analyses

The results from the AF demagnetization all together with the results from the thermal demagnetization of the NRM are projected in orthogonal vector demagnetization diagrams according to Zijderveld, 1967. The characteristic remanent magnetization (ChRM) directions were calculated by using principal component analysis (Kirschvink, 1980). Further information is obtained by applying great circle analyses, where the ChRM directions were not possible to be gained directly from the Zijderveld diagrams. Moreover, statistical analyses applied on the output data, based on the calculation of the virtual paleomagnetic pole. The confidence circle values A_{95} are used here as a criterion for the reliability of the paleomagnetic data according to Deenen et al., 2011. In the specific study case a value of A_{95min} of 4° and A_{95max} of 15° is used for N from 8 to 17 . Specimens from all core samples were used for this method. The measured results are described below for each site. The orientation of the declination values are plotted together with the stretching lineations in the geological map of Paros (Fig.3.1)

PA 1

Samples from site PA1 show a distinct difference between the low (LT) and high (HT) temperature components (Fig.20a). The HT components are defined mainly at temperature up to 325°C – 350°C while the LT components are clustered at temperatures up to 300°C and occasionally up to 350°C (sample PA008). The samples display a major clockwise direction of rotation with declination values of 114° and inclination 52.3°. The 45° cut-off analyses show well clustered ChRM directions in the same orientation (Fig.2.20b).

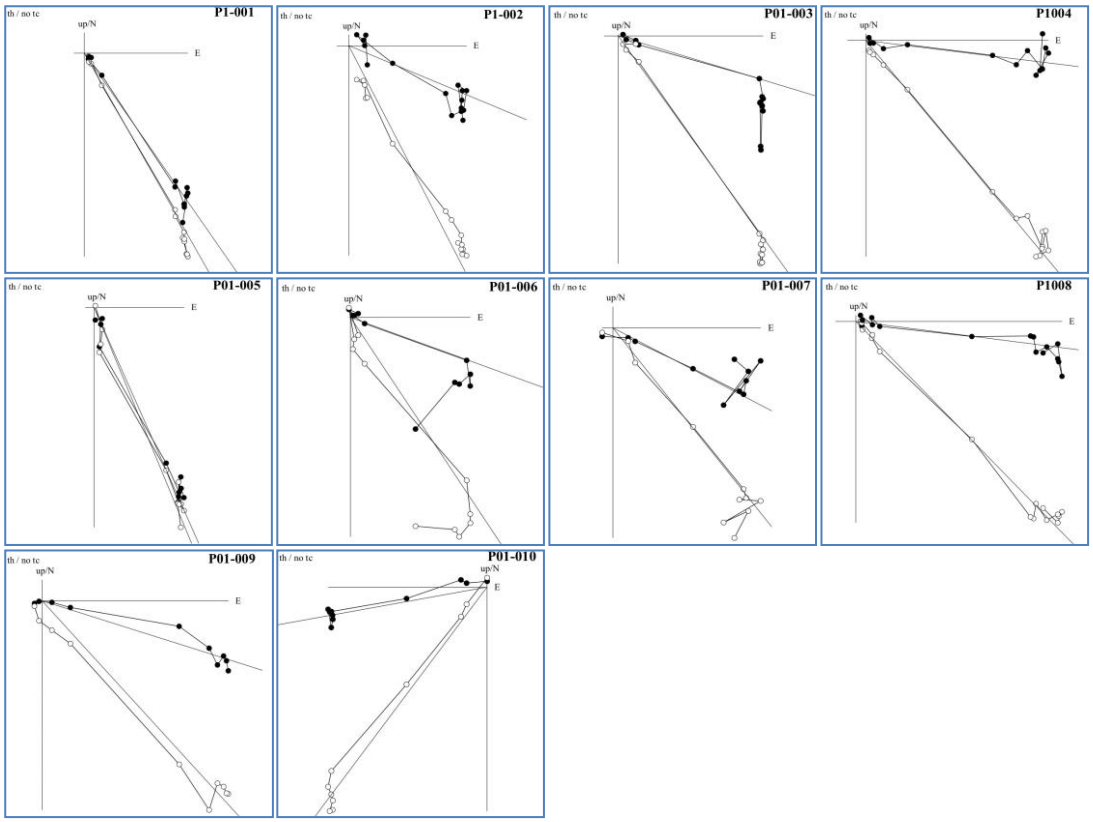

Fig 2.20a: Zijderveld diagram from site PA1.

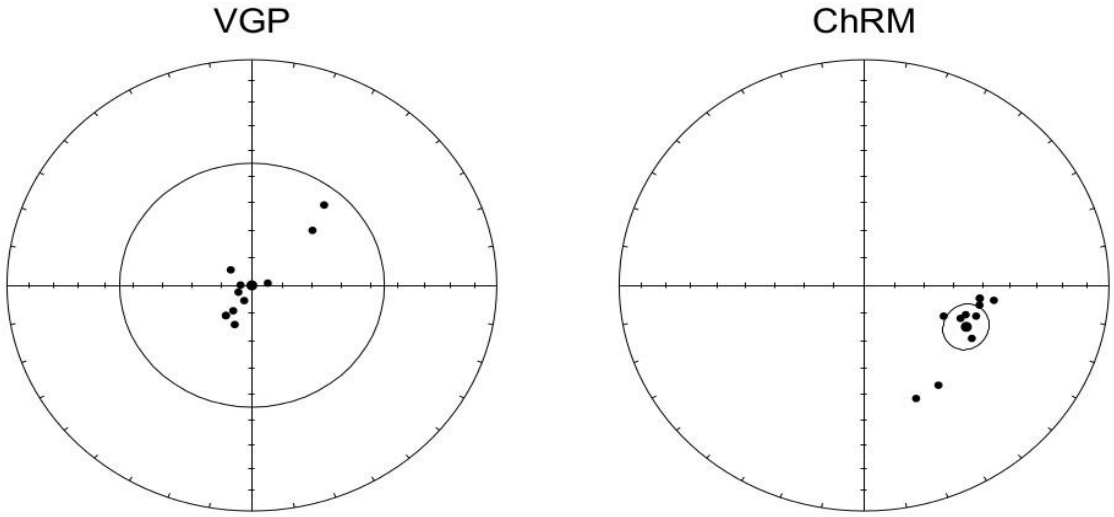

Figure 2.20b: plotted VGP and ChRM directions for site PA1

PA 2

The component analyses from site PA2 indicates that they are divided in two groups. The HT components are demagnetized, not always toward to the origin (P011, PA012, PA013, PA015, PA016), at temperatures of 330°C to 400°C. The LT component is defined at temperatures from 200°C to 300°C (Fig.2.21a). The declination values for this site are 97° and the inclination is 60°. All the samples are plotted within the circle of confidence (Fig.2.21b).

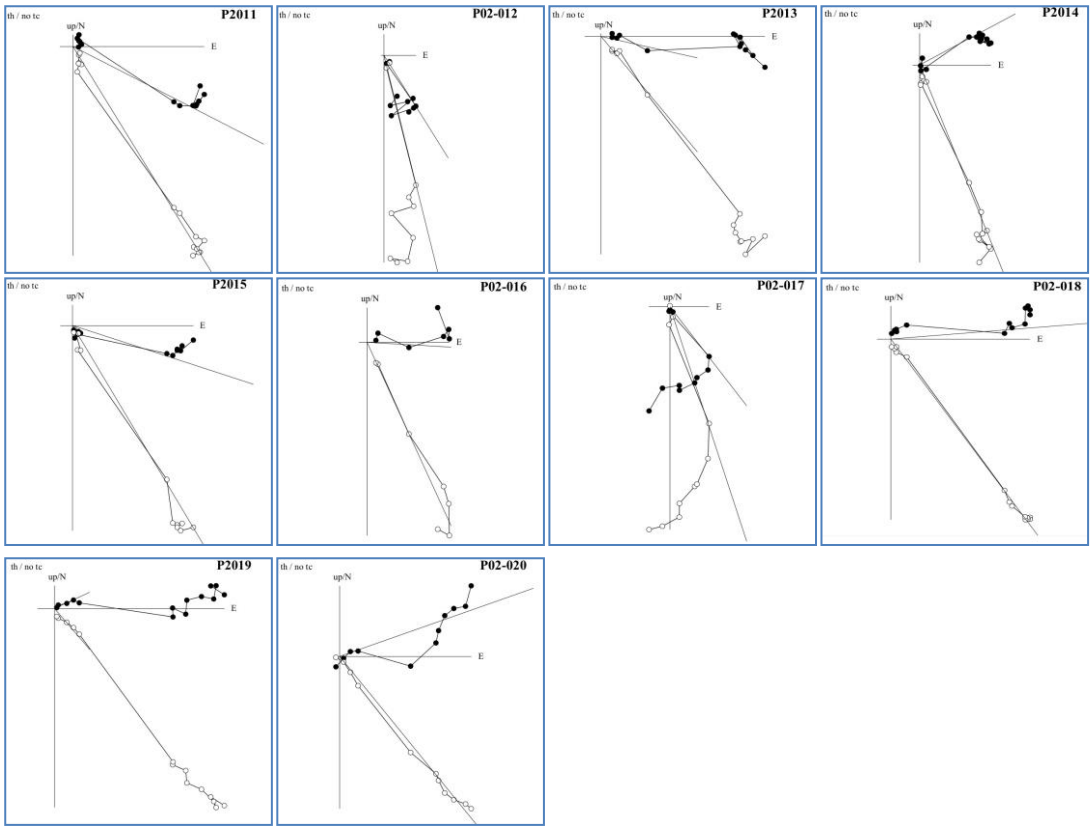

Fig 2.21a: Zijderveld diagram from site PA2.

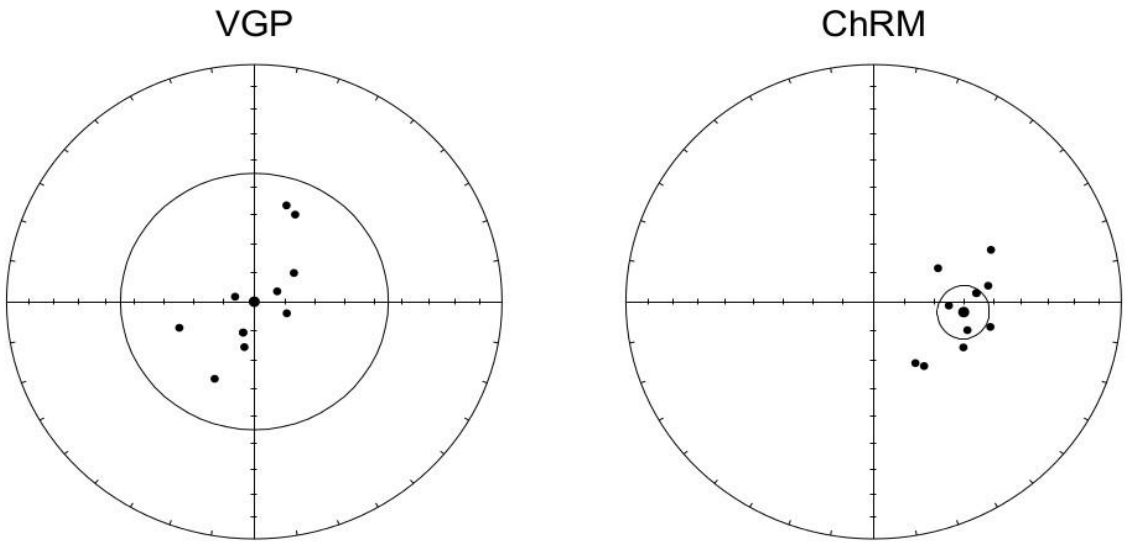

Figure 2.21b: plotted VGP and ChRM directions for site PA1

PA 3

From the Zijderveld diagrams two different components are well observed. The HT component is demagnetized through the origin at temperatures of 360°C to 400°C. On the other hand, the secondary magnetization is defined at 350°C. All samples show a consistent clockwise direction at 64.3° with inclination values at 51.9° (Fig.2.22a). The fixed 45° cut-off analysis shows well concentrated directions of the ChRM (Fig.2.22b).

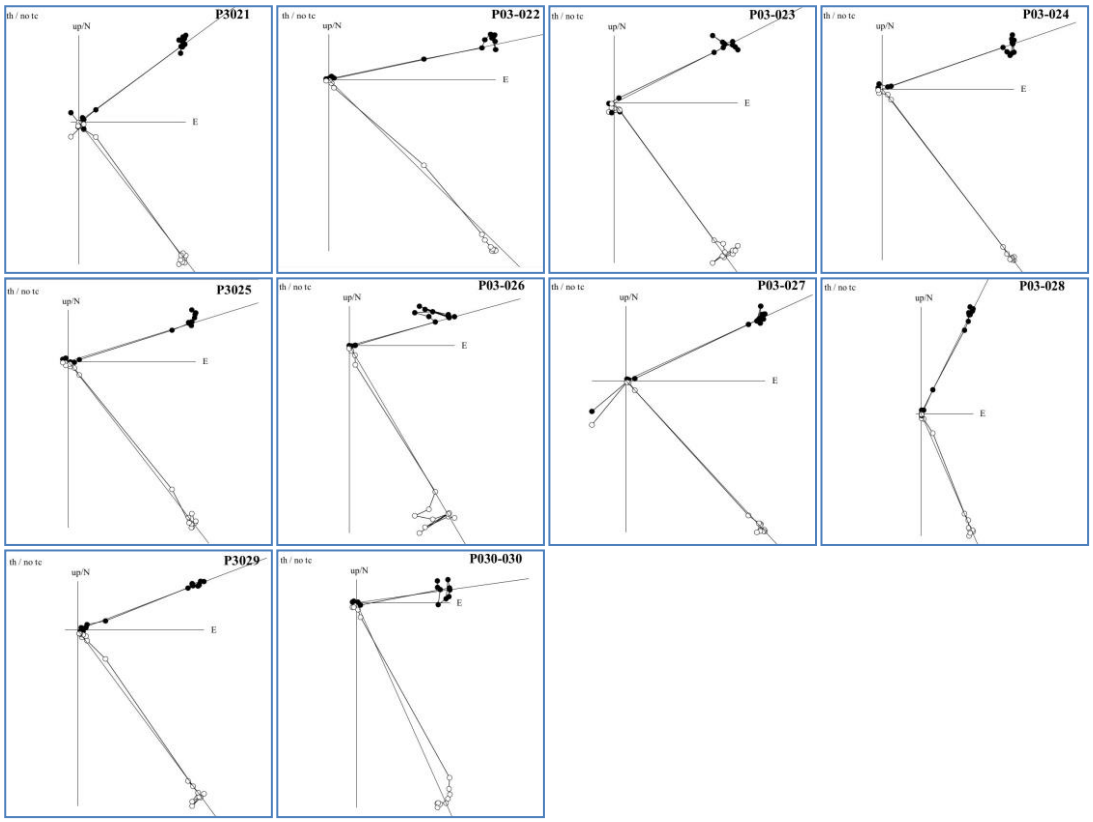

Fig 2.22a: Zijderveld diagram from site PA3.

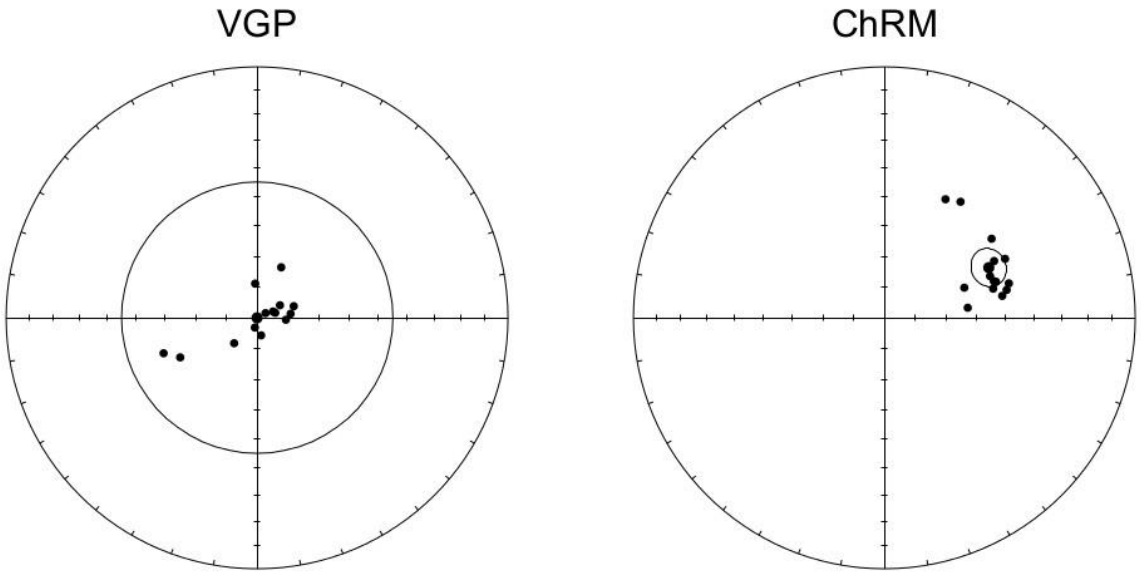

Figure2.23b: plotted VGP and ChRM directions for site PA3.

PA 4

The results from the analysis from site PA4 displays a distributed demagnetization curve from the components up to temperatures of 450°C indicating a less stable component. The rotation is determined at 317° clockwise (or 43° anticlockwise direction) (Fig.2.23a). The calculated mean poles, however they are poorly scattered, they are plotted within the error confidence circle(Fig. 2.23b).

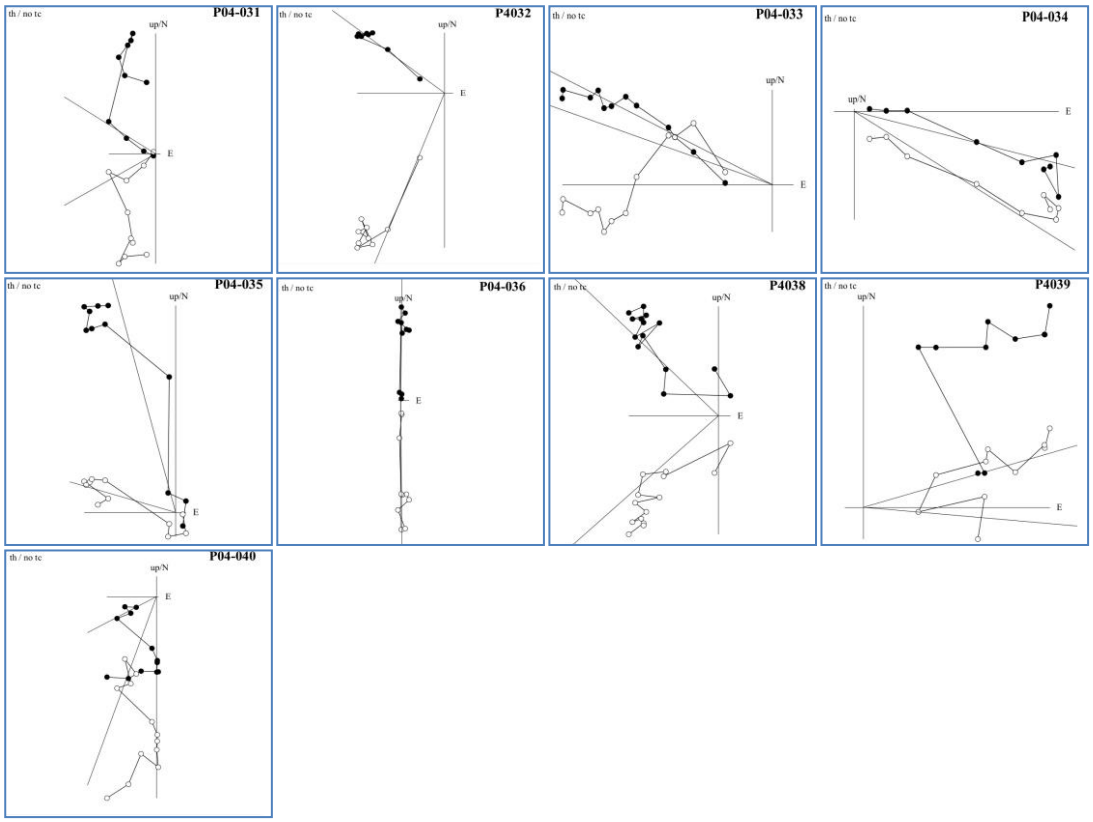

2.23a: Zijderveld diagram from site PA4.

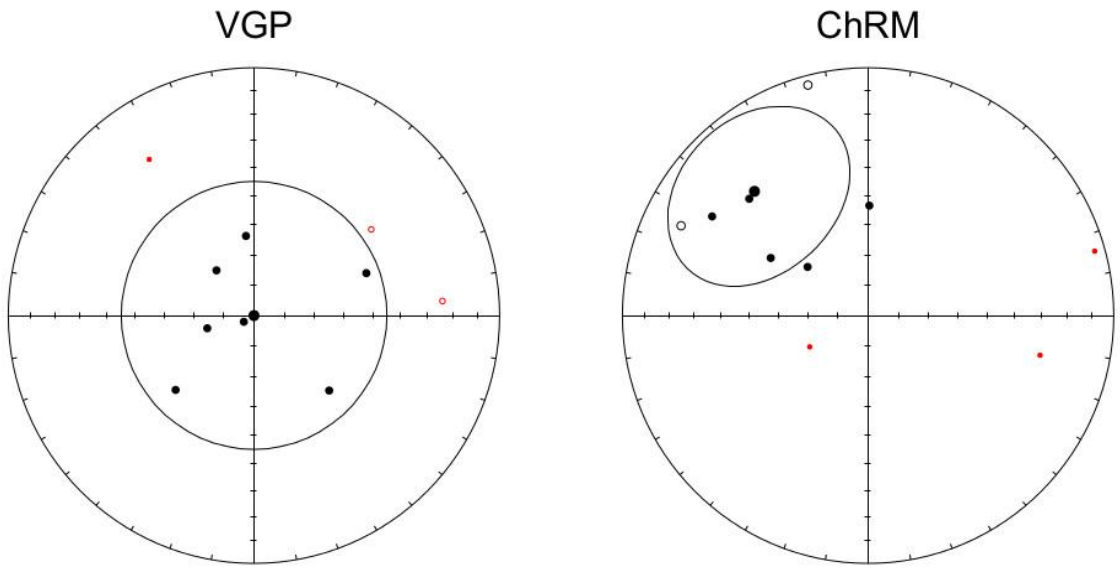

Figure

Figure 2.23b: plotted VGP and ChRM directions for site PA4.

PA 5

These samples exhibit both thermally discrete and distributed components (PA5043, PA047, PA5048, PAP049). The secondary magnetization, where displayed, is projected at 300°C, while the samples reached the Curie temperatures of 350°C – 500°C and occasionally at 600°C (PA048, PA49) (Fig.2.24a). The declination values for this site is 14° and the inclination 35,9°. The 45° cut off analyses show that the ChRM directions are well clustered (Fig.2.24b).

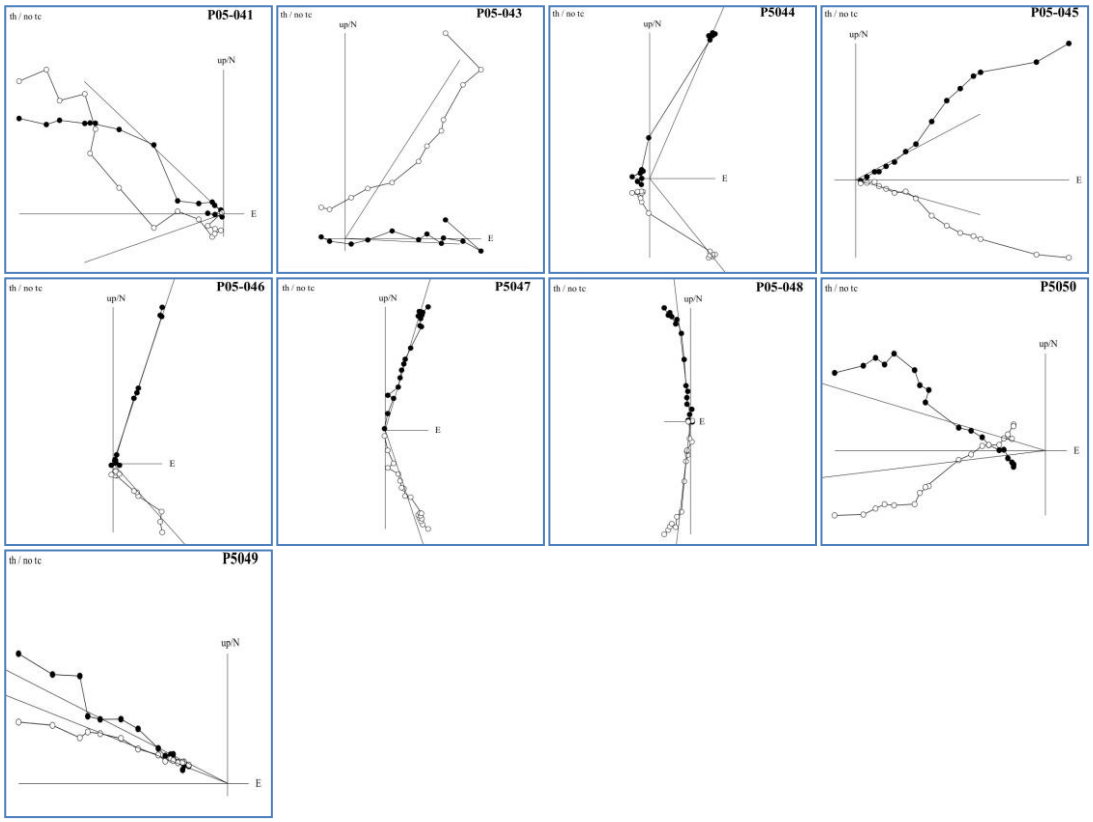

Fig 2.24a: Zijderveld diagram from site PA5.

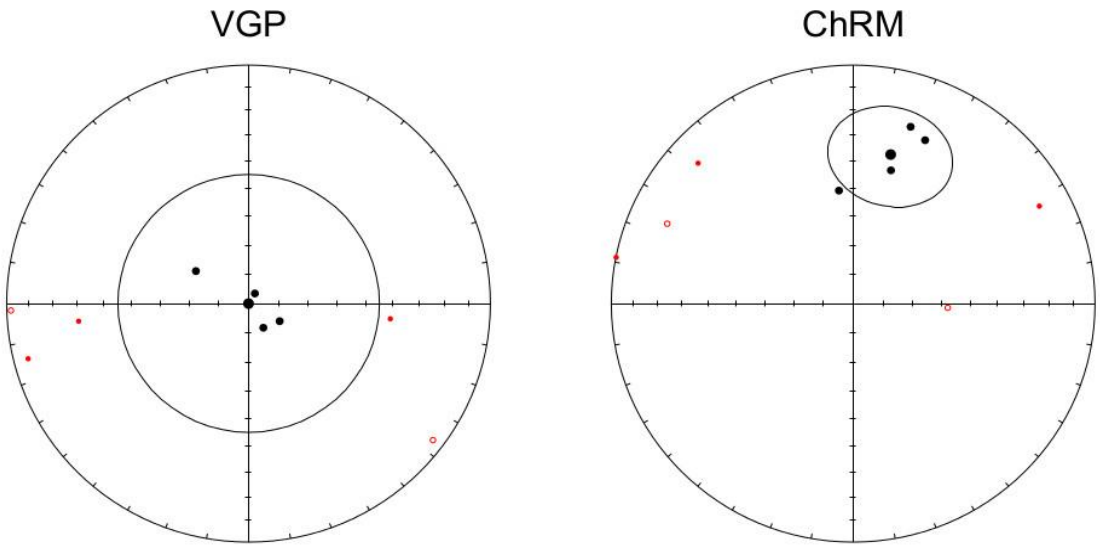

Figure 2.24b: plotted VGP and ChRM directions for site PA5.

PA 6

The plotted results for site PA 6 illustrate a HT component at temperatures of 325°C – 350°C and only PA6059 reaches at 450° and a LT component which derives from lower temperatures up to 300°C. Not all the demagnetization curves go to the origin (PA651, PA6052, PA6053). From the thermal analyses the obtained declination and inclination values are 353,2° and 22,2° respectively (Fig.2.25a). The ChRM directions are oriented at the same direction with acceptable cut-off values. (Fig. 2.25b).

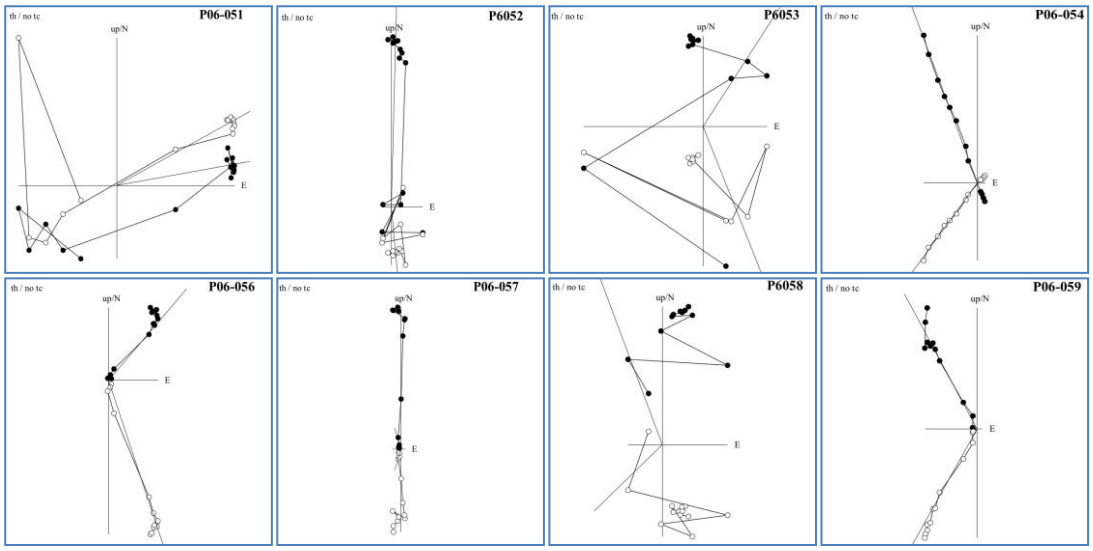

Fig 2.25a: Zijderveld diagram from site PA6.

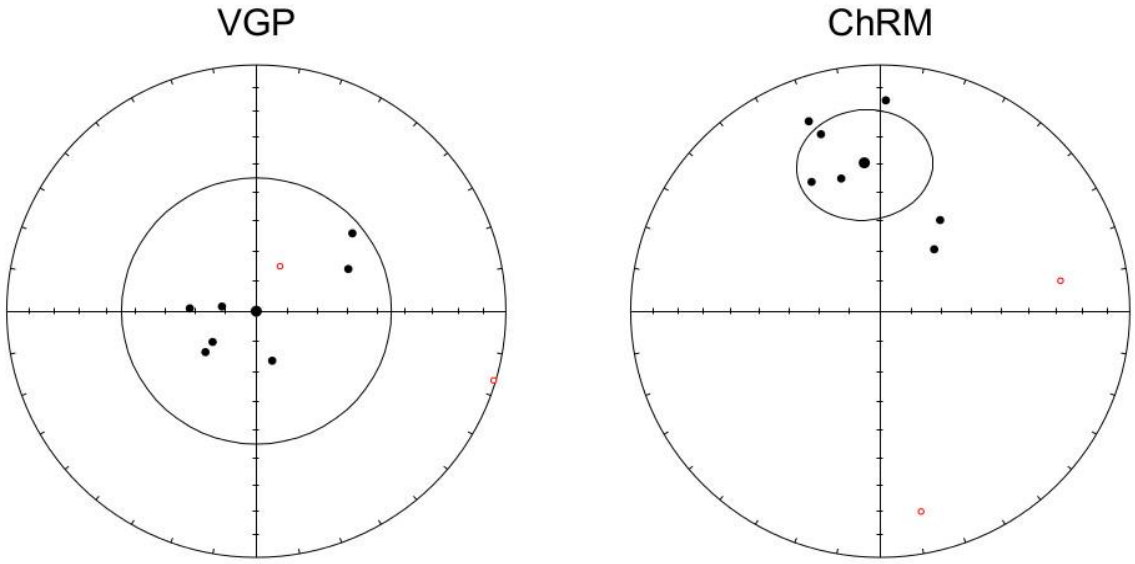

2.25b: plotted VGP and ChRM directions for site PA6.

PA 7

The plotted results for site PA7 shows different direction for each specimen. PA063 and PA069 are demagnetised gradually, not reaching the origin, while PA068 presents two distinct components. The majority of the demagnatization curves depict declination values of 334,8° and inclination of 22,2°(Fig.2.26a). The statistical quantifies for that sample meet the requirements for further interpretation (Fig.2.26b).

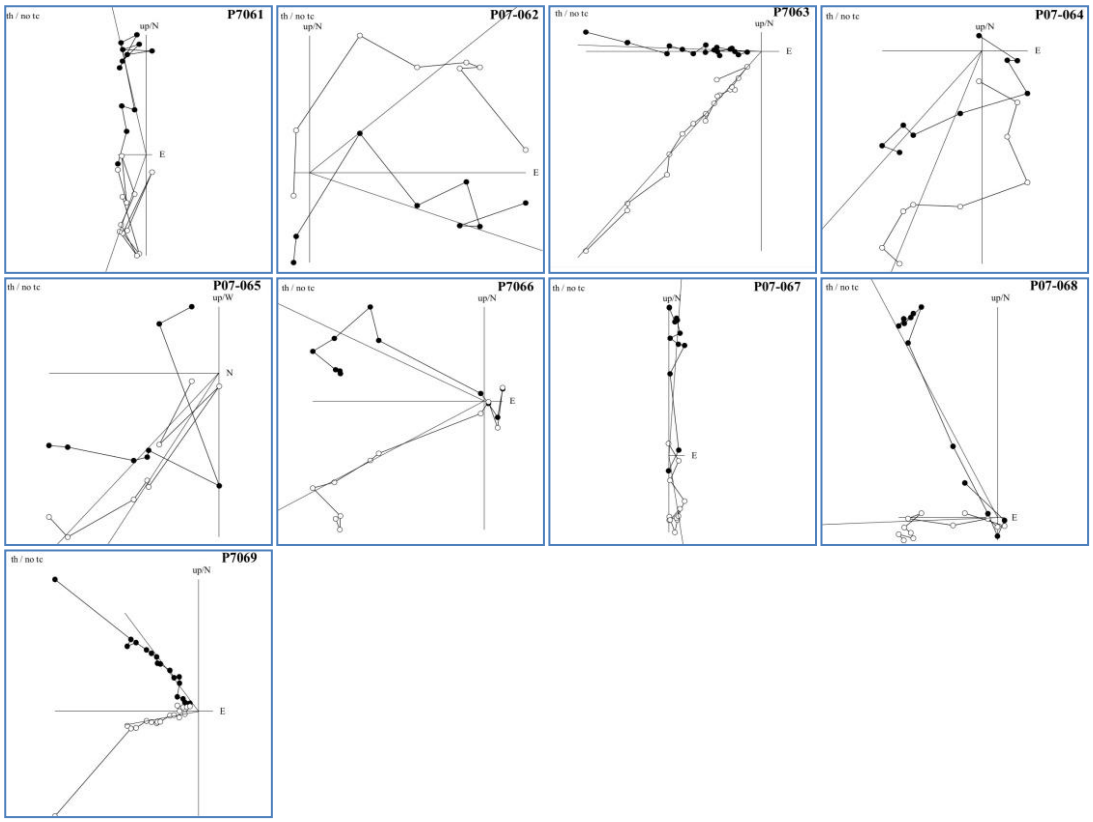

Fig 2.26a: Zijderveld diagram from site PA7

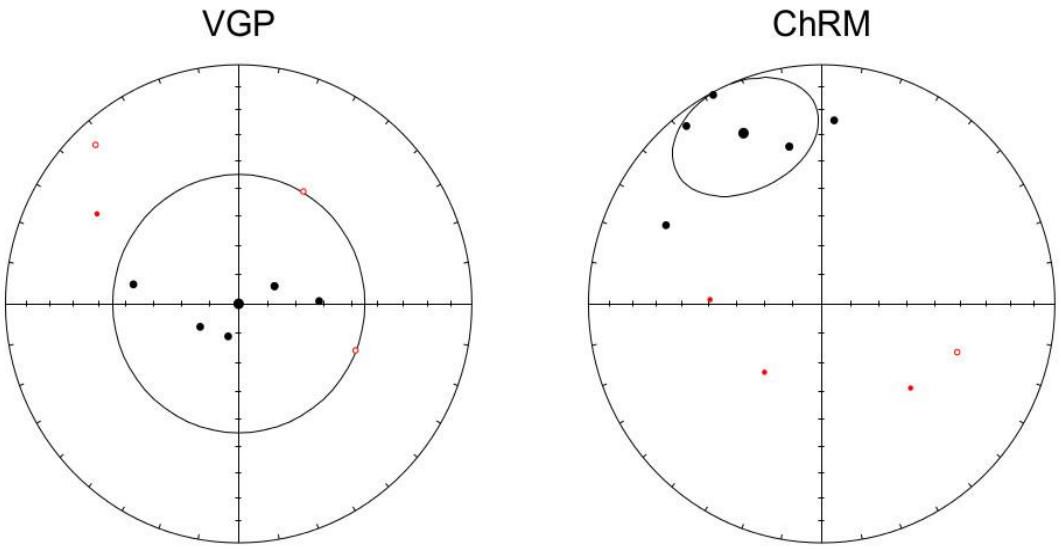

Figure 2.26b: plotted VGP and ChRM directions for site PA7.

PA 8

However, the diagrams from that site do not show any regularity according to the shape of the demagnetazation curves, they point at 352° rotation from the north point with inclination values t 19,2° (Fig.2.27a). Additionally, the plotted directions of the ChRM are well concentrated (Fig. 2.27b).

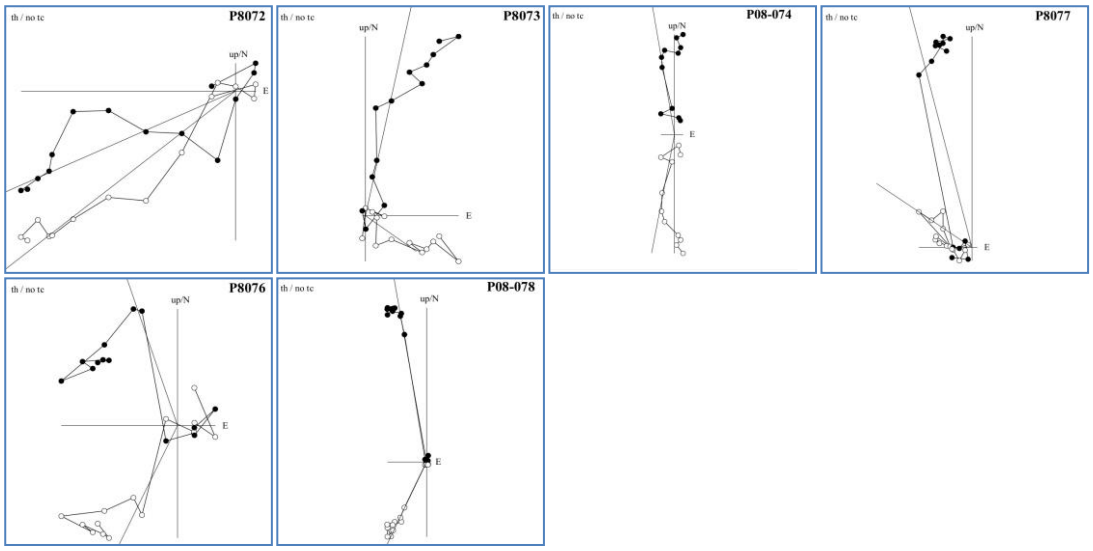

Fig 2.27a: Zijderveld diagram from site PA8.

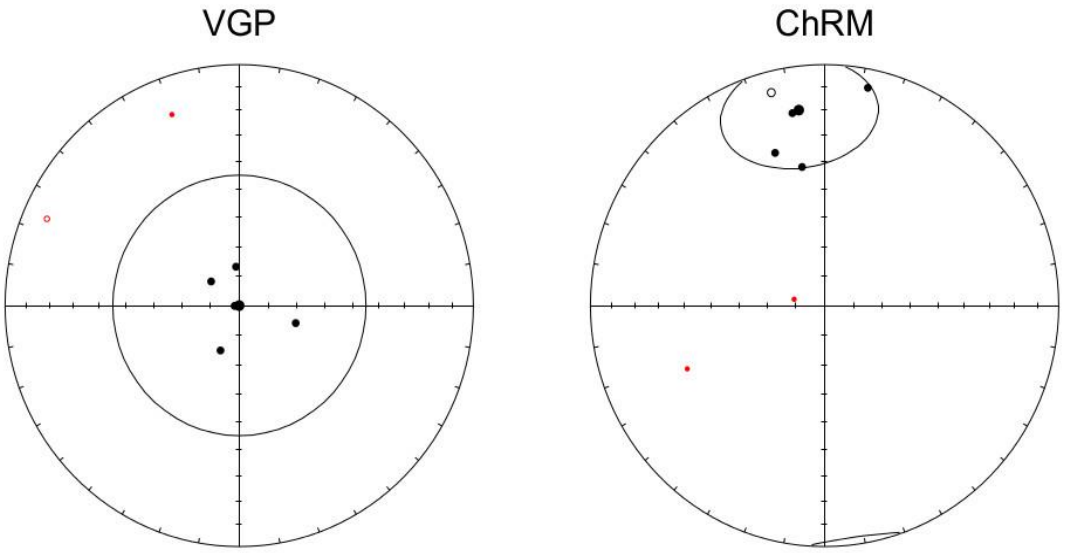

Figure 2.27b: plotted VGP and ChRM directions for site PA8.

PA 9

The plotted results from that site illustrate both discrete and distributed thermal curves (Fig. 2.28a). The measured declinations point at 331,8° and the inclination at 30,5°. However the ChRM directions are poorly clustered, they are plotted within the acceptable confidence circle (Fig. 2.28b).

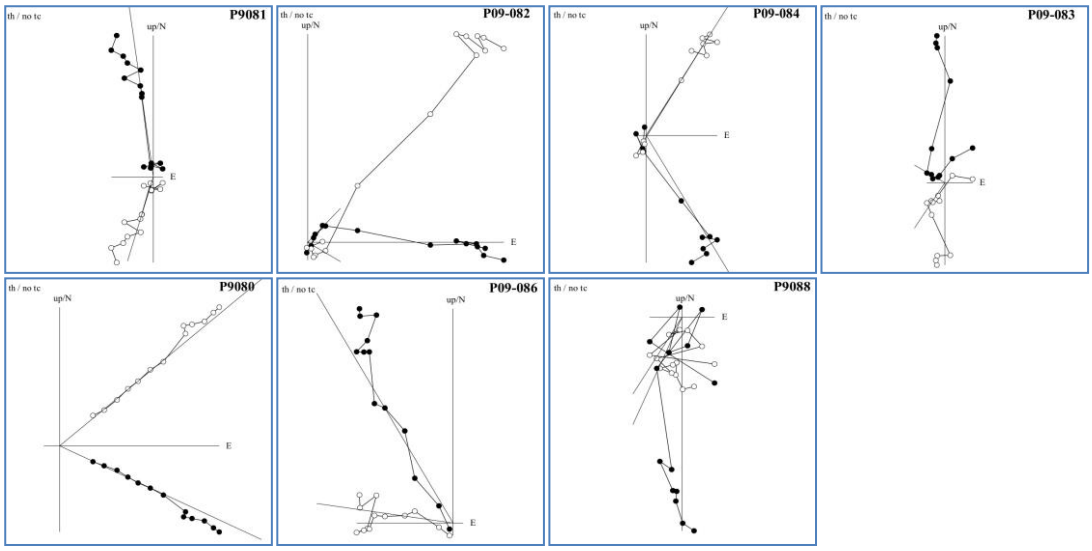

Fig 28a: Zijderveld diagram from site PA9.

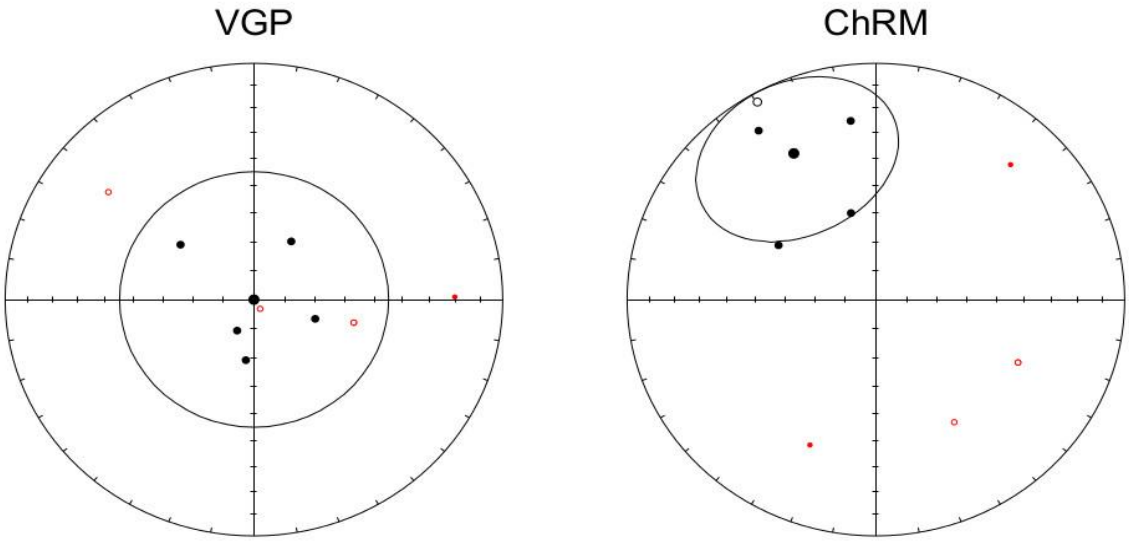

Figure 2.28b: plotted VGP and ChRM directions for site PA9.

PA 10

The demagnetization curves from this sample analyses are dived in two parts; a HT component, derives from temperature of 400° to 480° and occasionally up to 580° (PA094) reaching the origin. An overlap is determined at temperatures of 325° to 350°. Samples PA085 and PA089 were not demagnetized completely. The measured declination is 87.5° and the measured inclination is 47.3° (Fig.2.29a). According to the statistical plots the ChRm orientations are well clustered (Fig. 2.29b).

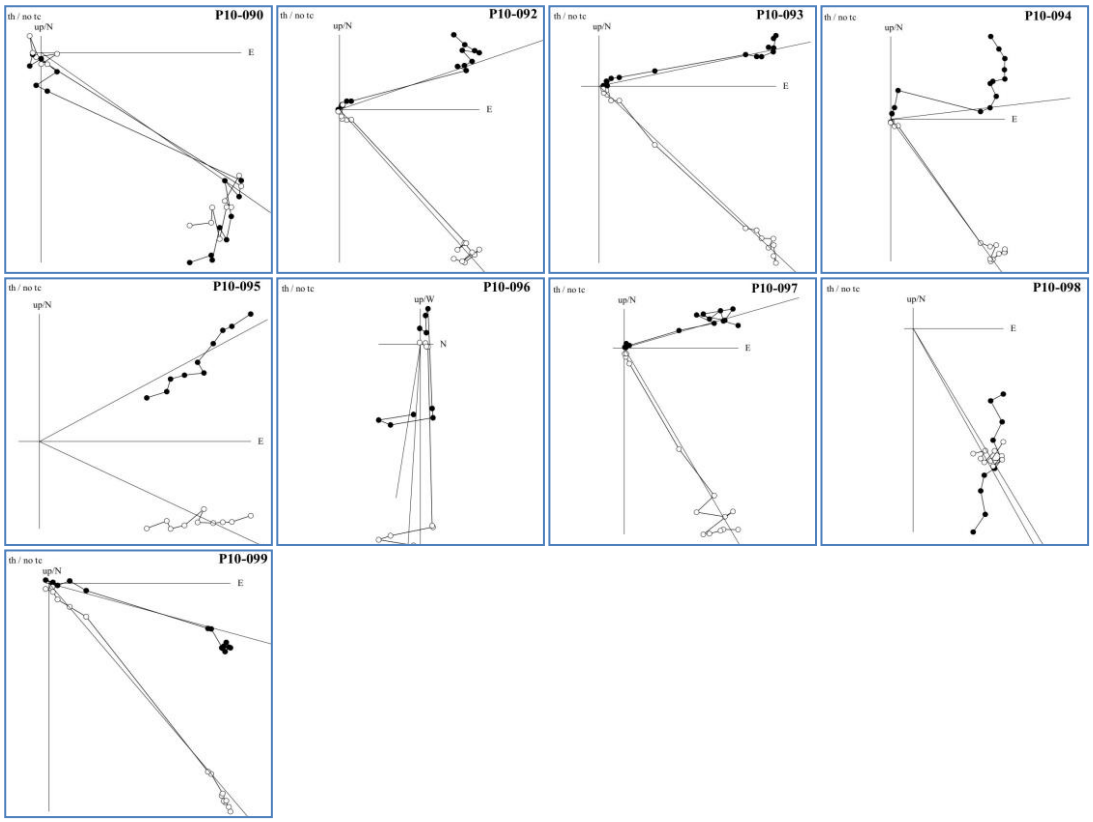

Fig 2.29a: Zijderveld diagram from site PA10.

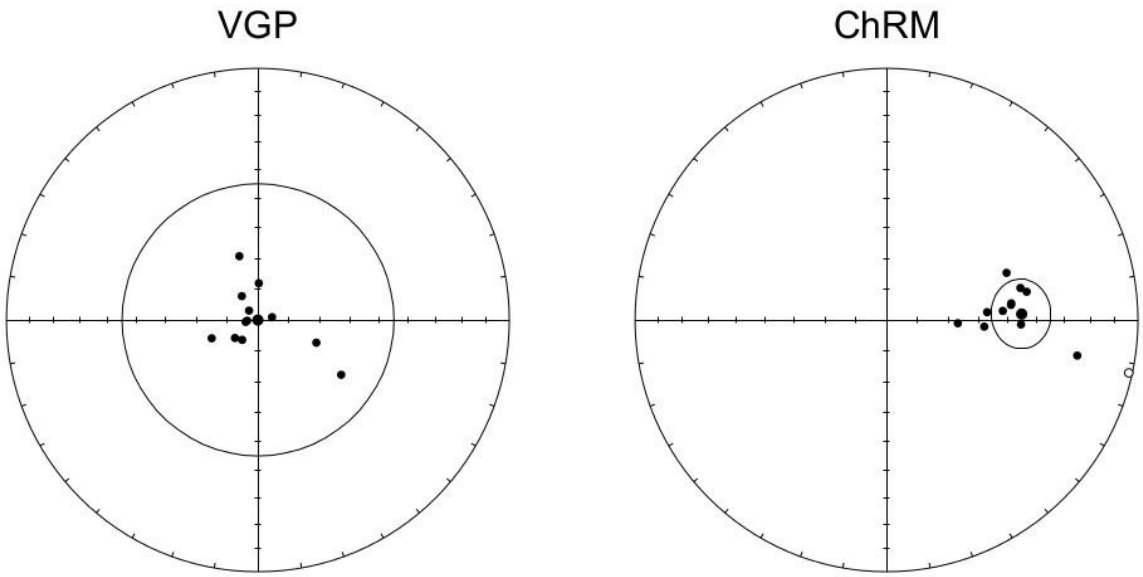

Figure 2.29b: plotted VGP and ChRM directions for site PA10.

PA 11

Two clear trends can be seen in the following diagrams. The HT component is clustered at temperatures of 450°C where the curves some times do not go through the origin (PA106, PA107, PA108). The secondary magnetization is defined at temperatures of 250°C to 270°C and 325°C for PA101 and PA104. The majority of the diagrams show a clockwise rotation direction at 72,4° with inclination values at 55,2°, while PA11102, PA11103 and PA11108 indicate differed orientations.

(Fig.2.30a) Even though the ChRM directions are well clustered the, K value for that site is very big (98,9) to satisfy the statistical requirements for that site. (Fig. 2.30b)

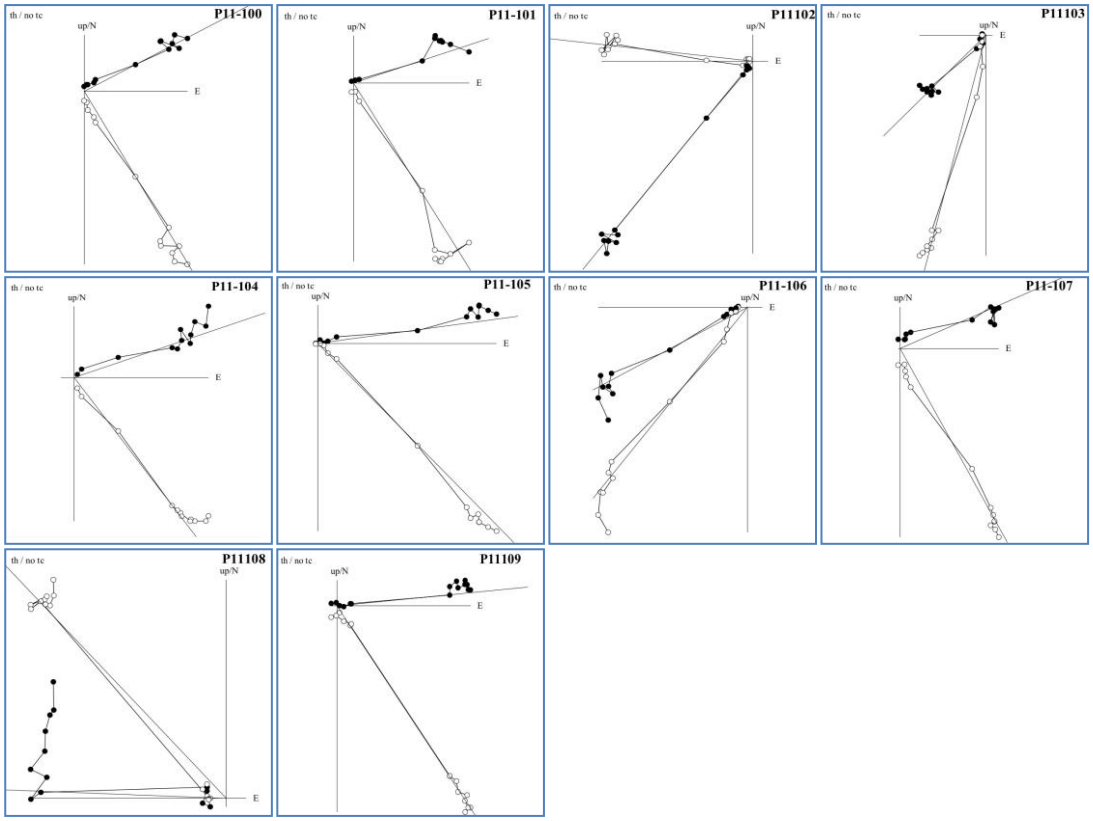

Fig 2.30a: Zijderveld diagram from site PA11.

Figure2.30b: plotted VGP and ChRM directions for site PA11.

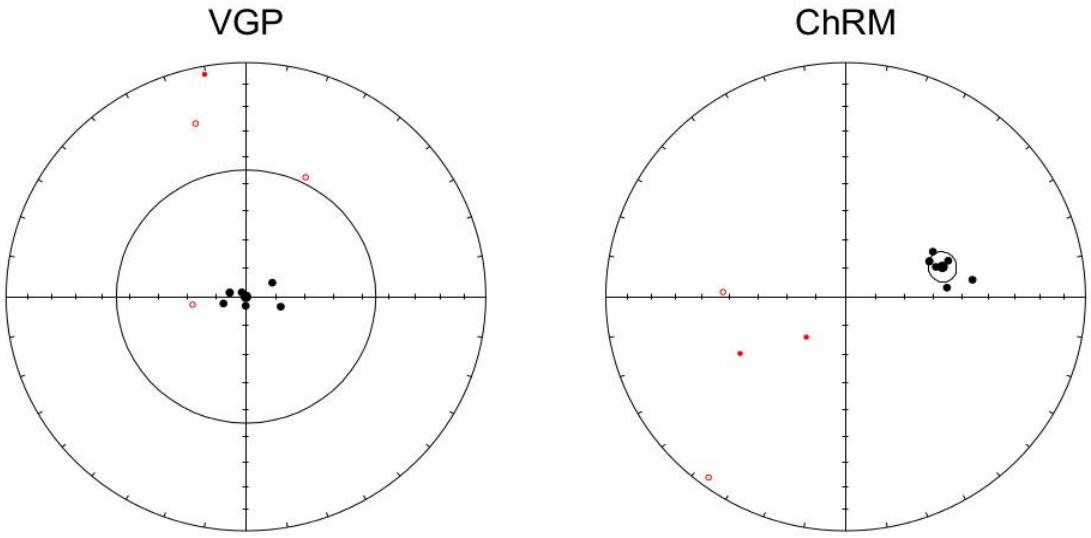

Figure2.30b: plotted VGP and ChRM directions for site PA11

PA 12

The following diagrams illustrate that the components of this site are progressively demagnetized (apart from PA12115) towards the origin at high temperatures above 625°. The declination

direction points at 351.5° and the inclination at 29.5° (Fig. 2.31a). From the 45 cut off analyses we can seen that the statistical values are acceptable (Fig. 2.32b).

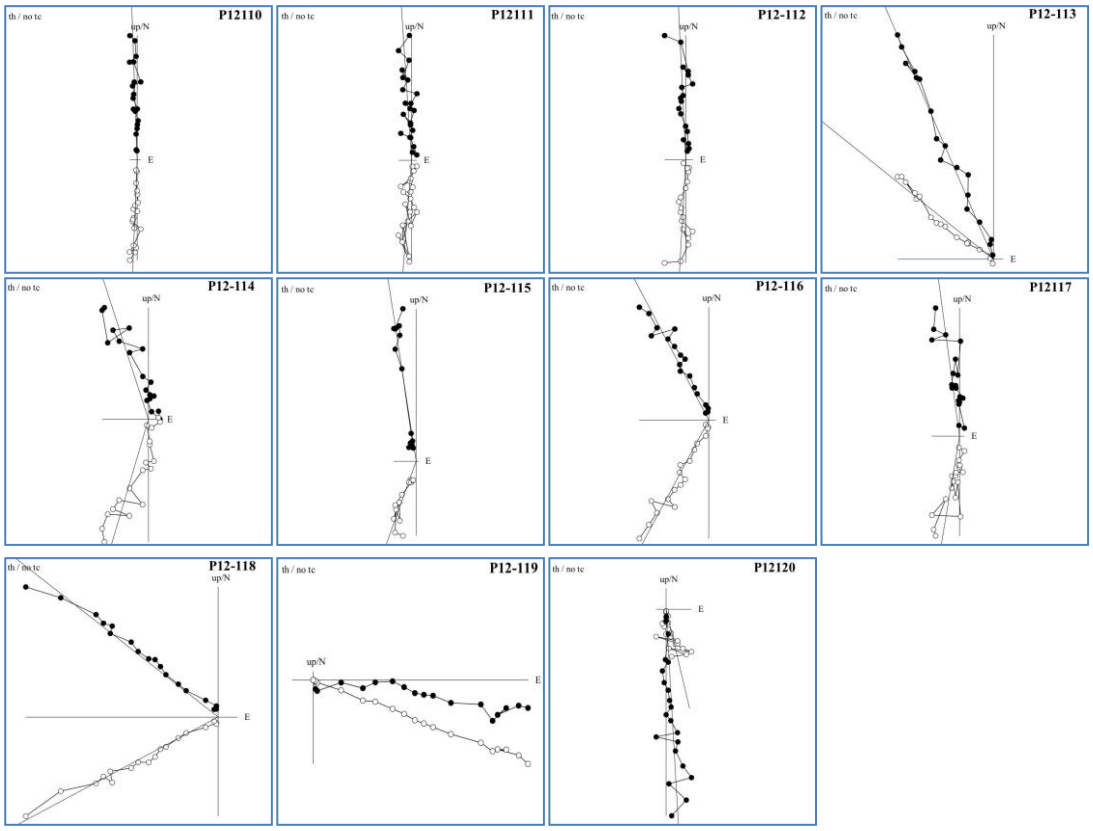

Fig 2.31a: Zijderveld diagram from site PA12.

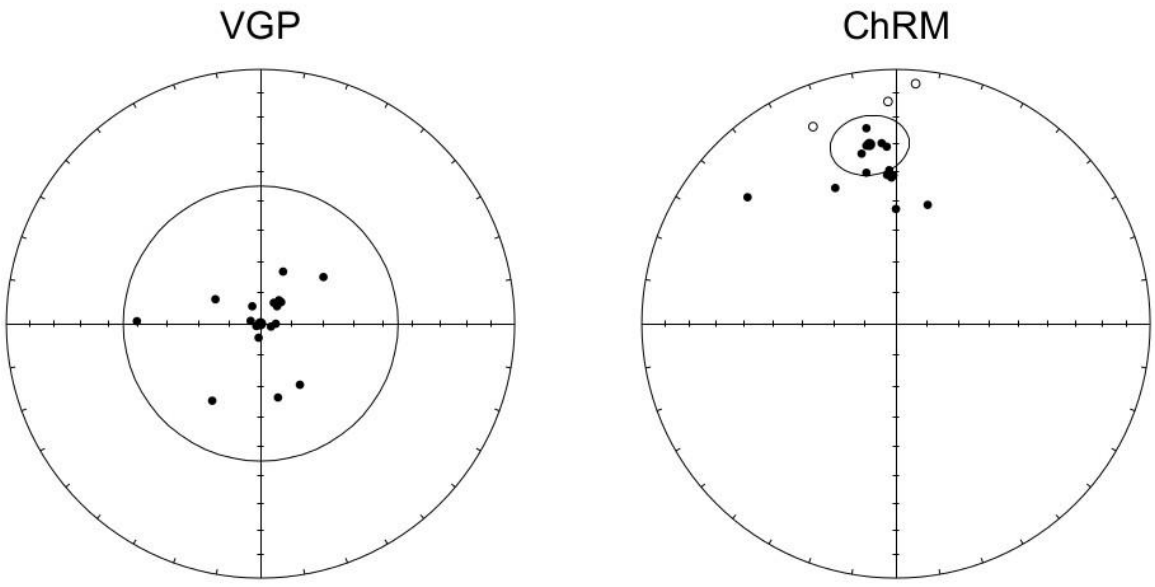

Figure 2.31b: plotted VGP and ChRM directions for site PA12.

PA 13

The thermal analyses from this site resulted in progressively demagnetized curves towards the origin. The components reach the Curie temperatures at 630 to 650° (Fig.2.32a). The ChRM directions are highly distributed in the space and therefore that site is not included for later investigation (Fig. 2.32b).

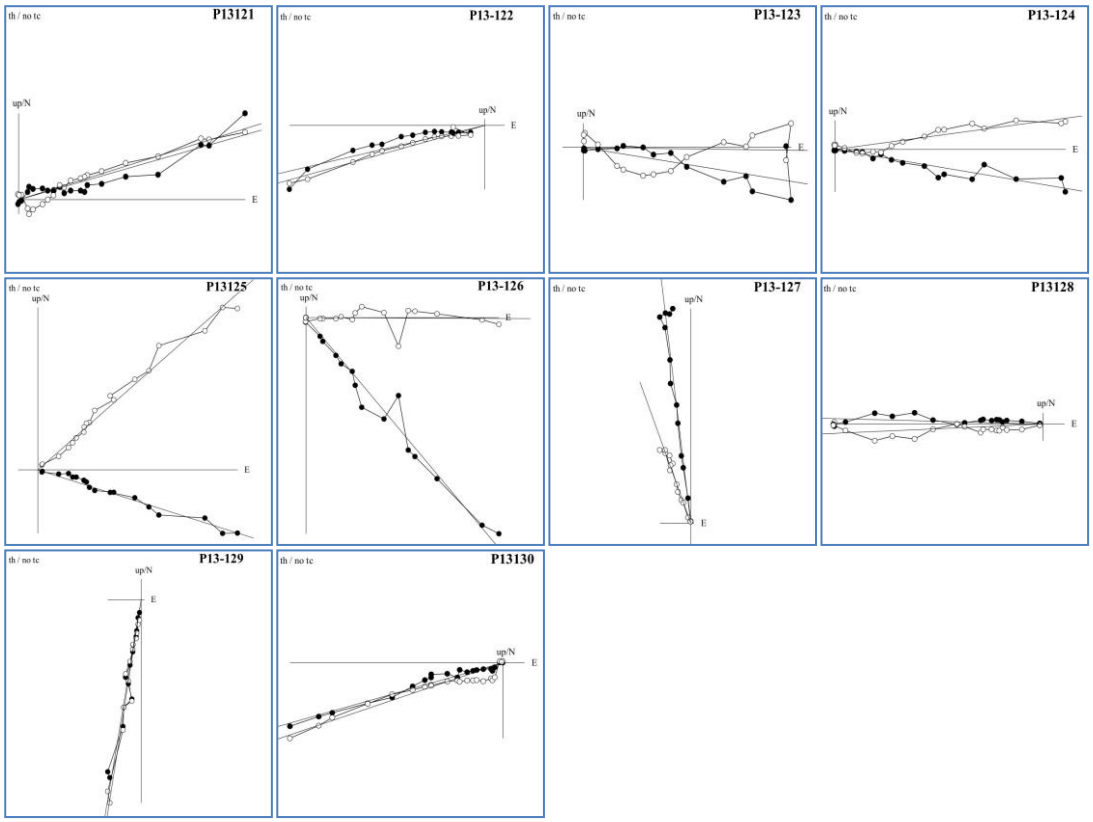

Fig 2.32a: Zijderveld diagram from site PA13.

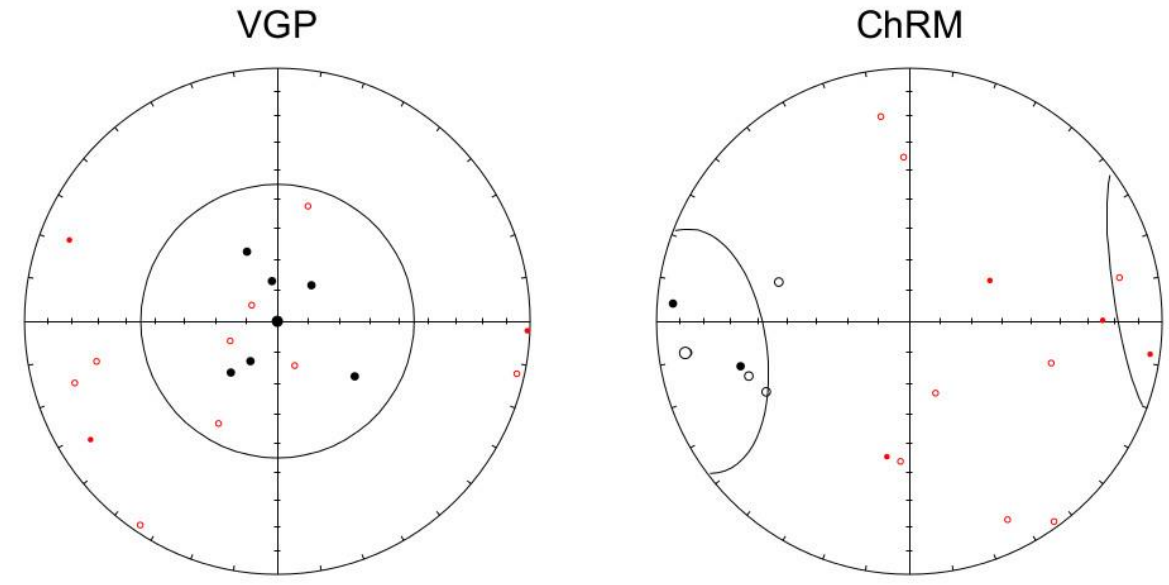

.

Figure 2.32b: plotted VGP and ChRM directions for site PA13

PA 14

The demagnetization curves for this site are divided in two parts. The HT component is defined at temperatures of 420°C - 450°C while an overprint is determined at temperatures of 250°C and only sample PA14148 shows a distributed thermal curve. The majority of the samples from present a clockwise rotation of 60,4° and inclination at 50,2°, although the samples PA14131 PA14137 PA14138 and PA14130 shows different directions.(Fig.2.33a). However the ChRM directions are slightly distributed, they show acceptable error values (Fig.2.33b).

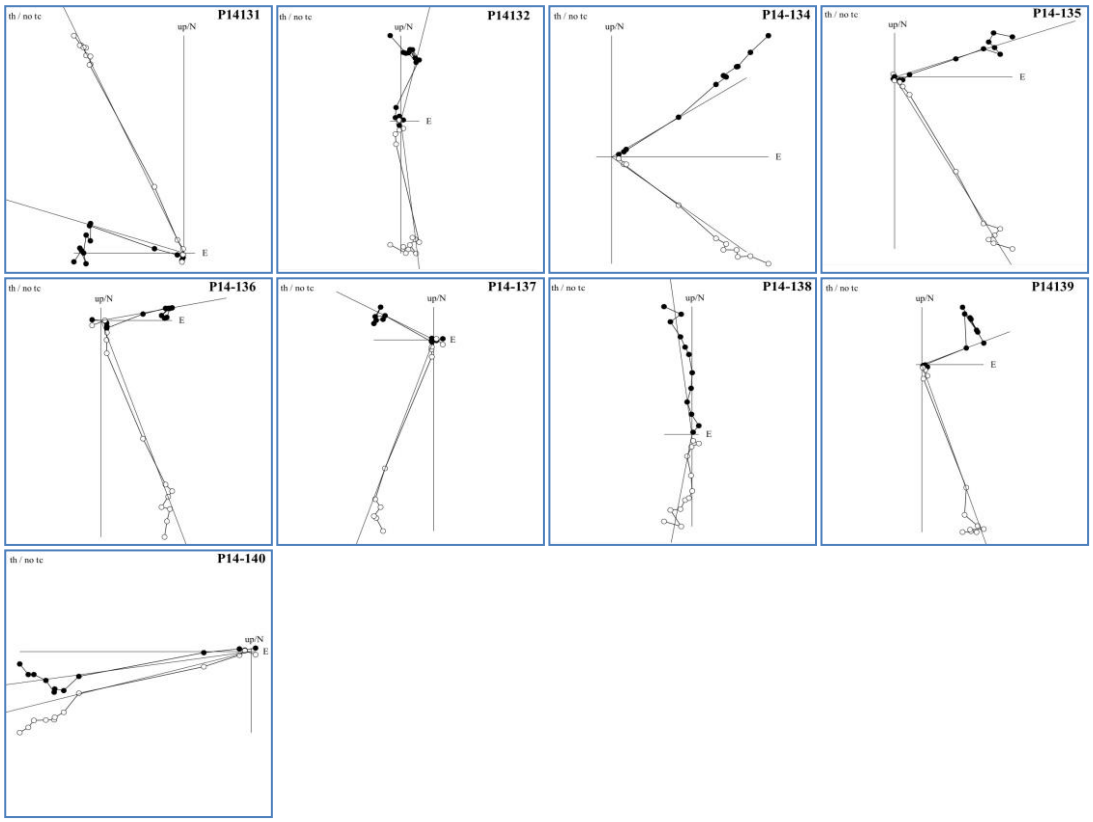

Fig 2.33a: Zijderveld diagram from site PA14.

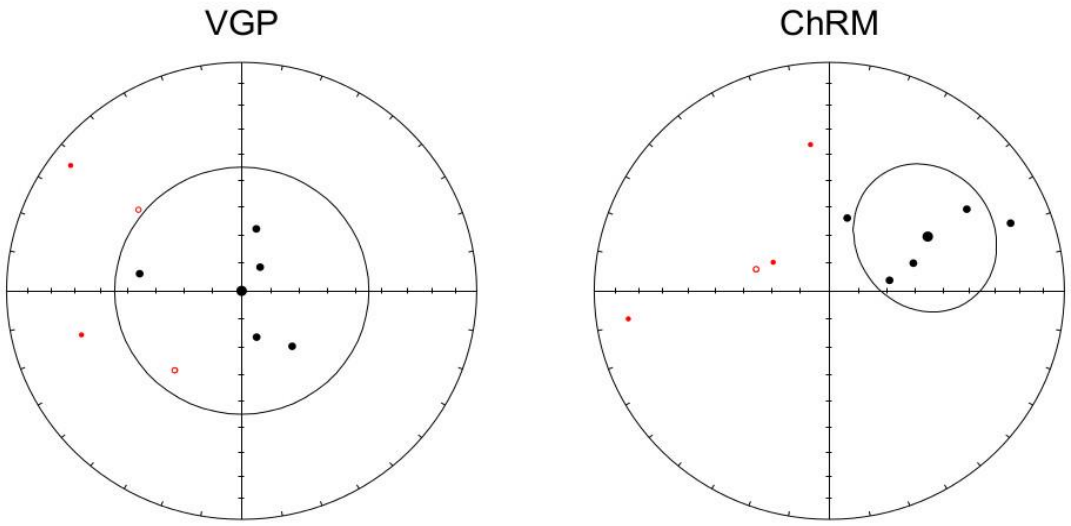

Figure 2.33b: plotted VGP and ChRM directions for site PA14.

PA 15

The analyses from the site PA15 exhibit two clear components. The LT component clusters at temperatures of 300°C while it is not possible to determine efficiently the HP component as most of the samples are not totally demagnetized. Samples PA1543, PA1544 and PA1447 reach the origin a temperature of 400°C (Fig.2.34a). The direction of the declination shows clockwise rotation of 105,2° and inclination of 40,7°. The ChRM directions are well clustered for this site (figure 2.34b).

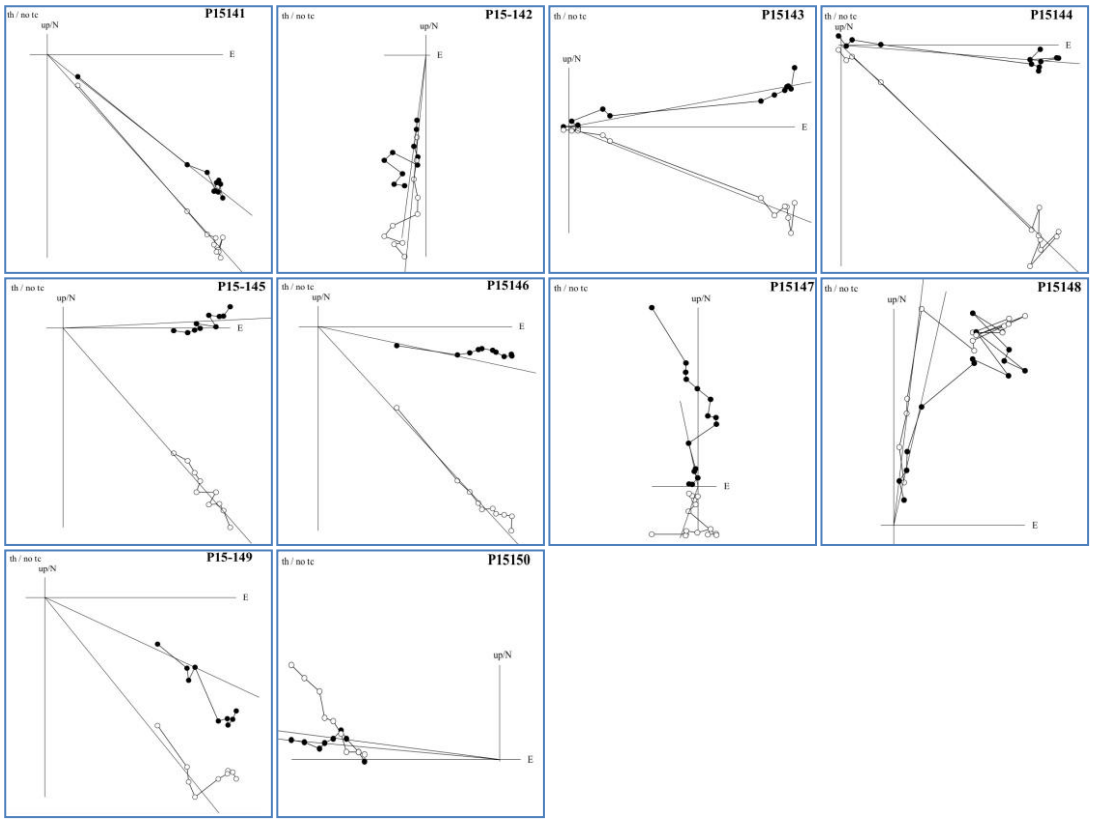

Fig 2.34a: Zijderveld diagram from site PA15.

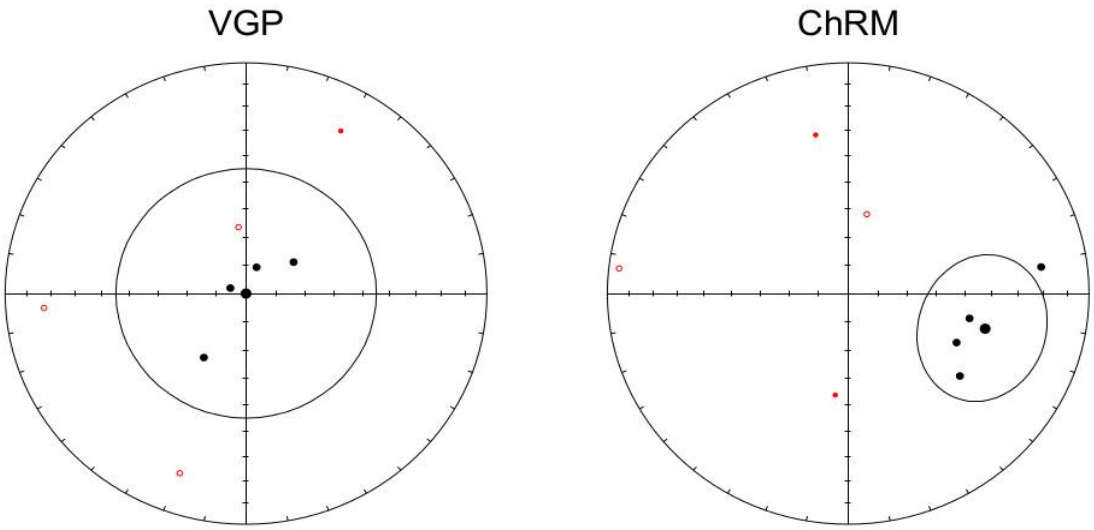

Fig. 2.34b: plotted VGP and ChRM directions for site PA15.

PA 16

The samples of that site are mainly demagnetized in two groups. There is an overprint of low temperature at 300°C. The Curie temperatures are reached up to 500°C. At times (PA16157, PA10159 and PA16160) present distributed thermal curves up to 600°C. The plotted results exhibit a clockwise rotation of 109,7° and inclination values of 40,1° (Fig.2.35a). The plotted ChRM directions are well concentrated at the same orientation with acceptable statistical values (Fig. 2.35b).

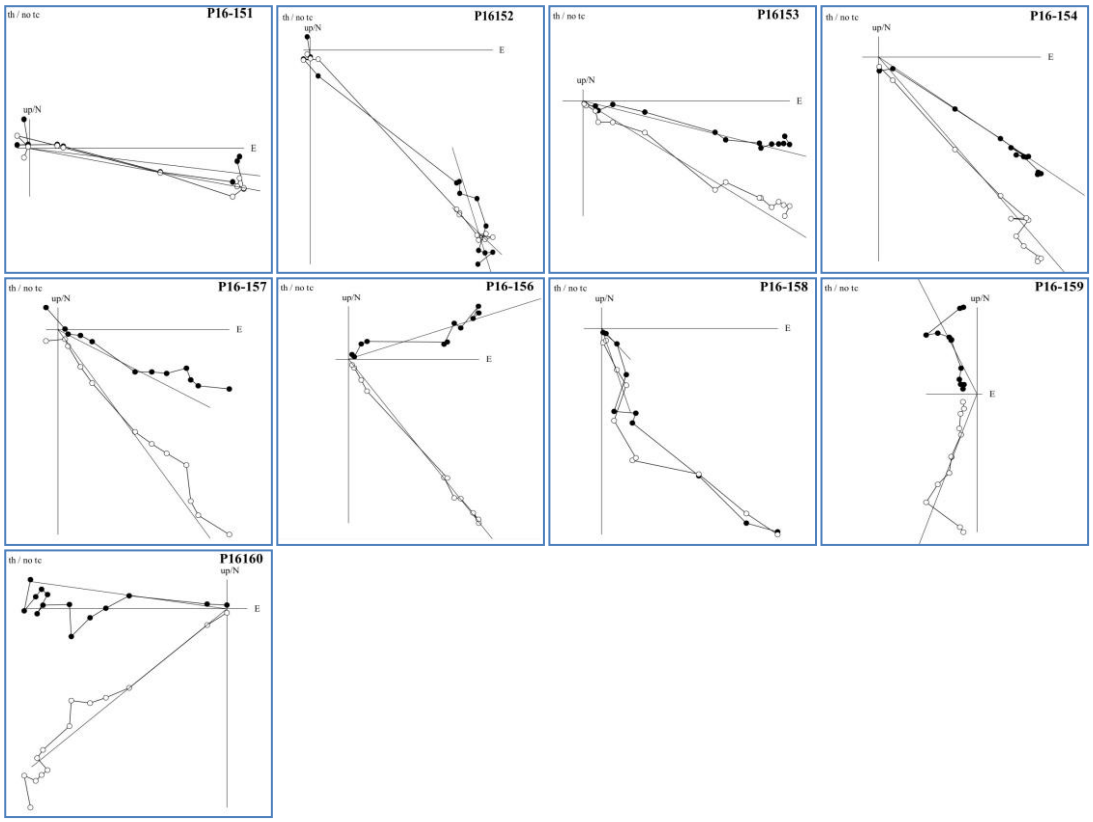

Fig 2.35a: Zijderveld diagram from site PA16.

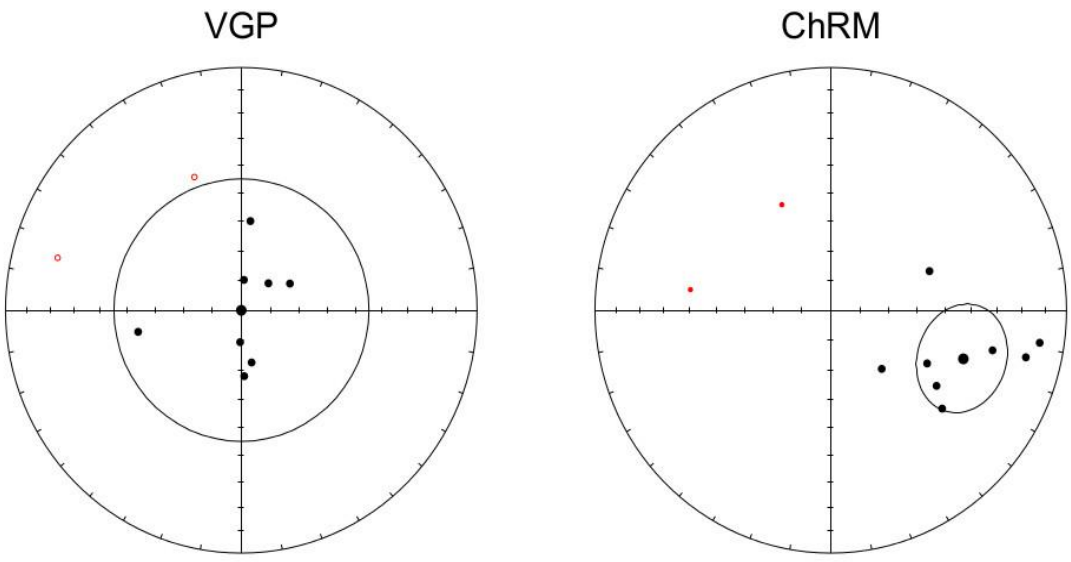

Figure 2.35b: plotted VGP and ChRM directions for site PA16.

SAMPLE	Long_WGS84	Lat_WGS84	n(m)	n(a)	dec	delta D	inc	delta I	A_{95}	K
PA1	25.18168	37.11699		11	114	12,2	52,3	10.8	10,2	21,0
PA2	25.18858	37.11835		11	97	17,1	60	10,3	6,5	27,6
PA3	25.2094	37.12557		14	64.3	8.9	51.9	8.1	7.5	28.8
PA4	25.17196	37.05601	14	7	317,2	25,2	23,2	37,7	24,1	7,3

PA5	25.21037	37.07887	15	5	14	18,7	35,9	26	9,8	28,5
PA6	25.19551	37.03913	15	7	353,9	23,1	39,2	29,8	21,3	9
PA7	25.23998	37.0162		6	334,8	21,4	22,2	37,4	26,5	11,2
PA8	25.23922	37.01716		5	352,2	15,7	19,2	28,4	15,4	25,5
PA9	25.19604	37.03738		5	331,8	26	40,1	30,5	16,4	10,4
PA10	25.20688	37.12326	12	12	87.5	9.4	45.3	10.5	8.4	27.5
PA11	25.20966	37.12692	16	7	72,4	7,5	52.2	6	24,1	98,9
PA12	25.24219	37.00694	17	17	351.5	8.4	29.5	13.3	8.1	20.3
PA13	25.20968	37.13611			no clustering, excluded					
PA14	25.21331	37.12909	16	5	60,4	31,8	50,2	29,9	26,8	9,1
PA15	25.1922	37.11962	8	4	105,2	25,9	40,7	32,2	23,6	16,1
PA16	25.17237	37.1108	15	8	109,7	18	40,1	22,8	16,5	12,2

Table 2: measured values from 45 cut off analysis.

2.4 Discussion

2.4.1 AMS

Petrofabric analyses were performed in the sampled Miocene granitoids to detect, if possible, any fabric that could affect the initial orientation of the magnetic lineations. Besides, we attempt to test whether the intrusion of the studied rocks took place during a late stage of the deformation event forming the stretching lineations. For such purposes, the measured orientations of the magnetic lineations are compared with the orientations of the stretching lineations recorded on Paros, using literature data from the work of Gautier et al., 1993 together with unpublished data. Furthermore, the magnetic foliation is analyzed in correlation with the structural characteristics of the host rocks.

The results from AMS analyses display a well-developed magnetic foliation plane, except sites PA6 and PA12 and PA13, where either the magnetic lineation is dominant or they show a high susceptibility. Samples show an oblate fabric (T>0), while sites PA4 and PA7 show a triaxial fabric, where both the magnetic foliation and lineation are poorly developed. In magmatic rocks such a variation may be related to post-emplacement processes, either associated with the flow of magma in the host rocks or due to tectonic reasons. Extension in ~N-S direction can explain the magnetic foliation and lineation.

Concerning the magnetic lineation, the sites PA7, PA8 and PA12 present a clear N-S orientation, while sample PA3 trends approximately E-W. The source of such orientation of the magnetic lineation is likely tectonic, although the possibility of magmatic flow cannot be excluded. This study assumes that tectonic forces controlled the magnetic mineral preferred orientations. Sites PA1, PA2, PA10, PA11, PA13, PA14, PA15 and PA16 in the northwest Paros, and the sites PA4, PA5, PA6 and PA9 in the central part of the island show poorly clustered orientations of the magnetic lineation, indicating that those samples have not experienced significant ductile deformation (Fig.2.36).

The host rocks of the granites show ductile fabrics defined by a pervasive metamorphic foliation (Gautier et al., 1993; Avigad et al., 2001). Although, the Miocene granites do not show a clear foliation, a weak fabric is determined from the AMS analysis. This observation suggests that the regional ductile deformation was strongly partitioned in the host rocks and in minor extent into

the Miocene granitoids. Taking into consideration the above information, we conclude that the granitoids intruded late in the regional deformation event that caused the regional stretching on the rocks. Furthermore, comparison between the orientation of the magnetic lineations and stretching lineations in the northwestern and the southeastern part of Paros, reveals that both orientations are parallel in the corresponding parts of the island. As a result, both the stretching and the magnetic lineations were affected by a dominant post-emplacement tectonic event resulted in the change of their orientations.

2.4.2 Magnetic carriers

Curie-balance measurements and decay-curves of the demagnetized samples shows that the main magnetic component is a titanomagnetite with various compositions. Instead sites PA6, PA9, PA10 and PA16 contain iron sulfides with minor fraction of low-Ti titanomagnetite. The obtained Curie points are up to 350°C for samples PA1, PA2, PA4, PA5, PA8, PA11 and PA14, while sites PA7, PA15 and PA16 display temperature up to 500°C. Sites PA12 and PA13 indicate much higher temperatures reaching up to 690°C. These two sites are not granites but quartzitic vein (sample PA12) and rhyolite (sample PA13) containing hematite.

The measured rotations in the Miocene granitoids occurred after the granitoids cooled below the Curie temperatures of the dominant carriers (i.e. below 500°C to 350°C). As a result we can infer that structures accommodating these rotations operated at metamorphic grades not higher than greenschist facies.

2.4.3 Rotation

To define if vertical rotations occurred on the Island of Paros, the paleomagnetic declination of the sampled rocks was measured and compared with known stretching lineations. Progressive thermal and alternating field demagnetization techniques were applied to measure the paleomagneitic declination and inclination of the samples. The measured declination and inclination values give accurate results within the acceptable error for all sites, except site PA13. This sample shows high intensities but with scattered orientation of the declination directions, indicating corruption by lightening. This site is therefore excluded from further investigation.

Sites from the northwest part of the island consistently show clockwise rotation, largest in the west at ~100°, decreasing eastward to ~75°. The results from the southeastern Paros show a mean declination of 351.5° +/- 3. This shows that there is a ~100° rotation difference between the NW and the SE part of the island. The orientations of the stretching lineations agree with the orientation of the paleomagnetic declinations (Fig. 2.36). Consequently, it can be concluded that all stretching lineations on Paros were originally oriented ~N-S trending, and only rotated after granitoids intrusion with an approximate 90° rotation in the northwestern part and 10° anticlockwise in the southern of Paros (Fig.2.36).

2.4.4 What structure accommodates the rotation?

According to the measured paleomagnetic declination values we conclude that a 100° rotation difference between the northwestern and the southeastern part of Paros occurred. Petrofabric analyses on the magnetic mineral preferred orientations in comparison with the orientation of the

stretching lineations of the Miocene granites, suggest that the rotation of those rocks occurred after their intrusion between 12 and 17 Ma. Thermomagnetic measurements show that the rotation occurred below temperatures of 350° and 500°C after granites cooled down. This range of temperatures is typical of the greenschist facies.

Based on the above-mentioned findings, the structure supporting the rotation difference on Paros operated in the upper crustal levels between 13 and 18 km, at the ductile to brittle transition. Such a structure, coincides with the tectonic contact between the metamorphic rocks of Marathi Unit and the Pre-Alpine basement in the northwestern part of the island (Fig. 2.36) comprising a low angle normal fault (detachment) dipping to the south (Papanikolau, 1980; Lister et al., 1999 and Lister et al., 1996). The strain on this detachment fault was preferentially partitioned along the gneiss-marbles boundary forming mylonites and ultramylonites (Papanikolaou 1980; Gautier et al., 1993). Ductile fabrics between the metamorphic lithologies of Marathi unit and the Pre-Alpine basement are parallel or sub-parallel, and occasionally low angle ductile shear zones cross-cut the contact (Kostis, unpublished). Locally, low angle normal faults overprint previous ductile structures. In fact it is reported the presence of tectonic breccias and cataclasites composed of the overlain rocks (Papanikolaou 1980; Gautier et al., 1993., Lister et al., 1999).

In conclusion, this SE dipping detachment fault initiated at depth in the ductile regime and evolved up to shallower brittle conditions in a progressive movement, accommodated the vertical axis rotations that took place on Paros after 12-17 Ma, as it is supported by the paleomagnetic study.

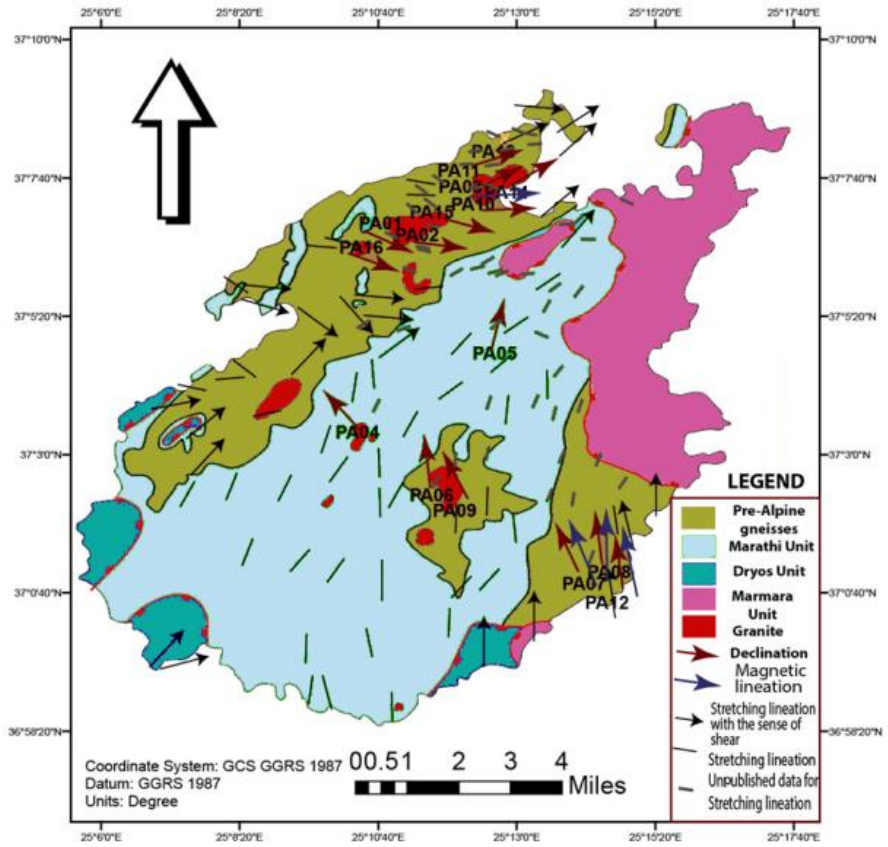

Figure: 3.36: Geological map of Paros presenting the stretching lineation, the magnetic lineations, the paleomagnetic declination and the structure separating the two domains

PART 3: PETROLOGY

3.1 Introduction

A crustal thinning regime dominated the Aegean region in the middle –late Oligocene period, resulting in widespread extension and exhumation of previously buried rock formation in core complexes (Lister et al., 1982; Foster et al., 1999).

The exhumation took place in two stages; an early uplift followed by a mid to high temperature overprint (van Hinsbergen et al., 2005; Brun and Faccena 2008; Jolivet and Brun 2010). The first stage involves the exhumation of basic rocks metamorphosed in the eclogite to blueschist facies, reaching a metamorphic peak at around 20 Kbars during late Eocene. During Oligocene – Miocene in a later stage, an increase of the temperature led to a retrograde overprint in the greenschist facies. The temperature during that phase reached regionally high temperatures leading to partial melting and migmatisation (Paros, Naxos) (Jansen and Shuiling 1976, Vanderhaeghe et al., 2007), while the whole extensional phase was accompanied by plutonic and volcanic activity (Pe-Piper and Piper 2001). The upper crustal rock formations record a non-to-low metamorphic grade as they were slightly or not affected by the Eocene subduction (Jolivet at al., 2010).

The exhumation of the metamorphic core complex in Cyclades was accommodated by large low angle detachment faults (Lister and Foster 1999; Jolivet et al., 2010). Several kinematic indicators suggest top-to-the-N shear sense (Gautier et al., 1989, 1990; Urai et al., 1990; Buick, 1991), except in the NW part of the island of Paros, where a to top-to-the-E/ESE shear sense is accompanied by a progressive rotation of the lineation trend (Gautier and Brun 1994; Jolivet et al., 2004). Specifically, in the northwest lineations trend NE – SW, while in the southeast lineations trend N – S.

Walcott and White (1998), in order to explain the change of the lineation trend in the Cyclades, proposed the existence of a mega-structure called the 'Mid Cycladic Lineament' (MCL). Such a structure is supposed to represent a conceptual border separating two lithospheric-scale domains, recording two different orientations of the stretching lineations. Although the change of the stretching lineation is reported by several authors (Gautier et al., 1993; White and Walcott 1998; Avigad et al., 2001), the presence of the MCL is still under debate.

The aim of this study is to provide any possible petrological indication supporting the existence of the Mid-Cycladic Lineament. The study area is focused on the island of Paros (Central Cyclades), as it comprises the only location where both directions of the stretching lineation have been reported. In order to confirm or dismiss the existence of the MCL, it is attempted to define any relation between the high grade metamorphic unit (Marathi Unit) and low grade metamorphic unit (Dryos Unit) of Paros ,questioning if they represent two distinct metamorphic units or they are both part of the same progressive exhumation stage.

In order to define the metamorphic conditions of the rock samples the stable mineral assemblages of the rocks are examined in thin sections. For this purpose thirty eight samples were collected in the field and cut perpendicular to the measured foliation plane and parallel to the lineation, where possible. The thin sections are studied using optical

microscopy techniques to recognize the minerals and the relationships between them. The results are depicted in tables showing the stable mineral paragenesis for each sample.

For a further investigation six samples are used for chemical analysis performing Electron Microprobe (EMP) technique. A JEOL JXA-1800 Superprobe equipped with an energy dispersive detection system and five wavelength dispersive spectrometers (WDS) at Utrecht University is used for such analysis. Carbon coated thin sections were initially analyzed with Energy Dispersive Spectrometry (EDS) for quick identification of minerals and Wavelength Dispersal Spectrometry (WDS) for high resolution analysis.

3.2 The Island of Paros

3.2.1 Tectonistratigraphy

The island of Paros (southern Cyclades) lies within the central part of the Aegean Sea (Fig.1.1). Three units with complex tectono-stratigraphic configuration are distinguished on the island (Papanikolaou 1977; Papanikolaou 1980). Lithological and structural characteristics differ considerably from unit to unit where both footwall formations and hanging wall sediments are exposed (Bargnesi et al., 2012).

Cycladic Basement:

The Cycladid Basement is the lowest tectonostratigraphic unit on Paros involving a Pre-Alpine orthogneisses. The pre-Alpine orthogneisses are dated 325-302 Ma (Engel and Reischmann, 1998) and shows optimal correlation with the orthogneisses (lowest units of the CBU) in Naxos, Ios and Sikinos (Philipon et al., 2012).

Marathi Unit

The orthogneisses are overlain by Mesozoic formations (high grade metamorphic Unit) of Marathi Unit which outcrops mainly in the central part of the island and it is assigned to the Cycladic Blueschist Unit (Bargnesi et al., 2012; Avigad, 2001; Gautier et al., 1993). The Marathi Unit can be further subdivided in two groups. The lower group includes amphibolites, amphibolitic schists intercalated with thin layers of impure marbles, quartzo-feldspatic rocks and micaschists (Papanikolau, 1980), while the upper one consists of marbles and metabauxites. Lithologies indicative of a transitional character between the amphibolites and the marbles are present in both two groups (Robert, 1982). All the above formations are highly deformed and intruded by Miocene S-type granites and pegmatitic dykes (Stouraiti et al., 2010; Altherr et al., 1982). Radiometric dating shows that magmatic intrusions within the basement orthogneisses and the high grade metamorphic rocks of Marathi are syn-to late tectonic with the deformation occurred 16 Ma (Bargnesi et al., 2012).

Dryos Unit

Dryos Unit overlays Marathi Unit and is characterized by limited exposure, showing a great

heterogeneity within its lithologies. Metabasites, calcareous rocks, phyllites and schists are the main lithological types which underwent low to medium metamorphism, up to the greenschist facies (Avigad et al., 2001). The formations are normally highly schistosed and folded, while close to the contact with Marathi Unit a well-developed mylonitic fabric is present (Papanikolaou, 1980; Gautier and Brun, 1994). Furthermore is reported the presence of Permian fossils within the marbles (Papanikolaou 1980)

Marmara Unit

The northeastern part of is occupied by Marmara Unit, the upper stratigraphic unit of the island. Field relationships reveal a clear tectonic contact juxtaposing Marmara (hanging wall) against both Marathi and Dryos Unit (in the footwall). This unit consists of two parts, the non-metamorphic Alpine rocks (lower part) and the Neogene supra-detachment clastic formations (upper part) (Avigad 2001; Sanchez-Gomez et al., 2002). Serpentinised ophiolites, clastic formations and Cretaceous limestone are present in the lower part, while coarse grained sediments with conglomerates, sandstones and sandy marls forms the upper part.

Dating of deposition suggests that the Cretaceous limestone is allochthonous and comprises an olistolisth into the basin (Bargnesi et al., 2012). Although the lower clastic formations reveal a marine character, the upper layers gradually shifted to continental environment deposition (Sanchez-Gomez et al., 2002). A low angle detachment fault brings the non-metamorphic formations (supradetachment deposits and Marmara Unit) into contact with the metamorphic formations of both Marathi and the pre-Alpine basement (Lee and Lister 1992; Brun et al., 1993; Jolivet et al., 2010).

Quaternary deposits

The stratigraphic column of Paros completes the Quaternary depositions with no any association either with the alpine orogenesis or the post-Alpine orogenic collapse. In the eastern part of the island slightly deformed travertine overlays uncomfortably all the pre-existing above mentioned formations (Papanikolaou 1980). Finally, Quaternary formations involving alluvial and fluvial-torrential sediments covers are an important part of the island.

3.2.2 Deformation

The long and complex geological history of Paros results four deformation (D1-D4) events associated with different metamorphic conditions.

D1

The oldest deformation phase cannot be detected on the field, but is only inferred by correlation with the corresponding units of the neighboring island of Naxos (Robert 1980).

According to that, the Marathi unit, which belongs to the Cycladic Blueschist Unit, underwent high-pressure deformation as it can be inferred by the rare high-pressure relics that have been found in related rocks in SE Naxos (Jansen 1976; Andriessen et al., 1979, Avigad 1998). Structures and mineral assemblages of that early phase in Paros have been overprinted by the younger syn-metamorphic D2 event that had a strong impact on the final geometry of the island.

D2

The D2 syn-metamorphic deformation phase resulted in isoclinal refolded folds showing a gradual change on their fold axis from the western to the eastern part of the island (Avigad et al., 2001; Papanikolaou 1980). Fold axis strike from ENE-WSW to ESE-WNW dipping to ENE and ESE respectively in the western part of the island, while folds are overturned to the west in the eastern Paros (Gautier et al 1993; Avigad et al., 2001). Moreover, during that stage the main foliation S2 is formed and well expressed in the main axial plane (Papanikolaou 1980). The L2 stretching lineation developed on the main foliation S2, displays a gradual transition from the western to the eastern part of the island. In the western part L2 strikes WNW-ESE plunging to ESE changing progressively to NE-SW. On the other hand, in the central and eastern part the stretching lineation trends N-S plunging either to the N (central part) or to the S (eastern part) (Walcott and White, 1998). The change of the lineation is consistent with the change of the fold axes (Papanikolaou 1980).

D3

D3 deformation is the progressive continuation of the previous event showing both brittle and ductile characteristics. During D3, the S2 schistosity is deformed by S-C structures and L3 stretching/intersection lineations are developed (Avigad et al., 2001). The trend of the L3 stretching lineation is not constant but it changes progressively. (Gautier and Brun, 1993). In the western part of Paros the L3 lineation is preferentially oriented WNW-ESE, while in the eastern and central part trends NE-SW and N-S respectively. Field observations as C' type shear bands and boudinage are the result of the D3 phase (Gautier and Brun, 1993; Avigad et al., 2001). Additionally, protomylonitic, mylonitic and ultramylonitic structures that are observed both in the Marathi and in the Dryos units, and the character of the contact between the lower and the upper units defined by a fine grained gouge, are all attributed to D3. Finally, extensional shear bands that gradually evolve into low-to-medium angle cataclastic surfaces characterize the late stage of D3 deformation.

D4

D4 structures postdate all the previous events with clear cross-cutting relationships in a post-orogenic regime. Brittle structures comprise cataclastic fractures, extensional zones,

faults and folds in a meso-to-macroscopic scale (Sanchez-Gomez et al., 2002; Gautier et al., 1993). Open upright folds striking NNE-SSW to NE-SW are accompanied by a disjunctive cleavage. A dense net of fractures with a small displacement characterize fault zones. The trend of such structures differs locally, but they always strike perpendicular to the stretching lineation (Gautier et al., 1993). The fractures are filled with calcitic and material forming veins in the formations.

3.2.3 Metamorphism

According to field and microscopic observations three metamorphic events have affected the lithologies on Paros.

M1

The characteristics of M1 cannot be directly found because they have been heavily overprinted by younger metamorphic events. Only a correlation with metamorphic units from the island of Naxos can shed some light on early stages of metamorphism and deformation. The presence of phengite, glaucophane, jadeite, and diaspore in the metabauxites in Naxos is indicative of a paragenesis equilibrated at high pressures (LT/HP) typically found in the outer Cycladic Islands (Robert, 1982, Avigad 1998). That metamorphic event took place at 45±5Ma (Andriessen et al., 1979) at 12 Kbar and at 470° C (Avigad 1998; Jansen 1977). Recent re-interpretations in other islands, defined this HP metamorphism to occur around 50 Ma at roughly 550 °C (Fig.3.2).

M2

The M2 phase is characterized by retrograde assemblages re-equilibrated in greenschist facies and in Paros and Naxos reached up to upper amphibolite facies (Fig.3.2). A few outcrops are preserved in the southern part of the island due to its greater distance from the migmatitic dome characterizing the M3 medium-temperature overprint.

M3

The M3 parageneses are defined by mineral assemblages typical of amphibolite/greenschist facies. Orthogneisses belonging to the pre-Alpine basement are characterized by a stable mineral assemblage Qz+Feld+Bt±Ms (Robert, 1982). The High Metamorphic Unit (marble-amphibolites) of the Marathi Unit is mainly composed of metric to pluri-metric layers of alternating marble and amphibolites. Impure marble, calcschists are prevalently formed by different proportions of calcite, chlorite, muscovite, green hornblende, garnet, scapolite and clinopyroxene. A detailed study on amphibolites and greenschists by Robert (1980) revealed a neat metamorphic gradient, varies from North to South in three distinct metamorphic areas belonging to the same event (Fig.3.3):

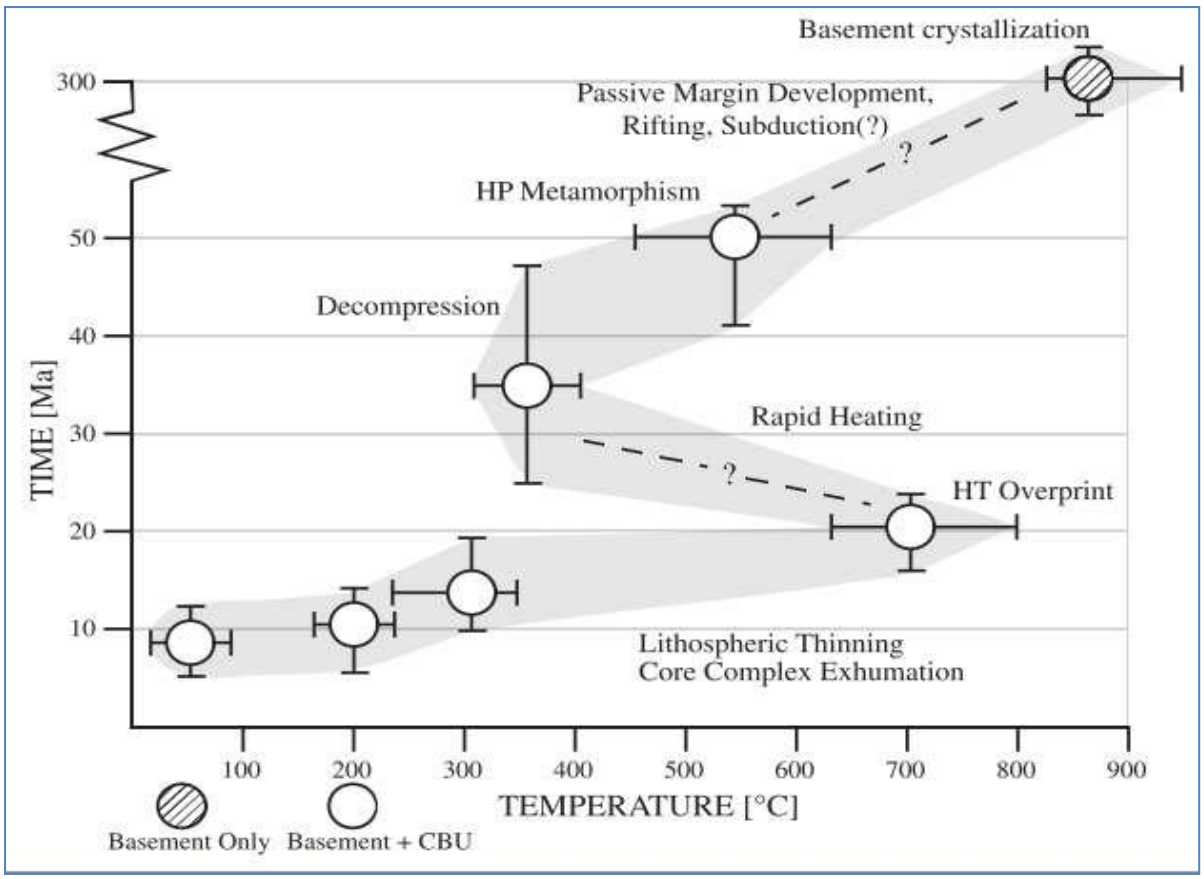

Figure 3.2: Diagram illustrating the tectono-metamorphic evolution of the Variscan basement and CBU during the alpine orogeny in the Aegean area (Bargnesi et al., 2012).

Zone A:

Greenschists facies of the southern part of the Island

Stable mineral assemblage: Chl+Ep+Ms ±Grt±Green Hbl

Zone B:

"Lower" Amphibolite zone, divided from the zone A by the concomitant disappearing of Chlorite and muscovite associated with the appearance of green hornblende and garnet.

Stable mineral assemblage: Ep+Grt+Green Hbl±Scp

Zone C:

"Upper" Amphibolite zone is distinguished from the zone B by the presence of diopside and scapolite.

Stable mineral assemblage: Grt+Green Hbl+Scp+Di±Ep

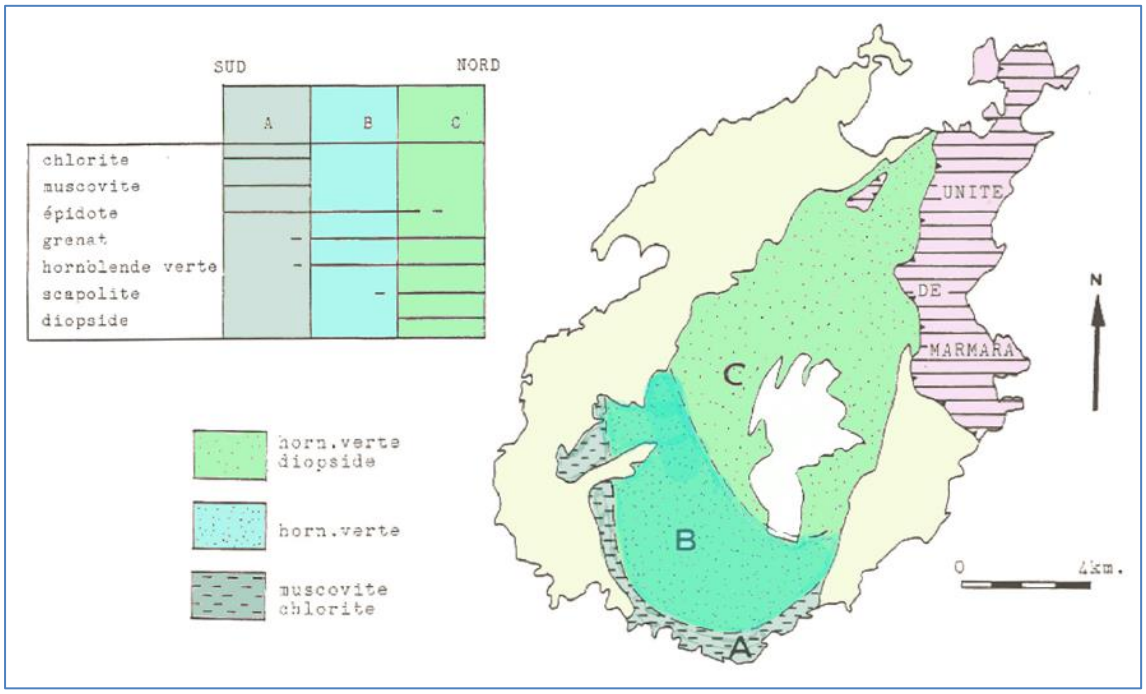

Figure 3.3: Geological map of Paros showing the metamorphic grades of the island according to Robert (1980).

3.3 Results

3.3.1 Field observations

Thirty eight samples (38) were collected from the field from both high and low grade metamorphic units (Marathi and Dryos units respectively) (Fig.3.4). The locations, lithology and number of samples that were gathered directly from the outcrop are depicted in Appendix 3.4. The samples 23, 25, 30, 31 and 34, collected from Marathi unit, were highly altered and weathered and therefore they are excluded from that study. Thirty-three (33) samples were cut and prepared for thin sections while six (6) of them were used for chemical analysis.

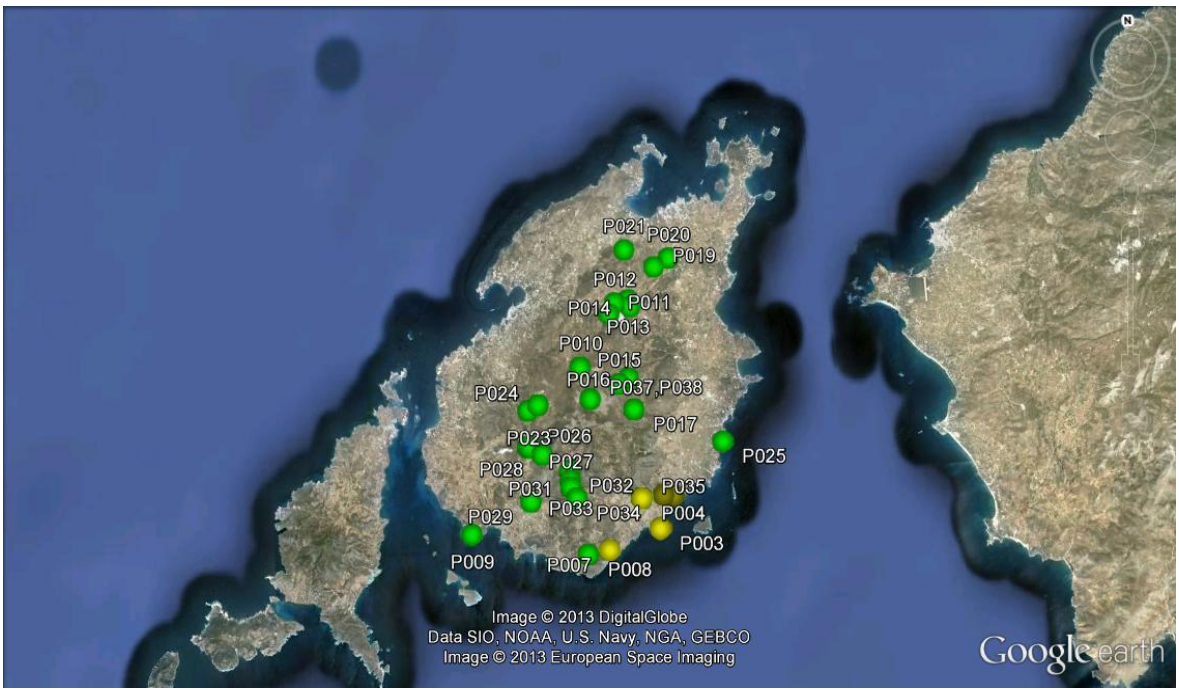

Marathi unit

The lithological types collected form that unit comprises amphibolites, mica schists, gneisses, amphibolitic schists and greenschists.

Amphibolites

This lithology shows a lithological variety in the field. The common observed mineral assemblage in the field is green amphibole, plagioclase and opaque minerals. Some samples may also contain garnet, quartz, brown mica (biotite) and epidote. They are medium to coarse grained size and generally dark colored, although, the differentiation in their mineralogy attributes them a variety in color from dark green to dark grey.

The amphibolites are deformed displaying a well expressed foliation. Their elongated minerals define a lineation on their main foliation plane while in some occasions more than one lineation can be observed.

That rock type is usually intercalated with marbles while some outcrops show an indeterminate and probably transitional character between amphibolite and marble (samples 10, 12 and 20). Thin calcitic, aplitic and quartzitic veins cut the formations in random directions. It is also observed that outcrops close to aplitic veins are slightly different as the feldspar is coarser grained and more rounded comparing other exposures (samples 15, 16). Moreover, some exposures (samples 18) display migmatitic characteristics showing a differentiation between felsic and mafic minerals.

Amphibolitic schists

That lithological type is distinguished by the previous one by its color and its slightly different mineralogy (sample 33). It contains amphibole, feldspar and higher percentage of mica compared to the amphibolites. Quartz and garnet are included as well. It is lighter colored and finer grained size than the previous type. The rock samples are highly deformed and strongly foliated. They are cut by calcitic and aplitic veins. The exposures are highly weathered and altered.

Figure 3.5: On the left coarse grained amphibolite, cut by slightly discordant granitic vein. On the right: amphibolitic rock, highly deformed and altered.

Mica schists

That rock has been collected from the southern and western part of the island very close to the contact with Dryos Unit (sample 7). It is composed by mica, feldspar, quartz and garnet. It is fine grained size and of brown color. Porphyroclasts of garnet are coarse grained and deformed while the feldspar forms eye shapes and σ clasts. The mica rich component attributes a distinct shiny shine in the rock surface.

The outcrop is highly deformed displaying a well-developed foliation. Its crystal shape and size together with observed shear bands indicates mylonitic deformation.

Gneiss

That lithology is selected from the central part of the island (samples 17, 38, 37). They are characterized by coarse grained minerals and large eye shaped feldspar. Their main mineralogy is composed by quartz, feldspar, mica and opaque minerals.

The samples develop a gneissic schistosity exposing mica and gneiss are slightly deformed

while foliation is not always well defined. They display S-C fabric and they are intruded by aplitic and pegmatitic veins and close to the intrusions locally they display migmatitic characteristics. That rock type is coherent and foliated. A well-developed compositional layering can be observed composing by light bands composed of quartz and feldspar alternating with mica - rich bands. The grains in the felsic bands are rounded to lenticular while elongated brown mica compose the dark layers. It is intruded by granitic veins and as well as thinner aplitic, pegmatitic and calcitic veins in random directions. Locally, it may display migmatitic characteristics.

Figure 3.6: On the left: mica schist. On the right: Gneiss

Greenschists

This rock type was collected from the southern part of the island and close to the contact with Dryos unit showing typical characteristics of that facies (samples 26, 27, 35). They are medium to coarse grained size and green colored. The main observed minerals are chlorite, epidote, mica, quartz and feldspar.

The samples are strongly deformed sheared and foliated. The feldspar forms eye-shaped crystals and σ – clasts indicating mylonitic deformation.

Dryos Unit

Dryos Unit consists of low grade metamorphic rock. The rock types collected from that unit involve phyllites, greenschists (metabasites) and marbles.

Phyllite

That rock type has been collected from the southernmost part of the island and close to the contact with Marathi Unit. It is fine to very fine grained size and it contains chlorite, mica, quartz, epidote and feldspar. Eye-shaped feldspar and porphyroclasts of felsic minerals

(quartz and feldspar) are usually wrapped by brown and white mica (samples 3-5). The outcrops are highly fractured and highly deformed. A well-developed foliation can be traced within the exposure and it is, in turn, bended and folded. The outcrops in this area are highly weathered and altered, complicating the work of sampling and thin section production.

Greenschist

That lithology involves metamorphosed basic volcanic rocks (pillow lavas). They contain green amphibole and chlorite and their color is green. The pillow-shaped structures are well preserved and display rounded structures up to 1m diameter. In some cases, the meta-pillow lavas show a banded structure involving a darker color within the core (brownish) and a lighter color rim (dark green).

Marble

Marbles are found in contact with the phyllites. They are coarse grained and they show a bright white color. They are composed mainly by calcite, while mica can be observed in some cases. They are slightly deformed.

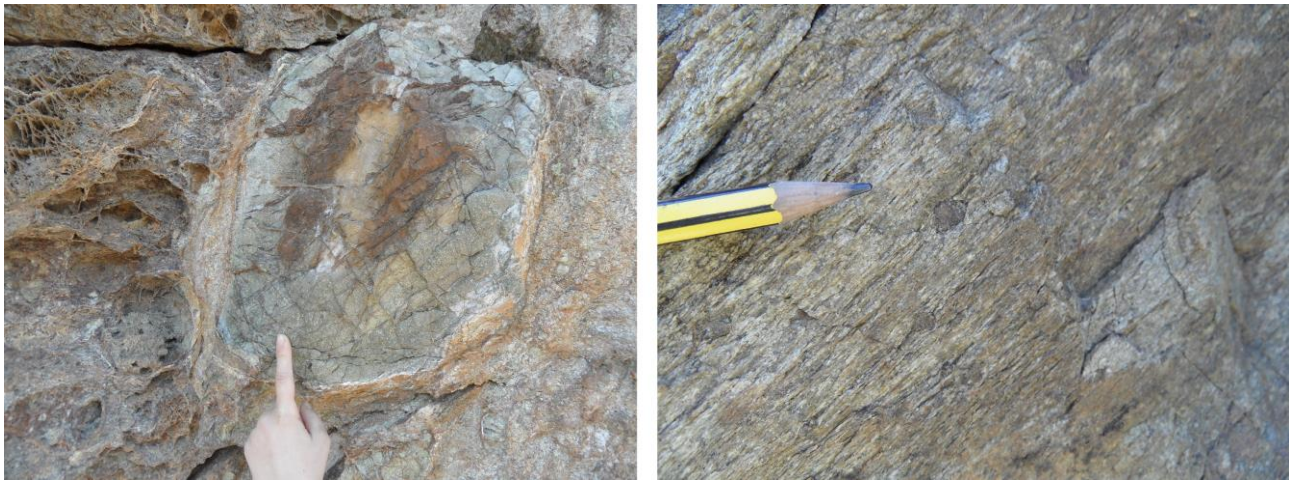

Figure 3.7: Greenschist preserving the pillow lava form. On the right garnet mica schist

3.3.2 Mineral Description

Thin section Description

P4

This rock sample has been collected from the Dryos unit and is characterized as a phyllite. It is composed of 90% fine grained ground mass and its main minerals are Chl, Ep, Bt, Qz, Feld, Cpx, Cal and Ab. The groundmass is mainly composed of an aggregate involving Chl, Ab and Cal in angular and very fine grained crystals. Porphyroclasts of Ep are broken in squared pieces and filled with an assemblage of Chl. The Cpx crystals appear with corrupted rims, surrounding by very fine grained Chl and Cal. There are also observed some lenses of deformed crystals of Qz recrystallized at their rims in finer grained crystals. Moreover Cpx appears as fine grained deformed and angular crystals.

No indication found in that thin section about the relation between Cpx and Ep. According to the crystal size composing the groundmass the sample can be characterized as a mylonite.

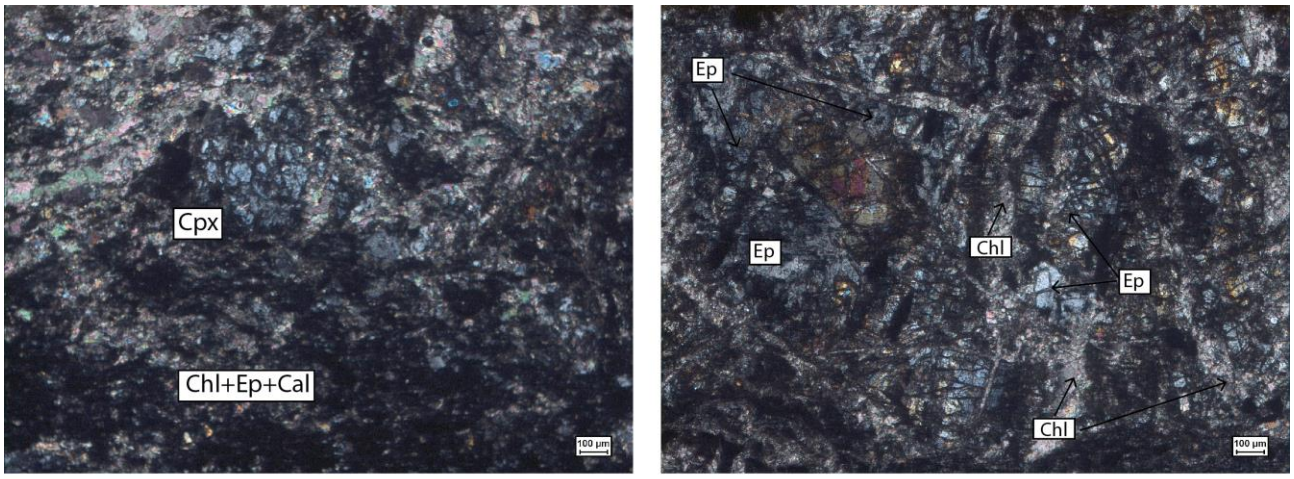

Figure 3.8: Microscope image showing broken crystal of Cpx surrounded by a matrix of Chl, Ep and Cal. B). Broken crystal of Ep filled with Chl.

Mineral	D1	D2	D3
Calcite		x	
Feldspar		x	
Epidote	x	x	
Opaque		x	
Clinopyroxene	X		
Chlorite		x	

P5

This rock sampled has been collected from Dryos unit and it is characterized as a phyllite. The main minerals composing that sample are Bt, Ms, Qz, while St, Chl and Ep can be observed as secondary minerals. All the crystals are deformed, displaying undulose extinction without any sign of re-crystallization. The sample is strongly foliated and banded. The foliation is defined by coarse grained and elongated Ms and Bt. The bands are composed by medium grained quartz and coarse grained elongated white mica (Ms). Two generations of quartz can be observed; coarse and finer grained. Coarse grained Qz forms anastomosing pockets together with Ms wrapped by fine grained Bt. Fine grained aggregates form bands and veins. Observed crystals of medium grained St are with corrupted rims are randomly oriented. The sample contains less than 50% of matrix (around 20%), classified as a protomylonite.

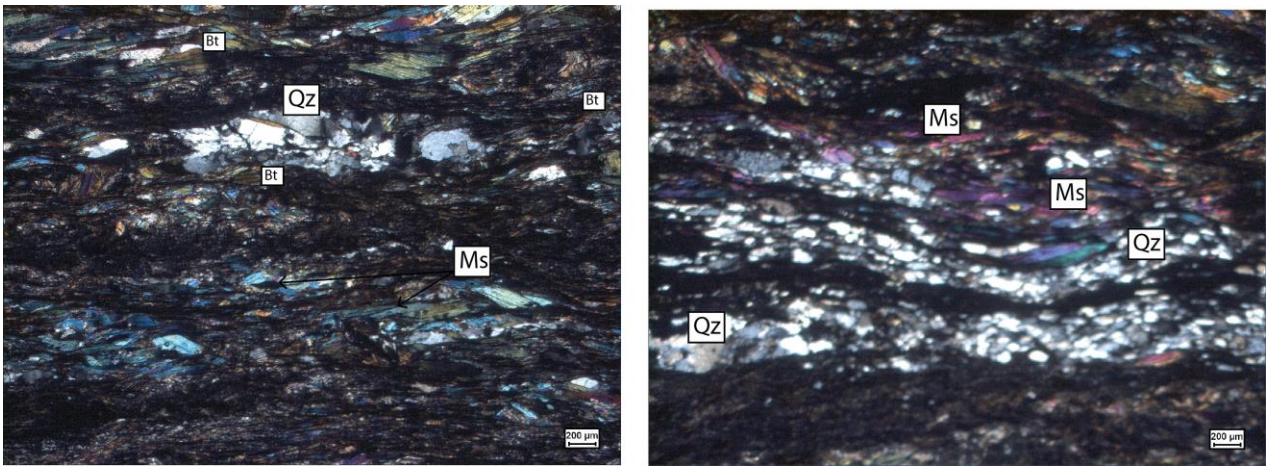

Figure 3.9: Optical microscope images (XPL) displaying alterning domains richer in Qz and Bt.

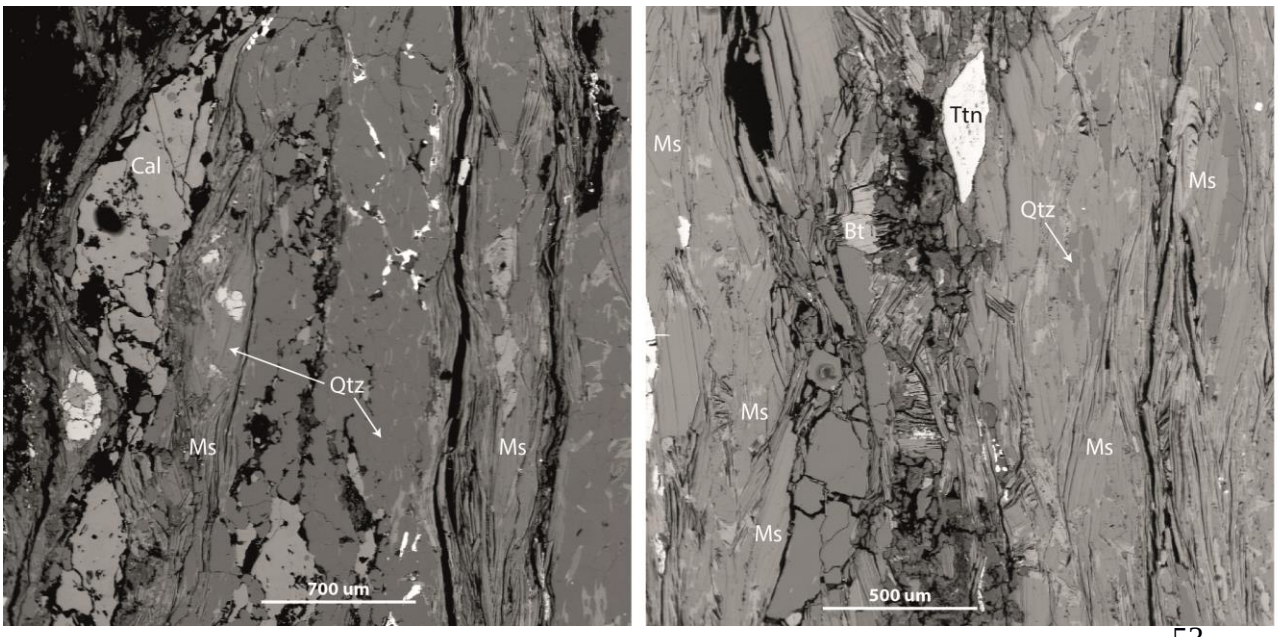

Figure 3.10: EMP images illustrating the presence of calcite (left) and titanite within the main foliation.

Mineral	D1	D2	D3
Feldspar		x	
Biotite		x	
Opaque			
Muscovite		x	
Quartz		x	

P21

This rock sample has been gathered from Marathi Unit and is characterized as an amphibolite. Its main minerals are Amp (around 70%) and Pl (around 25%), while Cpx can be observed as well. A well-developed foliation is defined by coarse grained and elongated Amp. Pl is coarse grained and well-shaped forming clear alternating bands with the Amp. Crystals of Cpx appear randomly oriented containing oriented inclusions of Amp. They display poor rims, while occasionally they display reaction rims with the Amp and the Pl.

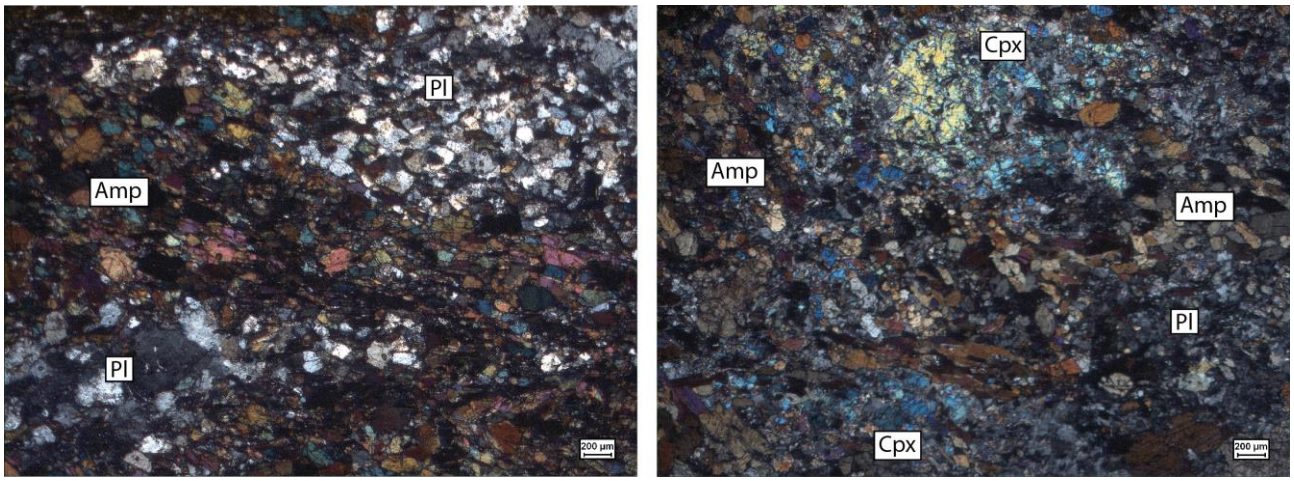

Figure 3.11: Optical microscope images (XPL) displaying Amp-Pl rich domain (left) and the localized appearance of Cpx.

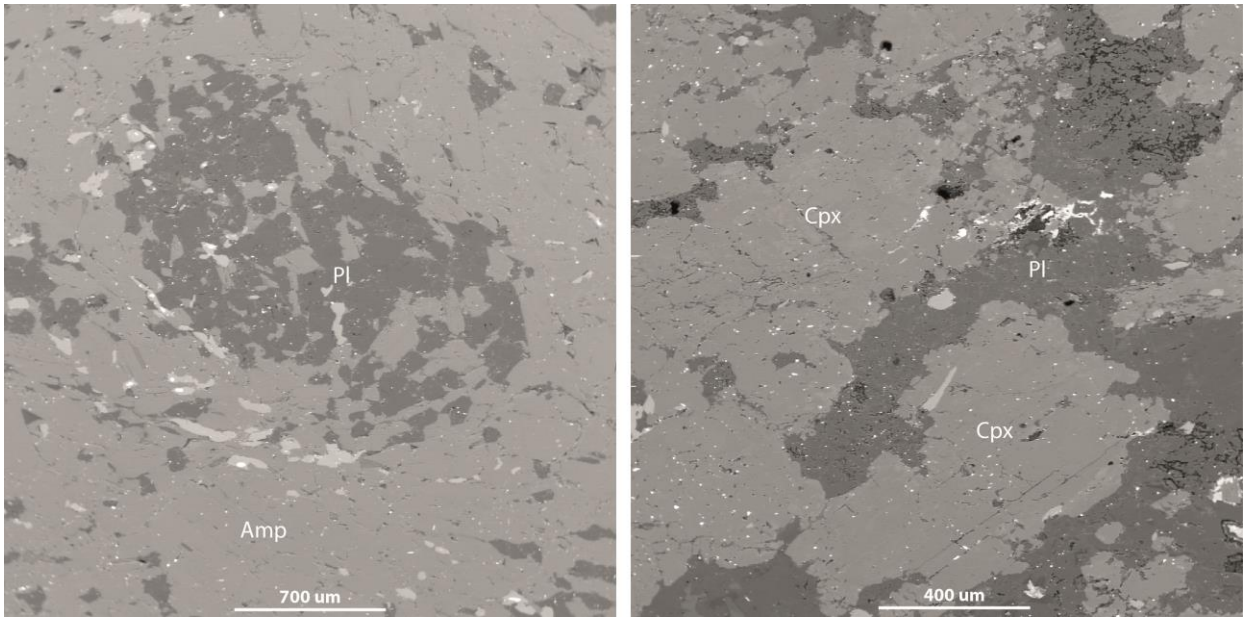

Figure 3.12: EMP images illustrating relationships between Amp and Pl (left) and Cpx and Pl (right).

Mineral	D1	D2	D3
Plagioclase	??	x	
Epidote		x	
Green amphibole (Hornblende)		x	
Opaque		x	
Pyroxene	x		

P22

This rock sample has been gathered from the NE section of the Marathi Unit and it can be characterized as an amphibolite. It contains Grt, Fsp, Pl, Qz, Amp, Cpx and Scp as main minerals and Mag, Ep, Cal, Chl and Bt as secondary and it is deformed and foliated. The foliation is defined by elongated Amp and Pl in alternating bands, while big porphyroblasts of Grt appear deformed and broken. The crystals of Grt are surrounded by green Amp, while its fractures are filled with a fine aggregate. Qz displays a preferential orientation and undoluse extinction. Cpx crystals are coarse grained with euhedral rims. Locally, they show reaction rims defined by Pl crystals. Coarse grained Cpx crystals are wrapped by Qz. The Amp is slightly oriented and euhedral.

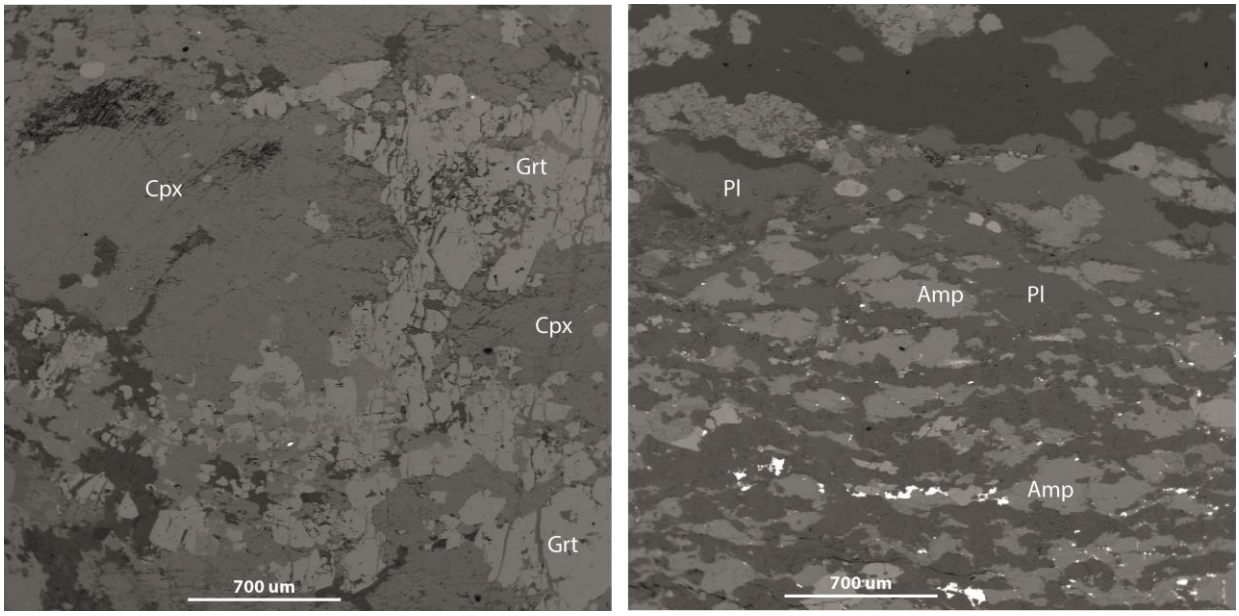

Figure 3.12: EMP images of Cpx-Grt rich domain (left) and Amp-Pl domain (right).

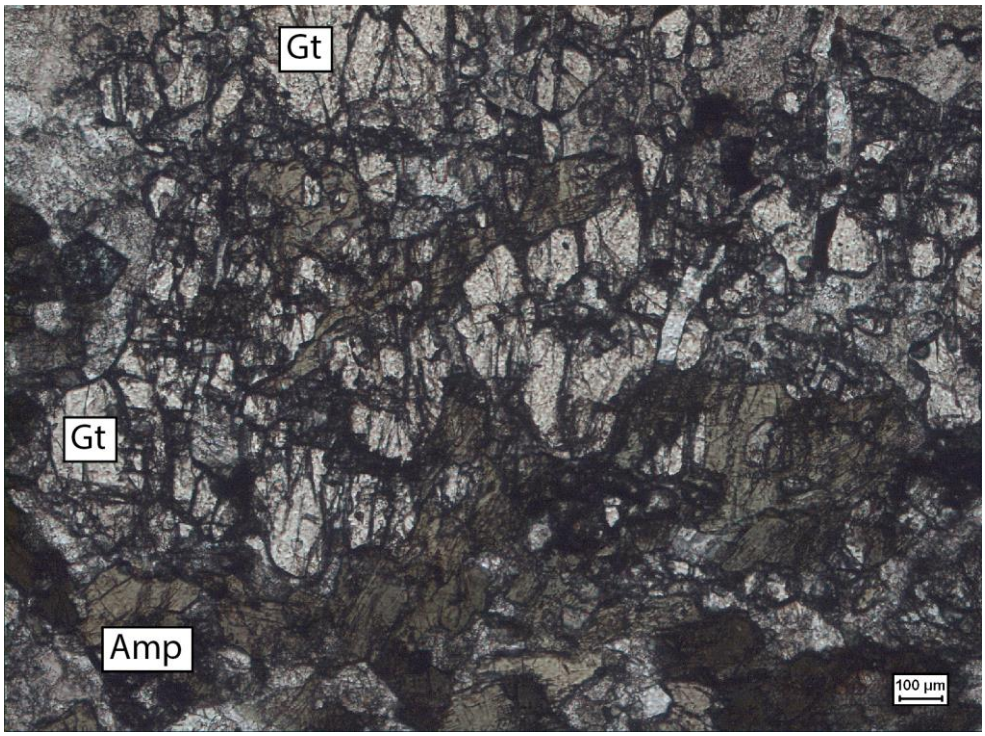

Figure 3.13: Optical microscope image (PPL) displaying mutual relationships between Amphibole (Amp) and Garnet (Grt).

Mineral	D1	D2	D3
Calcite	x	x	
K Feldspar	x		
Plagioclase		x	
Epidote	x		
Sphene	x		
Chlorite		x	
Green amphibole (Hornblende)		x	
Garnet	X		
Clinopyroxene	x		
Quartz	x	x	

P24

This rock sample can be characterized as an intermediate rock, with characteristics of both amphibolite and granulite facies. It contains Grt, Feld, Pl, Qz, Amp, Cpx and Scp as main minerals and Cal, Chl, Bt and Ttn as secondary. No clear foliation can be observed since the thin section is dominated by Grt, Cpx and Amp with no clear preferential orientation. Grt crystals are generally broken and filled with Feld (Fig.3.14 and 3.15) and have relatively sharp boundaries with large, corroded Cpx. Amp is minor and always in contact with Grt. The rest of the matrix is formed by Qz, Scp, Chl and Bt. Qz displays a preferential orientation and undulose extinction.

An assemblage of Amp + Pl is being replaced by a more stable assemblage formed by Grt + Pl + Cpx + Scp.

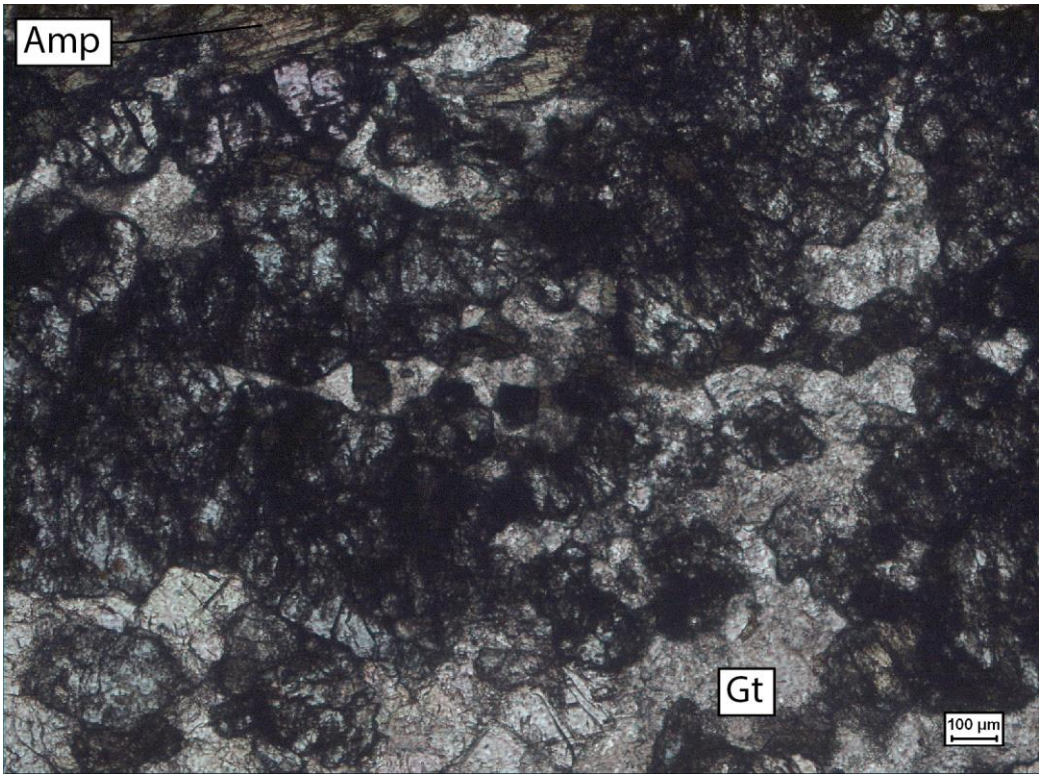

Figure 3.14: Optical microscope image (PPL) displaying mutual relationships between Amphibole (Amp) and Garnet (Grt) (sample P24).

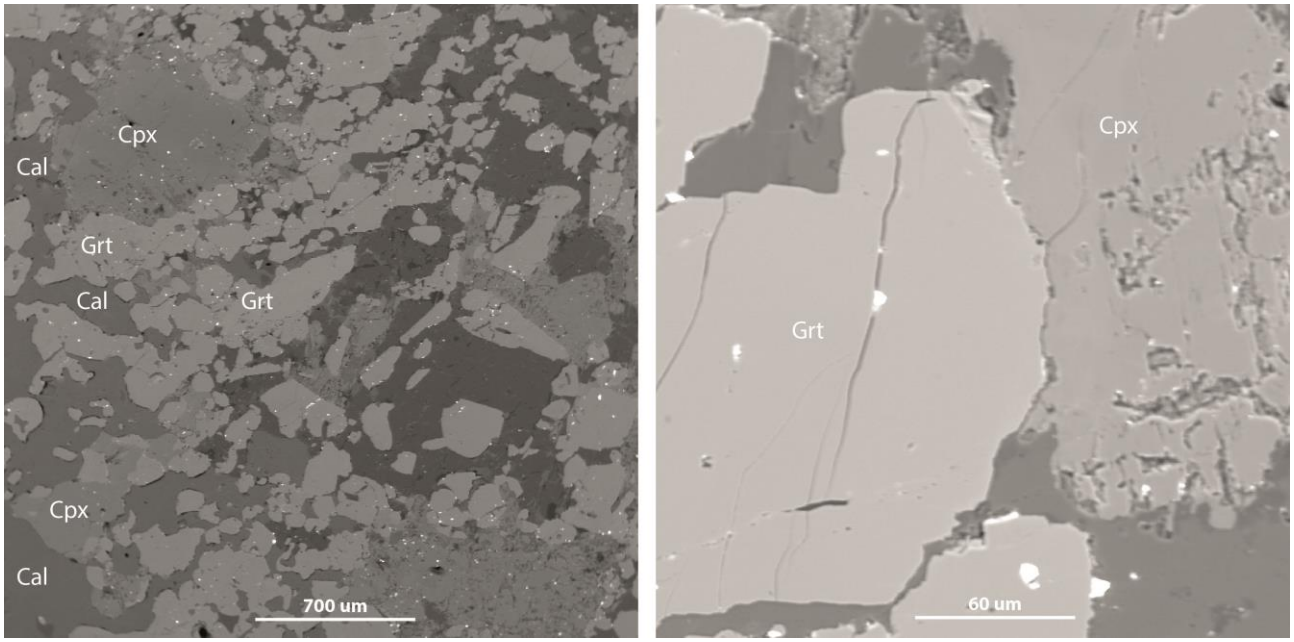

Figure 3.15: EMP images showing texture of sample P24 formed by Cpx-Grt and Cal (left). On the right, Grt and Cpx are in clear textural equilibrium (sample P24).

Mineral	D1	D2	D3
Calcite		x	x
Feldspar	x	x	
Epidote			x
Green amphibole (Hornblende)	x		
Scapolite		x	x
Garnet		x	
Biotite			x
Chlorite			x
Pyroxene		x	

P32

This rock sample can be defined as a mafic granulite. It contains Grt, Pl, Qz, Amp, Cpx and Scp as main minerals and Cal, Ep and Ttn as secondary. No clear foliation can be observed since the thin section is dominated by large porphyroblasts of Grt surrounded by very large crystals of Scp that makes up to 60% of the rock. The Grt are often broken and contain multiple minerals inclusion of Pl, Cal and Ep but not Scp. Amp is minor and generally occurs only at the margins of large Grt (Fig. 3.16) or in association with Cpx (Cpx clearly formed inplace of Amp)

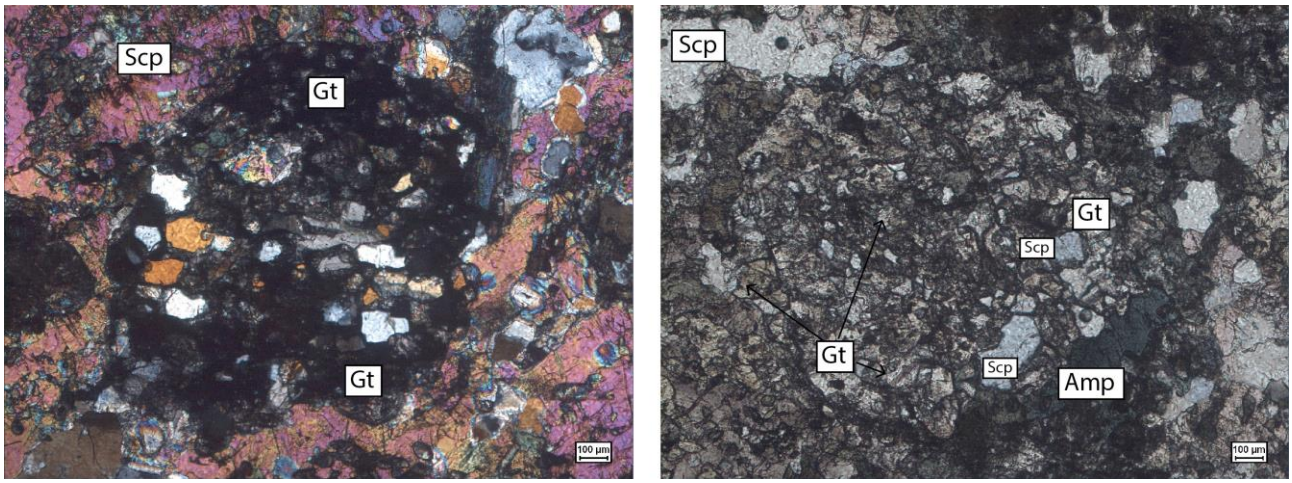

Figure 3.16: Optical microscope images (XPL and PPL) showing large Grt surrounded by a high birefringence Scp.

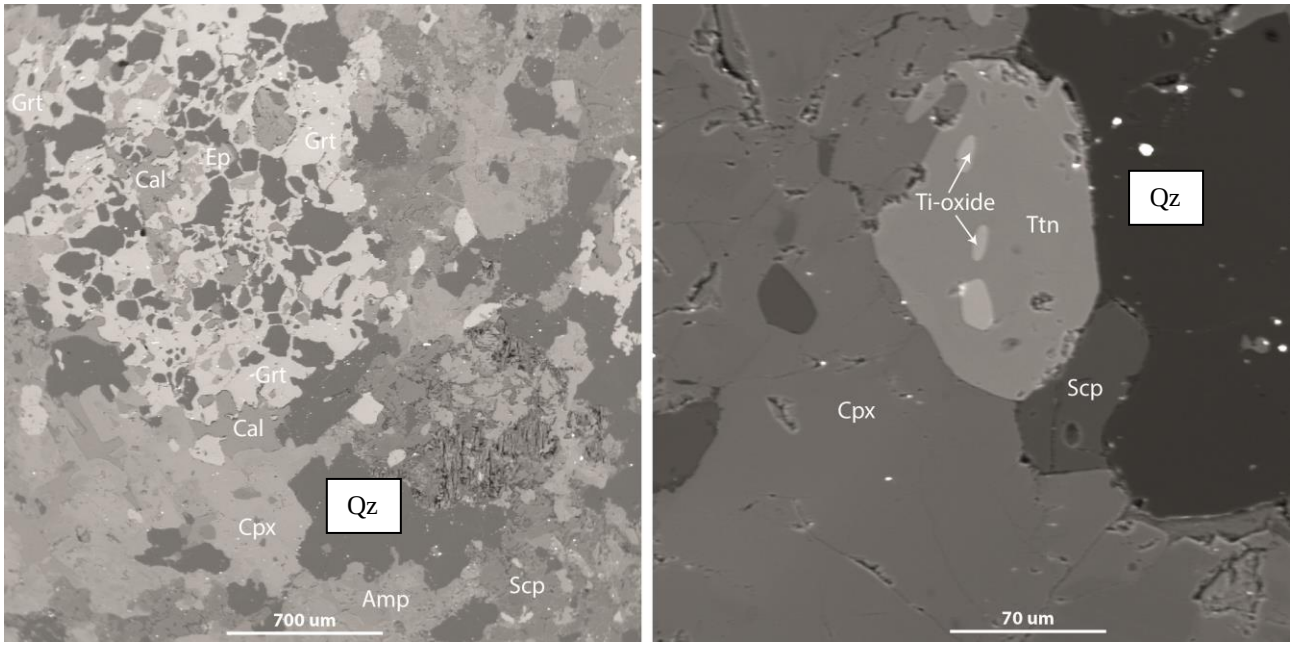

Figure 3.17: EMP image showing Grt (lighter color) containing crystals of Ep, Cal and Qz whereas Scp is present only outside the Grt (left). Cpx in chemical equilibrium with Qz, Ttn and Qz (right).

Mineral	D1	D2	D3
Scapolite		x	
Feldspar	x		
Green amphibole (Horneblende)	x		
Biotite			x
Clinopyroxene		x	
quartz	x	x	
garnet		x	

3.4 Mineral chemistry

3.4.1 EMP analyses

Electron Microprobe (EMP) analyses were performed using a JEOL JXA-1800 Superprobe equipped with an energy dispersive detection system and five wavelength dispersive spectrometers (WDS) at Utrecht University. Carbon coated thin sections were initially analyzed with Energy Dispersive Spectrometry (EDS) for quick identification of minerals and Wavelength Dispersal Spectrometry (WDS) for high resolution mineral chemical analyses

3.4.2 Results

Marathi Unit

Garnet

Garnet composition on the mafic lithologies of Marathi Unit is fairly uniform with local differences depending on the bulk rock composition. Sample P22 is defined by 35% Grossular, 35% Almandine + Andradite and 30% Pyrope + Spessartine whereas sample P24 Grt is slightly different with 35% Grossular, 50% Almandine + Andradite and 15% Pyrope + Spessartine. Instead sample P32 has two populations of Grt, one with 20% Grossular, 40% Almandine + Andradite and 40% Pyrope + Spessartine and the other with 20% Grossular, 60% Almandine + Andradite and 20% Pyrope + Spessartine

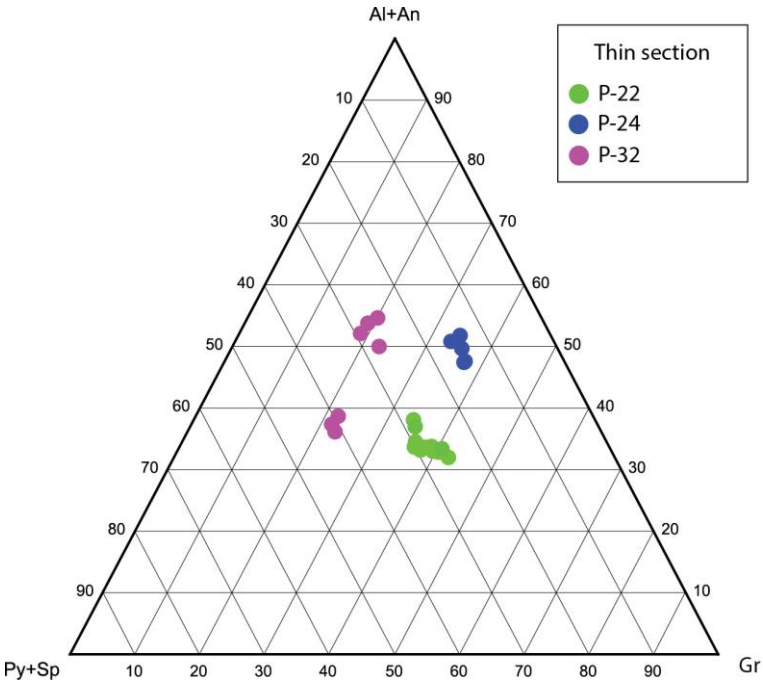

Figure 3.18: Garnet TRIPLOT based on end-member composition. Al: Almandine, An: Andradite, Gr: Grossular, Py: Pyrope and Sp: Spessartine. Color indicates the thin section.

Diopside

Clinopyroxene have very constant compositions with CaO of 22-24%, 8-10% FeO and 8-11% MgO. Only clinopyroxenes in sample P24 show a different chemical composition, with a marked FeO enrichment up to 15%. Based on their FeO and MgO content, all clinopyroxene are Diopside.

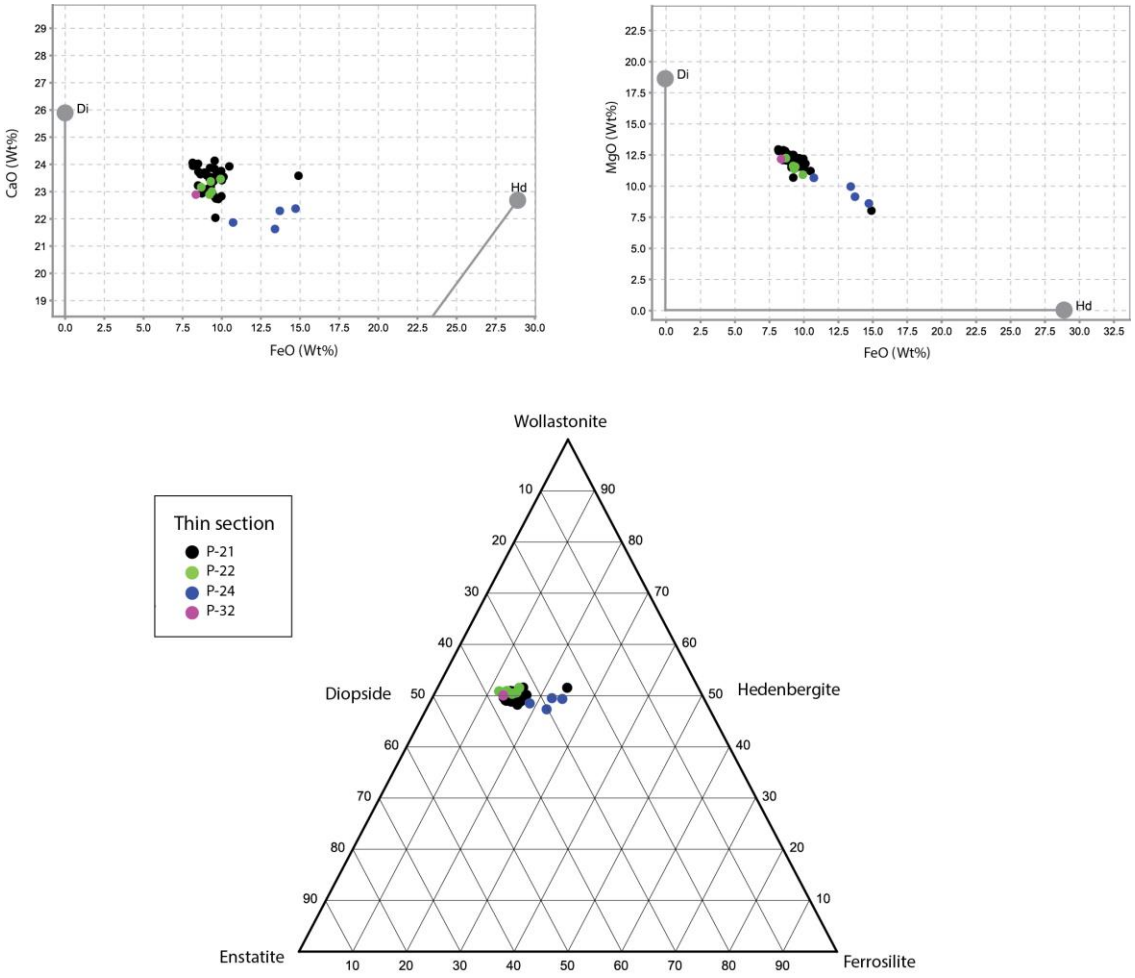

Figure 3.19: CaO vs FeO, MgO vs FeO diagrams and PYROXENE TRIPLOT plotted along with mean composition (Grey dot) of Hedenbergite (Hd) and Diopside (Di). Color indicates the thin section.

Amphibole

Amphibole is variable and strongly depends on the analyzed thin section. Sample is defined by an amphibole population with 11.5% CaO and 39.5-42% SiO_2 (Fig.3.20) that is very close in composition with Pargasite. Instead, a second population is defined by higher SiO2 (47-52%) and CaO (12-12.5%) and therefore they were classified as Mg-Hbl (SiO_2>50%) and Actinolites (SiO_2<50%).

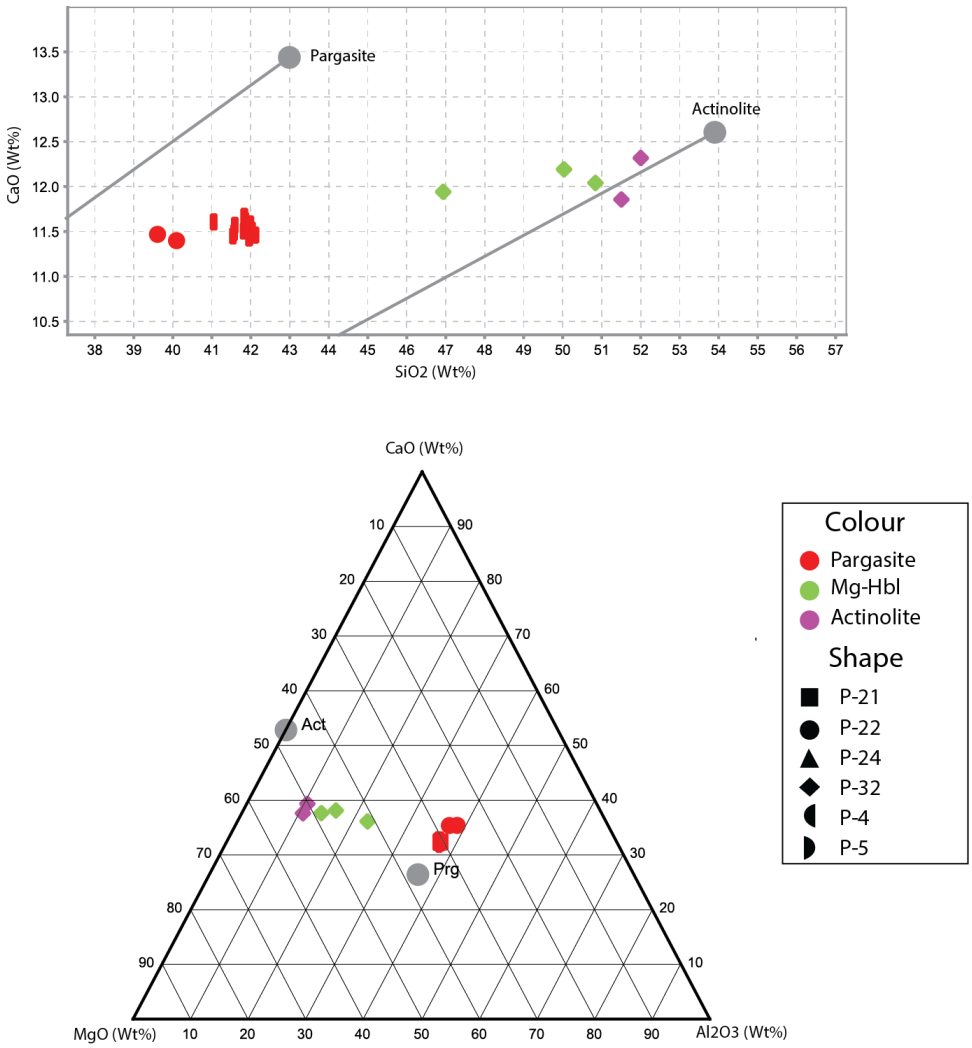

Figure 3.20: CaO vs SiO_2 diagram and CaO,MgO and Al2O3 TRIPLOT plotted along with mean composition (Grey dot) of Actinolite (Act) and Pargasite (Prg). Color indicates the type of mineral and the shape the thin section.

Feldspar

Plagioclase in the mafic rocks of Marathi Unit range in composition between Andesine, Labradorite and Bitownnite for samples P21-P22-P24-P24 (Fig.3.21). Instead sample P4, which belongs to Dryos Unit, is characterized by a strong depletion in CaO, resulting in a NaO-rich plagioclase termed as Albite.

Titanite and Clinozoisite

Titanite have a constant chemical composition with 27.5% CaO, 28.5-30.5% SiO_2 and Al_2O_3 < 2% (Fig.3.21). Clinozoisite instead is defined by 22.5% CaO, 36-38% SiO2 and Al_2O_3 of 25% (Fig.3.21).

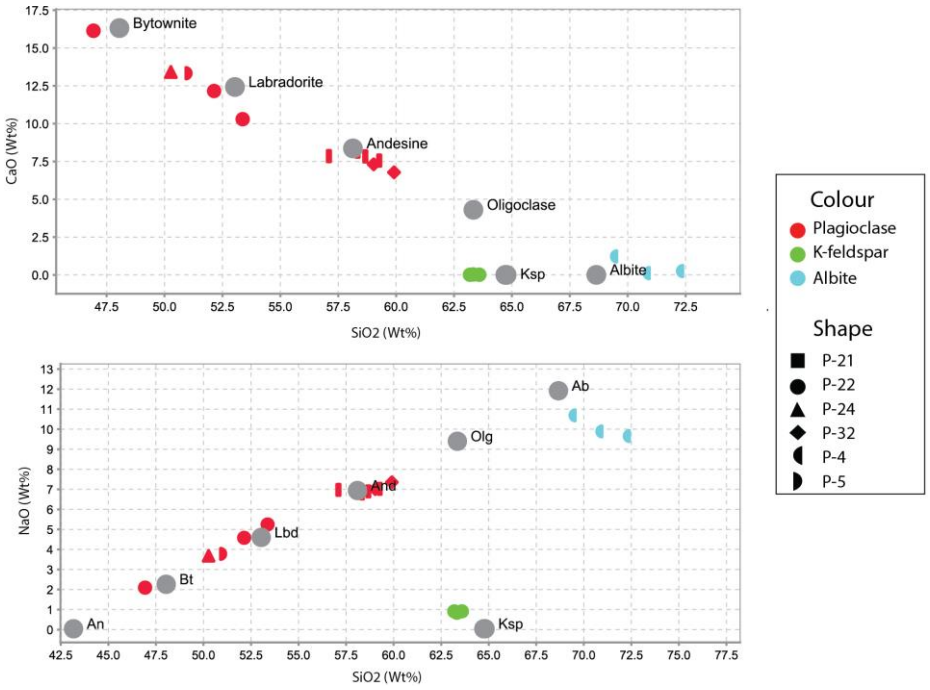

Figure 3.21: CaO vs SiO_2 and NaO vs SiO_2 diagrams plotted along with mean composition of K-feldspar, Albite, Oligoclase,

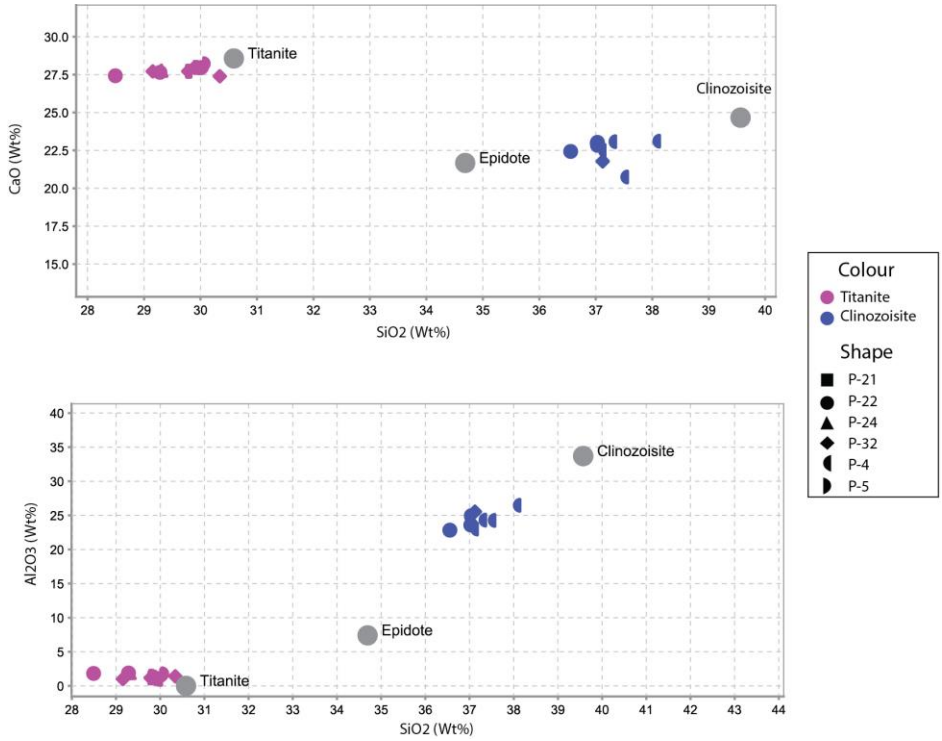

Figure 3.22: CaO vs SiO2 and Al_2SiO_3 vs SiO_2 diagrams plotted along with mean composition of Clinozoisite, Epidote and Titanite (Grey dot). Colour indicates the type of mineral and the shape the thin section.

Andesine, Labradorite and Bitownnite (Grey dot). Color = type of mineral, shape = thin section.

3.5 Geothermobarometry

Marathi Unit

Mafic rocks are the most suitable for the application of classic geothermobarmetry but mostly in granulite and eclogite facies. In greenschist or amphibolite facies, reliable geothermometers are lacking because of the presence of fluids. In fact, water activity in mineral like amphibole deeply influence the PT estimates and, therefore, they should be used with caution. The only sample with an appropriate mineral assemblage is P21 because the presence of amphibole and plagioclase (minor clinopyroxene) allows the application of two thermobarometer (see below).

However, sample P21-P24-P32 are transitional between amphibolite and granulite facies due to the coeval presence of amphibole, plagioclase, garnet and clinopyroxene. Such assemblage cannot be associated to precise PT estimates. We tried to apply Grt-Cpx Fe^{2+}/Mg exchange thermometer (Ravna, 2000) but the result are meaningless, implying out of equilibrium reactions or ionic exchange with other minerals (i.e. amphibole).

Nevertheless, we can infer higher equilibration temperature with respect P21 because of the presence of garnet and clinopyroxene, a set of mineral characteristic in the granulitic facies.

P21

The Amphibole-Plagioclase thermometer of Holland and Blundy (1994) is applied to sample P21 and yield the following results for different pressure (arbitrary input):

Results (mean values):

T = 708 ±20 C at 2 Kbar T = 718 ±20 C at 4 Kbar

T = 739 ±20 C at 8 Kbar T = 749 ±20 C at 10 Kbar

These results are partly corroborated by semi quantitative P–T estimates of 10± 1 Kbar and 790 ± 30 °C based on the TiO2 and Al2O3 contents of calcic amphiboles in presence of plagioclase (Ernst and Liu, 1998).

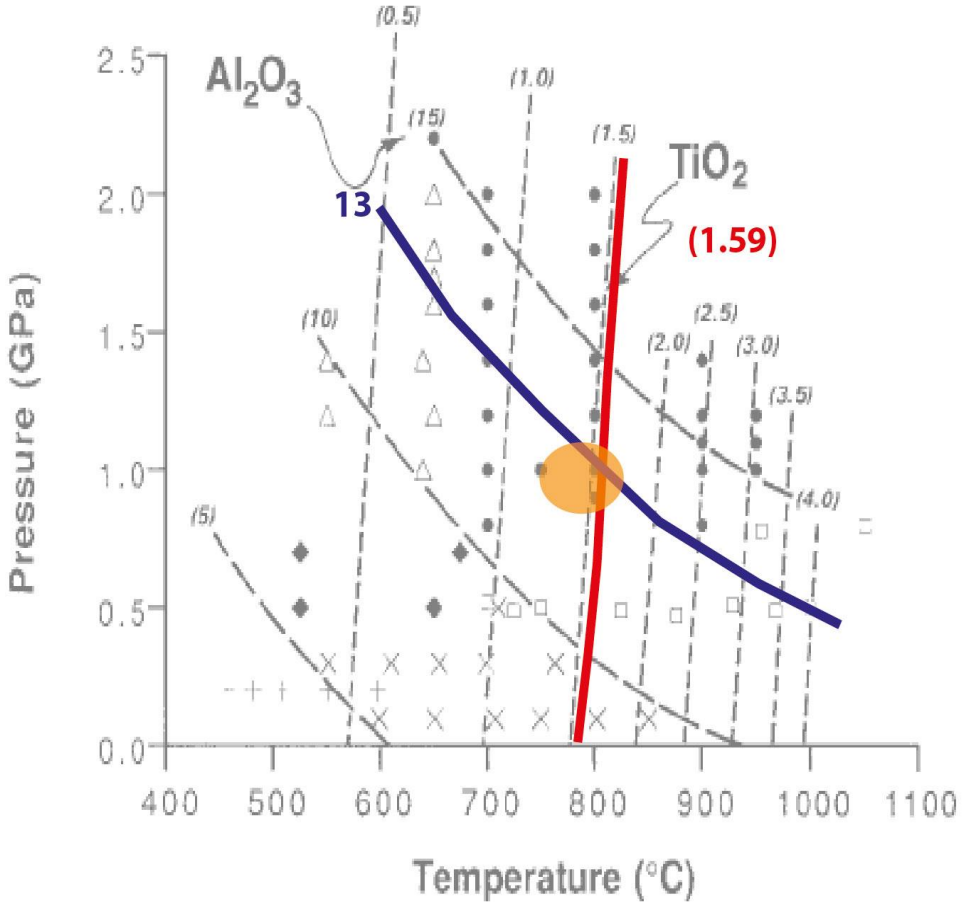

Figure 3.23: Graphic illustration based on the work of Ernst and Liu (1998) for sample P21. Al_2O_3 (wt%) and TiO_2 (wt%) content of amphibole define a PT conditions (orange oval) of 790 ± 30 °C and 10± 1 Kbar (1± 0.1 Gpa).

3.6 Discussion

3.6.1 Marathi Unit

The outer Cycladic Islands are affected by an HP metamorphic event reported in many localities by findings of rocks with phengite, glaucophane and jadeite mineral paragenesis (Robert, 1982). Although this metamorphic event is not reported in the Island of Paros, blueschist metamorphic conditions (**M1**) can be inferred by correlative units of Naxos island where the HP event is dated at 45+-5Ma (Andriessen et al., 1979) under 12 Kbar pressure and at 470° C temperature (Avigad, 1998; Jansen, 1977). In other islands, this HP event reached a metamorphic peak of 550 °C (Avigad et al., 1998; Brockers and Enders, 2001).

The **M2** phase is characterized by a fist decompression event in amphibolite and greenschists facies as recorded by mafic rocks comprising Marathi Unit. HP mineral paragenesis re-equilibrated in amphibolite to greenschist facies. Samples analyzed in

chapter 3.3 show that amphibolites (samples P21-P22-P24-P32) are not stable because of the contemporaneous presence of plagioclase, hornblende, garnet and clinopyroxene. While pyroxene and garnet are typical minerals in granulite facies, plagioclase and hornblende characterize amphibolite facies and they should not be stable at the same time.

We interpret the coeval stability of these minerals as an effect of the temperature increase due to **M3** heating event related to formation of the dome. Amphibolites are metastable and they represent a narrow temporal window in which mineral in amphibolite and granulitic facies can coexist. Amphibole-plagioclase geothermobarometry indicates thermal re-equilibration at 10± 1 Kbar and 790 ± 30 °C. These calculated PT conditions broadly coincide with amphibolite-granulite transition for an average basic rock (Fig. 3.24).

Greenschist conditions prevail in the southern part of the island. Following the work of Robert (1982), these rocks re-equilibrated during M2 and were not affected by M3 HT overprint as in the northern part of the island.

3.6.2 Dryos Unit

Dryos Unit comprises low to medium grade metamorphic rock which retain primary structures. Figure 3.7 shows a meta-basalt with well-preserved pillow lavas in the process to re-equilibrate in greenschist facies from rim to core. Only a low strain deformation up to the greenschist facies could preserve such structures. Other samples collected from the Dryos Unit are characterized by mineral assemblages typical of the greenschist facies as Ms-Bt-Chl-Ep in sample P5 and broken epidote surrounded by a matrix of Chl-Ab-Cal in sample P4.

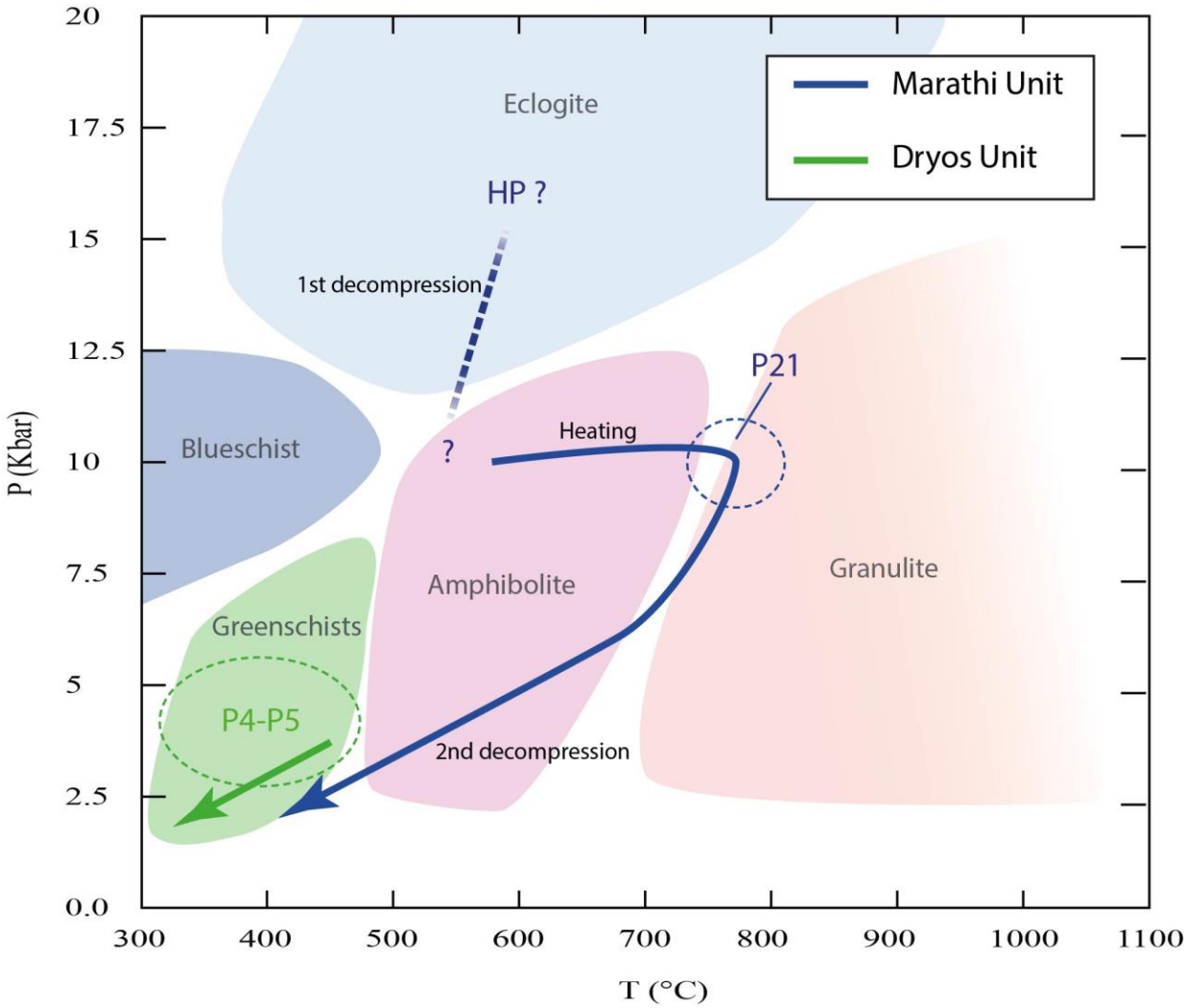

Figure 3.24: Pressure -Temperature diagram comprising metamorphic facies for a general basic rock. PT path for Marathi ad Dryos are based on a collection of personal and literature information (see Chapter 3.3)

The tectono-metamorphic evolution of the Dryos unit is in principle enigmatic because of lacking of suitable mineral assemblages for geothermobarometry and unclear mineral relationships. For instance the origin of the clinopyroxene in Fig.3.11 is not clear and requires more investigations to be confirmed and interpreted. Further work is required for a full interpretation of the Dryos Unit but I provided evidences that this unit did not reach a metamorphic grade higher than greenschist (Fig.3.24).

3.7 Conclusion

Are Marathi and Dryos the same unit?

Interpreting the Marathi and Dryos Unit has been a controversial issue since the 80'. Robert (1980) ascribed metamorphic differences to progressive temperature decrease further away from the dome outcropping in the center of Paros. Conversely, the work of Papanikolaou (1980) suggests that Mahrati and Dryos are separated by a detachment bringing in contacts units with different metamorphic conditions.

This study provides evidence that the Marathi and Dryos Unit do not share the same metamorphic evolution and are not part of the same tectono-lithological unit. Primary structure preservation up to greenschist facies in the Dryos Unit indicates low strain deformation at low pressure and temperature. These structures should be disrupted in a pervasive HP event followed by a strong thermal overprint during M2 and M3 as with the Marathi Unit.

As a result, these units came in contact during a 2nd exhumation cycle of the Marathi Unit (Fig.3.24) in greenschist facies or lower conditions conditions, as indicated also by the cataclastic fault rock along the contact.

3.8 Future works

- Production of a map outlining temperature isograds following the example of Robert (1982) but with the use of modern geothermobarometry (more samples are necessary);
- Investigation on the PT conditions reached by the NW part of Paros and compare them with the metamorphic evolution in the SE. Even though these two areas belong to the same tectono-metamorphic unit (i.e. Marathi Unit), they are separated by the Mid Cycladic Lineament and therefore they might have slightly different PT path during exhumation,
- This thesis shows that Marathi and Dryos are two distinct tectono-metamorphic unit with different peak assemblages but more investigations are required to precisely estimate the PT conditions reached by Dryos. In addition, the nature of the contact is still enigmatic and it should be investigated in detail,
- Dating the peak metamorphism might add invaluable constraint on the complex tectono-metamorphic evolution of the island of Paros and of the Central Cyclades during post-orogenic exhumation.

PART 4: DISCUSSION

4.1 What structure accommodates the rotation?

According to the measured paleomagnetic declination values we conclude that a 100° rotation difference between the northwestern and the southeastern part of Paros occurred. Petrofabric analyses on the magnetic mineral preferred orientations in comparison with the orientation of the stretching lineations of the Miocene granites, suggest that the rotation of those rocks occurred after their intrusion between 12 and 17 Ma. Thermomagnetic measurements show that the rotation occurred below temperatures of 350° and 500°C after granites cooled down. This range of temperatures is typical of the greenschist facies.

Based on the above-mentioned findings, the structure supporting the rotation on Paros operated in the upper crustal levels between 13 and 18 km, at the ductile to brittle transition. Additionally in order to meet the kinematic requirements the structure supporting vertical axis rotation demands a low angle detachment fault. In the island of Paros three major detachment faults are mapped: the Central Cycladic Detachment Fault, the contact between Dryos and Marathi Unit and the NW detachment fault which coincides with the NW contact between the high grade metamorphic rocks of Marathi Unit and the Pre-Alpine orthogneisses.

The Central Cycladic Detachment fault is a top-to-the north detachment fault and brings in contact the metamorphic units of Marathi and Dryos Unit with the non-metamorphic formations represented by the Marmara Unit. Because the stretching lineations are recorded only in the metamorphic formations of the Cyclades, this structure is excluded from further investigations.

The contact between the Dryos and Marathi Unit separates high grade metamorphic rocks from low grade metamorphic rocks. Our petrological study, performed on rock samples of both Units close to their contacts, reveals that this structure functioned in upper crustal levels under greenschists facies conditions. Geothermometry on these units shows different peak metamorphic conditions implying a metamorphic gap between these two units (Chapter 3.7). Therefore, it might have accommodated the vertical axis rotation between the two opposite rotating blocks in Paros as indicated by the paleomagnetic study in chapter 2.4.4.

Although, in our interpretation this fault cannot represent the border between two opposite rotating domains because the Dryos Unit outcrops exposes both NE and N-S trending stretching lineations. These two domains are exposed NW and SE of Paros, respectively (Fig.1.8; Gautier, 1993). As a result the MCL is a major tectonic detachment which cross-cut and rotated also the rocks belonging to the Dryos Unit.

Paleomagnetic, structural and petrological data suggest that the only structure supporting the vertical axis rotation on Paros is the south dipping low angle detachment fault which coincides

with the tectonic contact between the metamorphic rocks of Marathi Unit and the Pre-Alpine basement in the NW part of the island (Fig.4.1). The strain on this detachment fault was preferentially partitioned along the gneiss-marbles boundary forming mylonites and ultramylonites (Papanikolaou 1980; Gautier et al., 1993). Ductile fabrics between the metamorphic lithologies of Marathi unit and the Pre-Alpine basement are parallel or sub-parallel, and occasionally low angle ductile shear zones cross-cut the contact (Kostis, unpublished). Locally, low angle normal faults overprint previous ductile structures. In fact it is reported the presence of tectonic breccias and cataclasites composed of the overlain rocks (Papanikolaou 1980; Gautier et al., 1993., Lister et al., 1999).

In conclusion, this SE dipping detachment fault initiated at depth in the ductile regime and evolved up to shallower brittle conditions in a progressive movement, accommodated the vertical axis rotations that took place on Paros after 12-17 Ma, as it is supported by the paleomagnetic study.

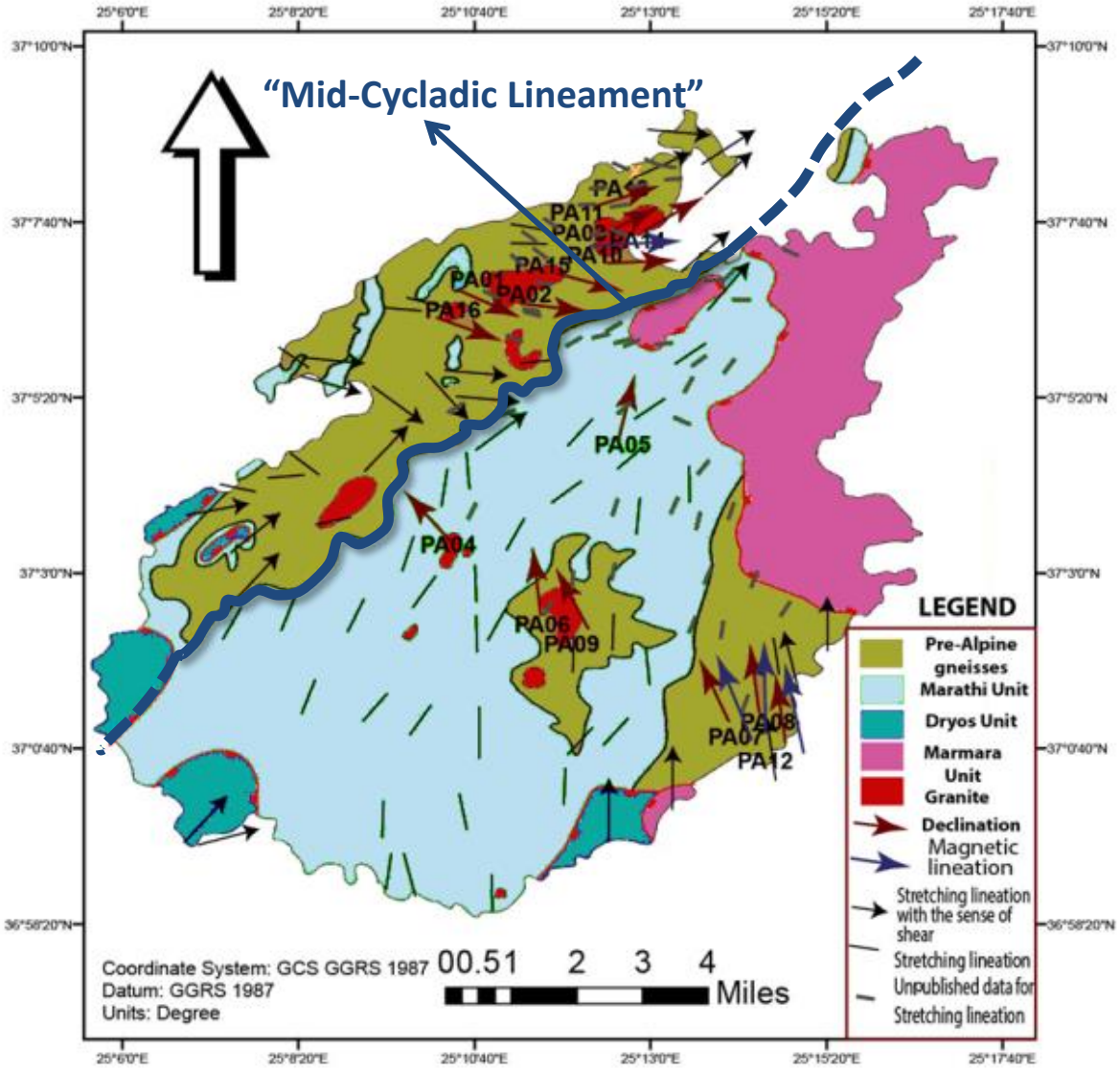

Figure: 4.1: Geological map of Paros presenting the stretching lineation, the magnetic lineations, the paleomagnetic declination and the structure separates the two domains. . The blue line represents the "Mid-Cycladic Lineament"

4.2 What is the " Mid Cycladic Lineament"(MCL)

The notable sharp change in the orientations of the stretching lineations on Paros coincides with the SE dipping detachment fault in the northwestern part of the island. This structure was primarily recognized as an early generation detachment fault, responsible for the progressive exhumation of the Central Cyclades in metamorphic core complexes (Lister and Davis 1989; Lister et al., 1996; Lister et al., 1999). Instead, Walcott and White (1998) interpreted the above mentioned structure as the boundary between two opposite rotating tectonic blocks defined by different orientation of the stretching lineation: the Western Aegean Block and the Eastern Aegean Block. In their study, this structure named “Mid-Cycladic Lineament” (MCL) is inferred as a former dislocation zone which functioned as a shear zone during the post-orogenic extension to accommodate the vertical axis rotation of the opposite rotating blocks.

This study provides additional information on the nature of the “MCL”, contributing to a better understanding on the role it played during post-orogenic extension on the island of Paros. In essence, we consider the “MCL” as a detachment fault supporting the coeval exhumation and rotation of the northwestern part of the island beneath the southeastern part of the Paros. It is important to note that from this point we define the SE part bounded from the “MCL” to the Central Cycladic detachment fault.

.

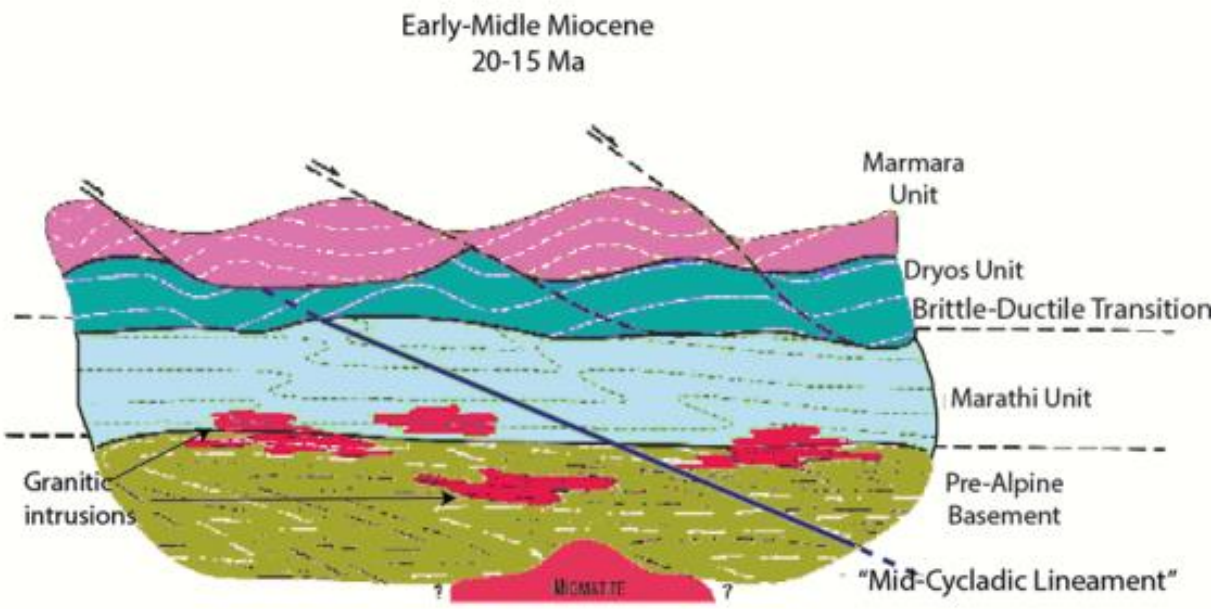

Figure 4.2 : 2D cross section of Paros showing the 2 domains separating from the “MCL“ (modified after Kostis, unpublished)

The “MCL” separates two domains characterized by different orientations of the stretching lineations; the northwestern part showing NE trending stretching lineations and the southeastern part delineated by north-south dipping lineations. Both domains belong to the same tectono-

metamorphic unit: the Cycladic Blueschists Unit (CBU), which in Paros is defined by a pre-Alpine basement overlain by Alpine metamorphic formations (i.e.Marathi Unit) (Fig.4.2). The structural configuration of the MCL shows that the NW domain is the footwall while the SE part represents the hanginwall of the fault. Further paleomagnetic data obtained in chapter 2.3 reveal that the NW domain underwent clockwise rotation of 100°, opposed to the 10° anticlockwise rotation recorded for the SE part. By restoring the kinematic evolution of both domains we conclude that their rotation was generated from an N-S original orientation. The metamorphosed footwall, corresponding to the Cycladic Blueschist Unit and involving the metasedimentary cover together with pre-Alpine basement, was divided in two parts along the "MCL". The lower geologic part underwent a major clockwise rotation all along its exhumation underneath the upper part of the footwall. Simultaneously, the upper part was exhuming underneath the non-metamorphic hanging-wall which is represented on Paros by Marmara Unit and rotated only in a minor counter clock wise direction (Fig.4.3).

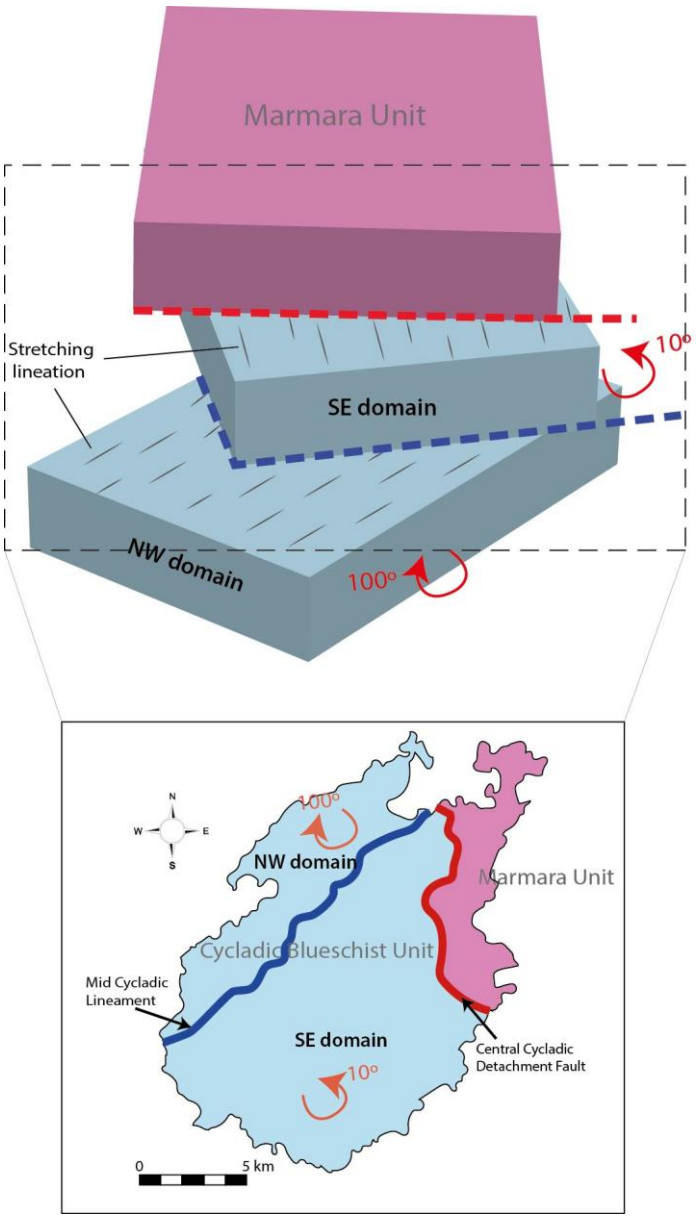

Figure 4.3: 3D illustration of the block kinematic, showing the NW CBU domain rotated and exhumed along the "MCL" (blue line) and the SE CBU domain rotated and exhumed along the Cycladic Detatchment fault (red line).

4.3 What are the regional implications of the "MCL" for the Central Greece?

The Aegean region lies upon the Hellenic orogenic Belt which comprises a previously stacked nappe pile, reworked and exhumed in extensional metamorphic complexes during late orogenic extension (Ring et al., 2007; Jolivet et al., 2010; Philipon et al., 2010). Exhumation of the extensional metamorphic complexes occurred in two different stages. A first stage took place from 25 to 15 Ma and involved exhumation through return flow, but with no surface expression (Jolivet et al., 2003; Ring et al., 2010; van Hinsbergen and Schmid 2012). In the second stage, after 15 Ma, the underthrusted nappes reached the surface along major detachment faults (Lister et al., 1999; Jolivet et al., 2003).

During the second exhumation stage, the ongoing extension in the Aegean region was supported by opposite rotation of the NW and the SE parts of the region (van Hinsbergen and Schmid 2012). The recorded 40° clockwise rotation of the NW part is the result of a multistage rotation relative to Moesia platform occurred since 25 Ma (Avigad et al., 1998; Brun and Sokoutis 2010; van Hinsbergen and Schmid 2012). Besides, the SE Aegean portion experienced 30° counterclockwise rotation in respect to the North Menderes Massifs (Northwestern Turkey) (Morris and Anderson 1996; Avigad et al., 1998). These two domains are defined by different orientation of stretching lineations; the NW domain displays NE trending stretching lineations opposed to the N-S trending stretching lineation recorded for the SE part (Walcott and White 1998). In the central Aegean region these two parts are divided by the "MCL", representing the boundary between the two opposite rotating blocks.

Since 25 Ma, the extensional regime in the Aegean region resulted in a total of 400 Km trench perpendicular extension as well as in trench parallel extension related to the opposite rotations of the of the Aegean domains (van Hinsbergen and Schmid 2012). The structures supporting the trench perpendicular extension are located between the non-metamorphic hanging-wall and the exhumed Cycladic metamorphic complexes. On the other hand, trench parallel extension is accommodated along the "MCL". While little is known about its nature and its precise location, it was possible to infer that the total amount of extension along this structure was ~300 km with a total of 650 km trench parallel extension within the south Aegean (van Hinsbergen and Schmid 2012).

This work shed light on the character and the significance of the "MCL" during the post orogenic extension in the Aegean region. Paleomagnetic study performed on the island of Paros indicated that the "MCL" is a top-to-the north detachment fault operated during the late stages of the post-orogenic extension in the upper crustal levels and accommodated a major rotation difference in the island of Paros (see discussion 2.4.3).

Further investigation reveals that the "MCL" cuts through the Cycladic Blueschist Unit, dividing it in two distinct domains determined by different orientation of both stretching lineations and paleomagnetic declinations: the NW and the SE domain. The paleomagnetic declinations for the NW part of Paros agree with available paleomagnetic data from the NW Aegean domain (Morris

and Anderson 1996; Avigad et al., 1998). Similarly, the paleomagnetic directions obtained for the SE part of Paros coincide with the declinations of the SE Aegean block as in Naxos and Milos (Avigad et al., 1998). In addition, the orientations of the stretching lineation on the NW and the SE part of Paros are parallel with the stretching lineation on the corresponding Aegean portions (Walcott and White 1998, Gautier et al., 1993, Avigad et al., 2001). Overall, the NW part of Paros experienced similar rotational history with the NW Aegean domain while the SE part of Paros is part of the counter clockwise rotating SE domain.

The above correlations lead us to the conclusion that the geological picture drawn for the island of Paros is depictive for the boarder Aegean region. Therefore, our kinematic reconstruction on the island of Paros is representative of the kinematic evolution on larger scale within the Aegean region. Taking all the above in consideration, we infer that major clockwise rotation of the NW Aegean domain took place contemporaneously with its exhumation underneath the SE Aegean part. The later rotated in a counter clockwise direction and exhumed under the non-metamorphic Upper Plate along major north dipping detachment faults (e.g North Cycladic Detachment Fault) resulted by trench perpendicular extension. The opposite rotation occurred along the "MCL", which represents the boundary between these blocks and was initiated from an original N-S orientation of both domains. The onset of the opposite rotations of the Aegean portions led to trench parallel extension which in the central Aegean region is accommodated by the "MCL".

To sum up, the "MCL" represents the boundary between the NW and the SE domains of Aegean, corresponding to the NW and the SE parts of the Cycladic Blueschists and accommodates trench parallel extension generated by the opposite rotations of the Aegean blocks (Fig. 4.1).

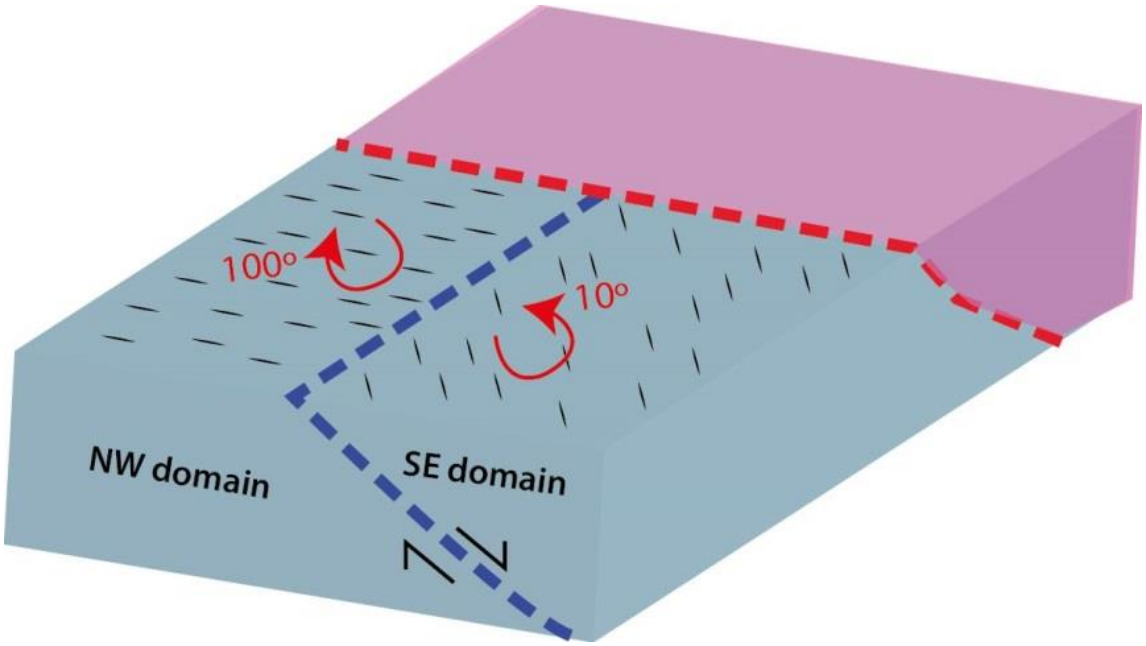

Figure 4.4: Positions of the tectonic blocks in Central Aegean; CBU (blue domain) and Upper plate (purple domain). The blue line separating the CBU corresponds to the "MCL", while the red line represents the Cycladic Detachments Fault Systems (i.e: North Cycladic Detachment System, Central Cycladic Detachment System)

PART 5: CONCLUSIONS

Building up the kinematic evolution of Paros and Aegean along the "MCL" we summarize our main findings in the following conclusions:

- The "MCL" operated after 12-17 Ma during a late stage of post orogenic extension.
- The "MCL" functioned in upper crustal levels in the stability field of the greenschist facies.
- The "MCL" is a top-to-the-North detachment fault dividing the CBU in two distinct domains..
- The "MCL" supported the exhumation of the NW under the SE domain in Paros.
- The "MCL" accommodated a major rotation difference of 100°.
- The "MCL" accommodated the trench parallel extension induced by the opposite rotations of the Aegean domains in a late exhumation stage.

PART 6: FUTURE WORK

Although our study contributed unravelling the kinematics of Aegean region, there is much room for further investigation given the complexity of the area. Thus, we suggest the following future study in order to complete the geological picture for Paros and for the boarder Aegean region.

- Map the "MCL" on the field. Additional structural characteristics might reveal more information about kinematics of the "MCL".

- Date the "MCL" should give information on the onset and the evolution of the trench parallel extension in the Aegean.

- Investigate the detachment faults in the rest of the Aegean showing the same characteristics with the "MCL", to test if they comprise the continuation of that structure. Consequently, it would be achievable to draw the path which that mega-structure followed within the crust. This requires a combined paleomagnetic, structural and petrological study in order to compare and outline both sides of the fault.

- Collect paleomagnetic data along a transection through the SW and the NE Aegean in order to record and define the precise borders of the opposite rotating blocks.

- Geophysical research under the sea level to trace if possible any structure indicative for the boarders of the Aegean blocks

- Production of a map outlining temperature isograds following the example of Robert (1982) but with the use of modern geothermobarometry (more samples are necessary);
- Investigate the PT conditions reached by the NW part of Paros and compare them with the metamorphic evolution in the SE. Even though these two areas belong to the same tectono-metamorphic unit (i.e. Marathi Unit), they are separated by the Mid Cycladic Lineament and therefore they might have slightly different PT path during exhumation,
- This thesis shows that Marathi and Dryos are two distinct tectono-metamorphic unit with different peak assemblages but more investigations are required to precisely estimate the PT conditions reached by Dryos. In addition, the nature of the contact is still enigmatic and it should be investigated in detail,
- Dating the peak metamorphism might add invaluable constraint on the complex tectono-metamorphic evolution of the island of Paros and of the Central Cyclades during post-orogenic exhumation.

REFERENCES

Altherr, R., Kreuzer, H. A. N. S., Wendt, I., Lenz, H., Wagner, G. A., Keller, J., Hohndorf, A. (1982). A late Oligocene/early Miocene high temperature belt in the Attic-Cycladic crystalline complex (SE Pelagonian, Greece). Geologisches Jahrbuch E, 23, 97-164.

Altherr, R., Schliestedt, M., Okrusch, M., Seidel, E., Kreuzer, H., Harre, W., Wagner, G. A. (1979). Geochronology of high-pressure rocks on Sifnos (Cyclades, Greece). Contributions to Mineralogy and Petrology, 70(3), 245-255.

Andriessen, P. A. M., Boelrijk, N. A. I. M., Hebeda, E. H., Priem, H. N. A., Verdurnen, E. T., Verschure, R. H. (1979). Dating the events of metamorphism and granitic magmatism in the Alpine Orogen of Naxos (Cyclades, Greece). Contributions to Mineralogy and Petrology, 69

Avigad, D. (1998). High-pressure metamorphism and cooling on SE Naxos (Cyclades, Greece). European Journal of Mineralogy, 10(6), 1309-1319.

Avigad, D., & Garfunkel, Z. (1991). Uplift and exhumation of high-pressure metamorphic terrains: the example of the Cycladic blueschist belt (Aegean Sea). Tectonophysics, 188(3), 357-372. 3, 215-225.

Avigad, D., Garfunkel, Z., Jolivet, L., Azañón, J. M. (1997). Back arc extension and denudation of Mediterranean eclogites. Tectonics, 16(6), 924-941.

Avigad, D., Ziv, A. and Garfunkel, Z., (2001). Ductile and brittle shortening, extension-parallel folds and maintenance of crustal thickness in the central Aegean (Cyclades, Greece). Tectonics, Vol. 20, Issue: 2, 277–287

Bargnesi, E. A., Stockli, D. F., Mancktelow, N., and Soukis, K. (2013). Miocene core complex development and coeval supradetachment basin evolution of Paros, Greece, insights from (U–Th)/He thermochronometry. Tectonophysics, Vol. 595, 165-182

Bijwaard, H., Spakman, W., & Engdahl, E. R. (1998). Closing the gap between regional and global travel time tomography. Journal of Geophysical Research: Solid Earth (1978–2012), 103(B12), 30055-30078.

Bonneau, M. (1984). Correlation of the Hellenide nappes in the south-east Aegean and their tectonic reconstruction. Geological Society, London, Special Publications, 17(1), 517-527. Papanikolaou, D. J. (1987). Tectonic evolution of the Cycladic blueschist belt (Aegean Sea, Greece). In Chemical transport in metasomatic processes (pp. 429-450). Springer Netherlands.

Brichau, S., U. Ring, R. A. Ketcham, A. Carter, D. Stockli, and M. Brunel (2006).Constraining the long-term evolution of the slip rate for a major extensional fault system in the central Aegean, Greece, using thermochronology. Earth Planetary Science Letter, Vol.241, 293–306

Bröcker, M., & Pidgeon, R. T. (2007). Protolith Ages of Meta-igneous and Metatuffaceous Rocks from the Cycladic Blueschist Unit, Greece: Results of a Reconnaissance U-Pb Zircon Study. The Journal of geology, 115(1), 83-98.

Bröcker, M., and Enders, M. (2001). Unusual bulk-rock compositions in eclogite-facies rocks from Syros and Tinos (Cyclades, Greece): implications for U–Pb zircon geochronology. *Chemical Geology*, *175*(3), 581-603.

Broecker, Michael, and Michael Enders. "U–Pb zircon geochronology of unusual eclogite-facies rocks from Syros and Tinos (Cyclades, Greece)."Geological Magazine 136.02 (1999): 111-118.

Brun, J-P., and Soukoutis, D., (2010). 45 my of Aegean crustal and mantle flow driven by trench retreat. Geology, 38, 815-818

Brun, J. P., & Faccenna, C. (2008). Exhumation of high-pressure rocks driven by slab rollback. Earth and Planetary Science Letters, 272(1), 1-7.

Brun, J. P., Sokoutis, D., Van Den Driessche, J. (1994). Analogue modeling of detachment fault systems and core complexes. Geology, 22(4), 319-322

Buick, I. S. (1991). The late Alpine evolution of an extensional shear zone, Naxos, Greece. Journal of the Geological Society, 148(1), 93-103.

Buick, I. S., & Holland, T. J. B. (1989). The PTt path associated with crustal extension, Naxos, Cyclades, Greece. Geological Society, London, Special Publications, 43(1), 365-369

Deenen, M. H., Langereis, C. G., van Hinsbergen, D. J., Biggin, A. J. (2011). Geomagnetic secular variation and the statistics of palaeomagnetic directions.Geophysical Journal International, 186(2), 509-520.

Dewey, J. F., Helman, M. L., Knott, S. D., Turco E. and Hutton, D. H. W. (1989). Kinematics of the western Mediterranean. Geological Society, London, Special Publications 45, 265-283

Engel, M. and Reischmann, T. (1998). Single zircon geochronology of orthogneisses from Paros, Greece. Bulletin of the Geological Society of Greece, 32, 91–99

Ernst, W. G., and Liu, J. (1998). Experimental phase-equilibrium study of Al-and Ti-contents of calcic amphibole in MORB-A semiquantitative thermobarometer.American Mineralogist, 83, 952-969.

Evelpidou, N., Melini, D., Pirazzoli, P. A. and Vassilopoulos, A., (2013). Evidence of repeated late Holocene rapid subsidence in the SE Cyclades (Greece) deduced from submerged notches. International Journal of Earth Sciences, Vol.103, Issue: 1, 381-395

Faccenna, C. and Becker, T. W., (2010). Shaping mobile belts by small-scale convection. Nature, Vol.465, 602-605

Faccenna, C., Jolivet, L., Piromallo, C., Morelli, A. (2003). Subduction and the depth of convection in the Mediterranean mantle. Journal of Geophysical Research: Solid Earth (1978–2012), 108(B2).

Forster, M. A., & Lister, G. S. (1999). Detachment faults in the Aegean core complex of Ios, Cyclades, Greece. Exhumation processes: Normal faulting, ductile flow and erosion, 154, 305-323.

Forster, M. a., & Lister, G. S. (1999). Detachment faults in the Aegean core complex of Ios, Cyclades, Greece. Geological Society, London, Special Publications, 154(1)

Gautier P. and Brun J. -. P. (1994). Crustal-scale geometry and kinematics of late-orogenic extension in the central Aegean (Cyclades and Ewia Island). Tectonophysics. Vol: 238, Issues : 1-4, 399-424

Gautier P., Brun JP., Jolivet l., (1993) Structure and kinematics of Upper Cenozoic extensional detachment on Naxos and Paros (Cyclades islands, Greece), Tectonics,12, No. 5, 1180-1194.

Gautier, P. and Brun, J.P., (1994). Crustal-scale geometry and kinematics of late-orogenic extension in the central Aegean (Cyclades and Ewia Island). Tectonophysics, Vol: 238, Issues : 1-4, 399-424

Gautier, P., Brun, J. P., Jolivet, L. (1993). Structure and kinematics of upper Cenozoic extensional detachment on Naxos and Paros (Cyclades Islands, Greece). Tectonics, 12(5), 1180-1194.

Gautier, P., M. Ballevre, J.P. Brun, and L. Jolivet, (1989). Extension ductile et bassins mio-pliocenes sur Naxos et Paros (Cyclades). Seance Spec. Soc. Geol. France," Thetys",p 25

Gautier, P., M. Ballevre, J.P. Brun, and L. Jolivet, (1990). Extension ductile et bassins sedimentaires mio-pliocenes dans les Cyclades (les de Naxos et Paros). C. R. Acad. Sci. Paris, 310, 147-153,

Holland, T., and Blundy, J. (1994). Non-ideal interactions in calcic amphiboles and their bearing on amphibole-plagioclase thermometry. Contributions to Mineralogy and Petrology, 116(4), 433-447.

Jackson, J. (1994). Active tectonics of the Aegean region. Annual Review of Earth and Planetary Sciences, 22, 239-271.

Jansen h. B. D. and Schuiling R. D. 1976. Metamorphism oin Naxos: petrology and geothermal gradients. American Journal of Science, 276, 225-1253

Jansen, H.B.D. and Schuiling, R.D., (1976). Metamorphism oin Naxos: petrology and geothermal gradients. American Journal of Science, Vol.276, 1225-1253

Jelikek, V., (1977). The statistical theory of measuring of magnetic susceptibility of rocks and its applications. Geofyzika, Brno, pp 87

Jolivet L., Famin V., Mehl C., Perra T., Aubourg C., Hebert R., Phillipot P. 2004. Strain Localization during crustal – scale boudinage to form extensional metamorphic domes in the Aegean Sea., in Whitney D.I., Teyssier C., Siddoway

C. S., Gneiss domes in orogeny: Boulder, Colorado, Geological Society of America, Special Paper 380, pp: 185-210

Jolivet, L. and Brun, J – P., (2010). Cenozoic geodynamic evolution of the Aegean. Int J Earth Sci (Geol Rundsch), Vol.99, 109–138

Jolivet, L., De Lamotte, D. F., Mascle, A., & Séranne, M. (1999). The Mediterranean basins: Tertiary extension within the Alpine orogen—An introduction. Geological Society, London, Special Publications, 156(1), 1-14.

Keay, S., Lister, G., & Buick, I. (2001). The timing of partial melting, Barrovian metamorphism and granite intrusion in the Naxos metamorphic core complex, Cyclades, Aegean Sea, Greece. Tectonophysics, 342(3), 275-312.

Keiter, M., Piepjohn, K., Ballhaus, C., Lagos, M., & Bode, M. (2004). Structural development of high-pressure metamorphic rocks on Syros island (Cyclades, Greece). Journal of Structural Geology, 26(8), 1433-1445.

Kilias A., Frisch W., Avgerinas A., Dunkl I., Falalakis G.., Gawlick H. J. (2010). Alpine architecture and kinematics of deformation of the northern Pelagonian nappe pile in the Hellenides. Austrian Journal of Earth Sciences Vol 103/1, Vienna, 4 – 28

Kirschvink, J. L. (1980). The least-squares line and plane and the analysis of palaeomagnetic data. *Geophysical Journal International*, *62*(3), 699-718.

Kissel, C., & Laj, C. (1988). The Tertiary geodynamical evolution of the Aegean arc: a paleomagnetic reconstruction. Tectonophysics, 146(1), 183-201.

Kissel, C., Laj, C., Poisson, A., & Görür, N. (2003). Paleomagnetic reconstruction of the Cenozoic evolution of the Eastern Mediterranean. Tectonophysics, 362(1), 199-217.

Lacombe, O., Jolivet, L., Le Pourhiet, L., Lecomte, E., & Mehl, C. (2013). Initiation, geometry and mechanics of brittle faulting in exhuming metamorphic rocks: insights from the northern Cycladic islands (Aegean, Greece). Bulletin de la Société Géologique de France, 184(4-5), 383-403. Extension

Laurent, V., Beaudoin, A., Jolivet, L., Arbaret, L., Augier, R., Rabillard, A., & Menant, A. (2015). Interrelations between extensional shear zones and synkinematic intrusions: The example of Ikaria Island (NE Cyclades, Greece).*Tectonophysics*.

Lee, J., and Lister, G. S. (1992). Late Miocene ductile extension and detachment faulting, Mykonos, Greece. Geology, 20(2), 121-124.

Lister, G.S. et al., 1982. Metamorphic core complexes of Cordilleran type in the Cyclades , Aegean Sea, Greece., 221–225.

Mehl, C., Jolivet, L. and Lacombe, O., (2005). From ductile to brittle: Evolution and localization of deformation below a crustal detachment (Tinos, Cyclades, Greece). Tectonics, Vol.24, TC4017, doi:10.1029/2004TC00176

Morris, A., and Anderson, M. (1996). First palaeomagnetic results from the Cycladic Massif, Greece, and their implications for Miocene extension directions and tectonic models in the Aegean. Earth and Planetary Science Letters, 142(3), 397-408.

Mullender, T. A. T., Van Velzen, A. J., Dekkers, M. J. (1993). Continuous drift correction and separate identification of ferrimagnetic and paramagnetic contributions in thermomagnetic runs. *Geophysical Journal International*,*114*(3), 663-672.

Okrusch, M., & Bröcker, M. (1990). Eclogites associated with high-grade blueschists in the Cyclades archipelago, Greece; a review. European Journal of Mineralogy, 2(4), 451-478.

Okrusch, M., & Bröcker, M. (1990). Eclogites associated with high-grade blueschists in the Cyclades archipelago, Greece; a review. European Journal of Mineralogy, 2(4), 451-478.

Papanikolaou, D.J., (1977). On the structural geology and tectonics of Paros Island (Aegean Sea), Annales geologiques des Pays helleniques, Vol.28, 450-464

Papanikoloau, D.J., (2009) Timing of tectonic emplacement of the ophiolites and terrane paleogeography in the Hellenides. Volume 108, Issues 1–4, 262–280

Parra, T., Vidal, O., Jolivet, L. (2002). Relation between the intensity of deformation and retrogression in blueschist metapelites of Tinos Island (Greece) evidenced by chlorite–mica local equilibria. Lithos, 63(1), 41-66.

Pe-Piper, G., and Piper, D. J. (2001). Late Cenozoic, post-collisional Aegean igneous rocks: Nd, Pb and Sr isotopic constraints on petrogenetic and tectonic models. Geological Magazine, 138(06), 653-668.

Pe-Piper, G., and Piper, D. J. W. (2005). The South Aegean active volcanic arc: relationships between magmatism and tectonics. Developments in Volcanology,7, 113-133.

Pe–Piper, G., Piper, D. J. W., Matarangas, D., (2002). Regional implications of geochemistry and style of emplacement of Miocene I-type diorite and granite, Delos, Cyclades, Greece. Lithos, Vol.60, 47 – 66

Philippon, M., Brun, J. P., Gueydan, F. (2012). Deciphering subduction from exhumation in the segmented Cycladic Blueschist unit (Central Aegean, Greece). Tectonophysics, 524, 116-134.

Ravna, K. (2000). The garnet–clinopyroxene Fe2+–Mg geothermometer: an updated calibration. *Journal of metamorphic Geology*, *18*(2), 211-219.

Ring, U., Gessner, K., Güngör, T., & Passchier, C. W. (1999). The Menderes Massif of western Turkey and the Cycladic Massif in the Aegean—do they really correlate?. Journal of the Geological Society, 156(1), 3-6.

Ring, U., Glodny, J., Will, T., & Thomson, S. (2010). The Hellenic subduction system: high-pressure metamorphism, exhumation, normal faulting, and large-scale extension. *Annual Review of Earth and Planetary Sciences*, *38*, 45-76.

Ring, U., Will, T., Glodny, J., Kumerics, C., Gessner, K., Thomson, S., ... & Drüppel, K. (2007). Early exhumation of high-pressure rocks in extrusion wedges: Cycladic blueschist unit in the eastern Aegean, Greece, and Turkey.*Tectonics*, *26*(2).

Robert, E., (1982). Contribution a l'etude geologique des Cyclades (Greece): l'ile de Paros, these de Doctorat,103 pp., Paris-Sud (Orsay)

Sanchez-Gomez, M., Avigad, D. and Heimman, A., (2002). Geochronology of clasts in allochthonous Miocene sedimentary sequences on Mykonos and Paros Islands: implications for back-arc extension in the Aegean Sea. Journal of the Geological Society, Vol.159, 45-60

Schliestedt, M., Altherr, R., & Matthews, A. (1987). Evolution of the Cycladic crystalline complex: petrology, isotope geochemistry and geochronolgy. In Chemical transport in metasomatic processes (pp. 389-428). Springer Netherlands.

Soukis, K. and Stockli, D., (2013). Structural and thermochronometric evidence for multi-stage exhumation of southern Syros, Cycladic islands, Greece. Tectonophysics, Vol: 595-596, 148-164

Stouraiti, C., Mitropoulos, P., Tarney, J., Barreiro, B., McGrath, A. M., Baltatzis, E. (2010). Geochemistry and petrogenesis of late Miocene granitoids, Cyclades, southern Aegean: Nature of source components. Lithos, 114(3), 337-352.

Taymaz, T., Jackson, J., & McKenzie, D. (1991). Active tectonics of the north and central Aegean Sea. Geophysical Journal International, 106(2), 433-490.

Tirel, C., Gautier, P., Van Hinsbergen, D. J. J., Wortel, M. J. R. (2009). Sequential development of interfering metamorphic core complexes: numerical experiments and comparison with the Cyclades, Greece. Geological Society, London, Special Publications, 311(1), 257-292.

Trotet, F., Jolivet, L., Vidal, O. (2001). Tectono-metamorphic evolution of Syros and Sifnos islands (Cyclades, Greece). Tectonophysics, 338(2), 179-206.

Urai, J. L., Schuiling, R. D., Jansen, J. B. H. (1990). Alpine deformation on Naxos (Greece). Geological Society, London, Special Publications, 54(1), 509-522.

Van der Maar, P. A., Feenstra, A., Manders, B., Jansen, J. B. H. (1981). The petrology of the island of Sikinos, Cyclades, Greece, in comparison with that of the adjacent island of I05. Neues Jahrb. Mineral. Monatsh, 10, 469.

Van Hinsbergen, D.J.J. and Schmid, S.M., 2012. Map view restoration of Aegean-West Anatolian accretion and extension since the Eocene. Tectonics, 31(5),

Van Hinsbergen, D.J.J., Hafkenscheid, E., Spakman, W., Melenkamp, J.E. and Wortel, R., (2005). Nappe stacking resulting from subduction of oceanic and continental lithosphere below Greece. Geology, Vol.33, pp:325-328

Vandenberg, L. C., and Lister, G. S. (1996). Structural analysis of basement tectonites from the Aegean metamorphic core complex of Ios, Cyclades, Greece. Journal of Structural Geology, 18(12), 1437-1454.

Vanderhaeghe, O. (2004). Structural development of the Naxos migmatite dome. SPECIAL PAPERS-GEOLOGICAL SOCIETY OF AMERICA, 211-228.

Vanderhaeghe, O., Hibsch, C., Siebenaller, L., Duchêne, S., de St Blanquat, M., Kruckenberg, S., Fotiadis, A. and Martin, L. 2007. Penrose Conference - Extending a Continent - Naxos Field Guide. In: (Eds.) Gordon Lister, Marnie Forster, and Uwe Ring, Inside the Aegean Metamorphic Core Complexes,Journal of the Virtual Explorer, Electronic Edition, ISSN 1441-8142, volume 27, paper 4, doi:10.3809/jvirtex.2007.00175

Walcott C.R. And White S.H. (1998), Constraints on the kinematics of post -orogenic extension imposed by stretching lineations in the Aegean region, Tectonopysics, 298, pp: 155-175.

Whitney, D. L., and Evans, B. W. (2010). Abbreviations for names of rock-forming minerals. *American mineralogist*, *95*(1), 185.

Wijbrans, J. R., & McDougall, I. (1988). Metamorphic evolution of the Attic Cycladic Metamorphic Belt on Naxos (Cyclades, Greece) utilizing 40Ar/39Ar age spectrum measurements. Journal of Metamorphic Geology, 6(5), 571-594.

Wijbrans, J. R., Schliestedt, M. and York, D., (1990). Single grain argon laser probe dating of phengites from the blueschist to greenschist transition on Sifnos (Cyclades, Greece). Contributions to Mineralogy and Petrology, Vol: 104, Issue 5, 582-593

Wijbrans, J. R., Van Wees, J. D., Stephenson, R. A., and Cloetingh, S. A. P. L. (1993). Pressure-temperature-time evolution of the high-pressure, metamorphic complex of Sifnos, Greece. Geology, 21(5), 443-446.

APPENDIX

Microprobe line scans

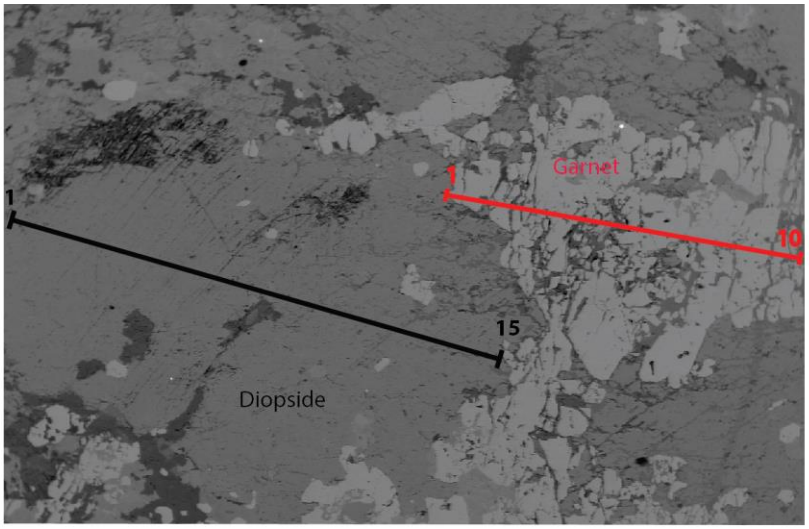

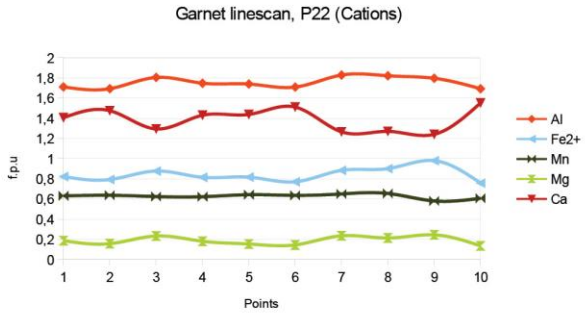

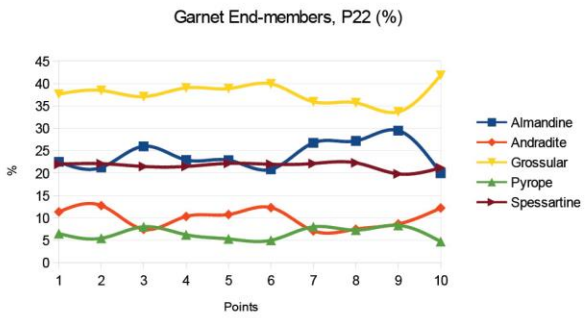

	1	2	3	4	5	6	7	8	9	10
SiO2	37,38	37,24	37,56	37,46	37,34	37,05	37,39	37,32	37,40	37,09
TiO2	0,14	0,15	0,09	0,11	0,11	0,16	0,08	0,09	0,11	0,12
Al2O3	17,74	17,55	18,90	18,25	18,11	17,68	19,18	19,08	18,84	17,41
FeO	15,32	15,32	15,16	15,06	15,17	14,84	15,21	15,56	17,10	14,50
MnO	9,18	9,28	9,15	9,13	9,39	9,24	9,55	9,60	8,54	8,77
MgO	1,55	1,30	1,94	1,51	1,28	1,20	1,97	1,78	2,04	1,11
CaO	16,17	16,99	15,00	16,57	16,61	17,36	14,69	14,73	14,42	17,73
Na2O	0,00	0,00	0,01	0,02	0,01	0,02	0,00	0,00	0,00	0,02
Cr2O3	0,01	0,00	0,00	0,00	0,00	0,00	0,02	0,02	0,01	0,03
F2O	0,00	0,00	0,00	0,00	0,00	0,00	0,26	0,34	0,00	0,00
NiO	0,01	0,00	0,00	0,00	0,01	0,01	0,02	0,00	0,01	0,00
Sum	97,50	97,82	97,81	98,11	98,02	97,55	98,37	98,53	98,46	96,78
Almandine	22,5	21,2	26,0	22,9	22,9	20,8	26,8	27,2	29,5	20,0
Andradite	11,4	12,8	7,5	10,3	10,8	12,3	7,1	7,5	8,6	12,2
Grossular	37,6	38,4	37,1	39,0	38,9	39,9	35,9	35,7	33,7	41,8
Pyrope	6,5	5,5	8,0	6,2	5,3	5,0	8,0	7,3	8,3	4,7
Spessartine	22,0	22,1	21,5	21,5	22,2	22,0	22,1	22,3	19,8	21,2
Uvarovite	0,0	0,0	0,0	0,0	0,0	0,0	0,1	0,1	0,0	0,1

Thin section P21
Linescans "lnscP21"

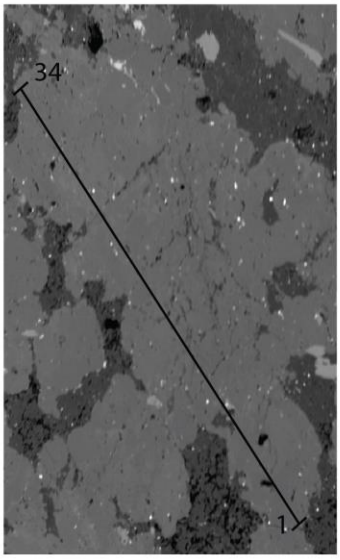

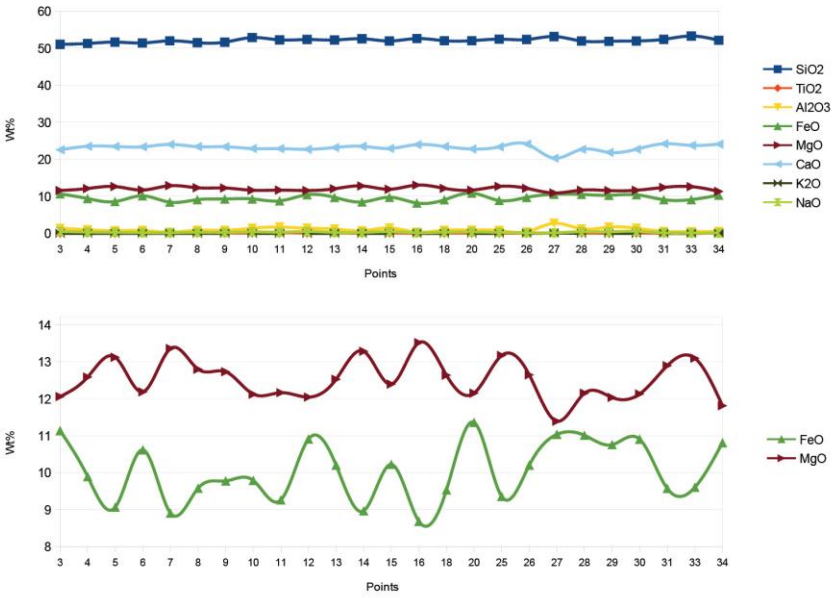

POINT	SiO2	TiO2	Al2O3	FeO	MgO	CaO	K2O	NaO	Cr2O3	sum
1	50,86	0,04	0,51	9,80	11,24	23,82	0,00	0,15	0,05	96,48
2	50,54	0,10	1,63	9,79	11,29	22,56	0,00	0,37	0,00	96,28
3	51,00	0,06	1,35	10,63	11,56	22,51	0,00	0,49	0,04	97,65
4	51,23	0,12	0,96	9,39	12,08	23,48	0,00	0,36	0,04	97,66
5	51,61	0,04	0,68	8,56	12,62	23,44	0,00	0,26	0,02	97,23
6	51,37	0,09	0,77	10,11	11,68	23,32	0,00	0,19	0,08	97,62
7	51,96	0,02	0,31	8,40	12,85	24,00	0,00	0,15	0,04	97,74
8	51,46	0,08	0,82	9,07	12,30	23,39	0,00	0,28	0,01	97,41
9	51,58	0,06	0,80	9,27	12,23	23,37	0,00	0,25	0,03	97,59
10	52,83	0,11	1,36	9,28	11,62	22,87	0,00	0,41	0,04	98,53
11	52,20	0,17	1,70	8,76	11,66	22,85	0,00	0,31	0,04	97,69
12	52,30	0,11	1,36	10,41	11,54	22,66	0,00	0,49	0,03	98,90
13	52,17	0,11	1,15	9,70	12,02	23,14	0,00	0,24	0,03	98,57
14	52,52	0,04	0,67	8,46	12,78	23,49	0,00	0,23	0,01	98,21
15	51,91	0,11	1,44	9,72	11,89	22,89	0,00	0,46	0,06	98,48
16	52,56	0,02	0,32	8,18	13,01	23,94	0,00	0,17	0,03	98,23
17	51,04	0,07	1,18	9,13	12,19	22,61	0,00	0,20	0,06	96,48
18	51,99	0,06	0,83	9,03	12,13	23,44	0,00	0,30	0,02	97,80
19	50,24	0,03	2,68	9,10	11,78	19,91	0,00	0,19	0,07	94,00
20	51,99	0,07	0,88	10,86	11,65	22,76	0,00	0,40	0,05	98,65
21	48,70	0,37	4,88	13,85	10,42	18,94	0,00	1,22	0,07	98,46
22	46,16	0,04	0,57	8,20	10,44	20,12	0,00	0,12	0,02	85,67
23	49,70	0,03	6,82	8,25	8,31	21,70	0,00	0,31	0,04	95,15
24	37,07	0,08	1,42	3,02	10,40	28,10	0,03	0,07	0,05	80,25
25	52,39	0,06	0,77	8,85	12,67	23,34	0,00	0,26	0,02	98,35
26	52,31	0,03	0,39	9,70	12,14	24,09	0,00	0,12	0,02	98,80
27	53,11	0,04	2,71	10,53	10,89	20,28	0,11	0,14	0,06	97,86
28	51,91	0,10	1,21	10,51	11,65	22,65	0,00	0,44	0,03	98,49
29	51,82	0,04	1,68	10,25	11,53	21,84	0,00	0,42	0,02	97,60
30	51,92	0,10	1,36	10,40	11,63	22,68	0,00	0,55	0,02	98,66
31	52,35	0,03	0,50	9,07	12,39	24,16	0,00	0,12	0,06	98,69
32	50,80	0,08	1,51	9,95	10,39	22,54	0,00	0,23	0,07	95,56
33	53,24	0,02	0,46	9,10	12,59	23,73	0,00	0,09	0,04	99,28
34	52,10	0,04	0,47	10,31	11,31	24,08	0,00	0,10	0,00	98,40

Thin section P21
Diopside

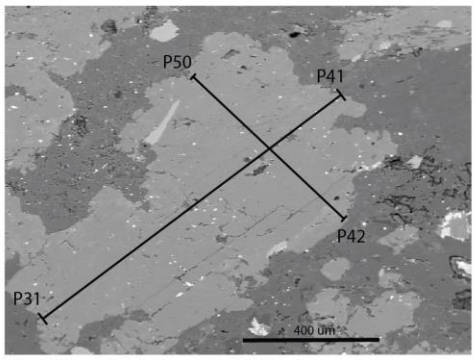

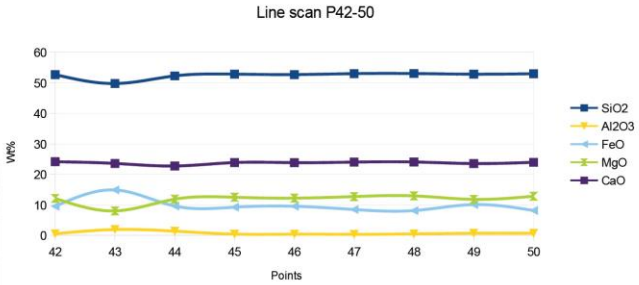

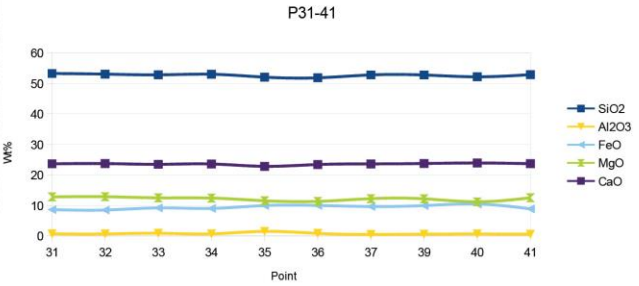

POINTS	SiO2	TiO2	Al2O3	Cr2O3	FeO	MnO	MgO	CaO	NaO	K2O	F2O	NIO	SUM
31	53,26	0,04	0,72	0,09	8,64	0,34	12,82	23,64	0,26	0,00	0,24	0,06	100,11
32	53,05	0,05	0,69	0,06	8,51	0,31	12,88	23,73	0,22	0,00	0,00	0,02	99,52
33	52,82	0,10	0,90	0,07	9,21	0,35	12,51	23,49	0,27	0,00	0,31	0,00	100,01
34	53,01	0,04	0,70	0,03	9,04	0,36	12,43	23,60	0,24	0,00	0,12	0,00	99,58
35	52,06	0,16	1,53	0,02	9,98	0,34	11,55	22,83	0,39	0,00	0,00	0,01	98,86
36	51,84	0,11	0,86	0,03	10,01	0,33	11,35	23,42	0,14	0,00	0,08	0,00	98,16
37	52,79	0,03	0,50	0,01	9,67	0,35	12,24	23,63	0,17	0,00	0,31	0,02	99,71
39	52,76	0,08	0,61	0,03	9,96	0,33	12,19	23,76	0,18	0,00	0,00	0,00	99,91
40	52,17	0,05	0,66	0,04	10,48	0,38	11,21	23,93	0,16	0,00	0,00	0,03	99,12
41	52,88	0,05	0,61	0,02	8,89	0,34	12,53	23,70	0,19	0,00	0,00	0,00	99,22
42	52,70	0,05	0,54	0,04	9,54	0,40	12,13	24,14	0,15	0,00	0,00	0,00	99,69
43	49,78	0,23	1,92	0,04	14,90	0,45	8,03	23,58	0,15	0,00	0,00	0,01	99,10
44	52,28	0,10	1,40	0,04	9,63	0,28	11,87	22,75	0,45	0,00	0,20	0,03	99,03
45	52,86	0,04	0,43	0,02	9,25	0,35	12,50	23,87	0,16	0,00	0,28	0,00	99,75
46	52,71	0,05	0,40	0,01	9,54	0,38	12,22	23,84	0,14	0,00	0,21	0,00	99,50
47	53,02	0,03	0,35	0,01	8,48	0,35	12,73	24,02	0,11	0,00	0,01	0,01	99,13
48	53,05	0,04	0,49	0,07	8,14	0,37	12,95	24,06	0,13	0,00	0,00	0,00	99,29
49	52,85	0,04	0,71	0,06	10,11	0,37	11,81	23,54	0,36	0,00	0,33	0,00	100,18
50	52,98	0,08	0,71	0,06	8,16	0,33	12,84	23,95	0,20	0,00	0,00	0,00	99,30

Appendix 3.2

Thin sections description and paragenetic diagrams

Sample	Mineralogy	Notes-description
4	Chl, Ep, Bt, Qz, Feld (Cpx?), Cal, Ab	This sample is composed by 90% fine grained ground mass. Angular and very fine grained crystals. Porphyroclasts of epidote are broken in squared pieces and filled with an assemblage of Chl. The matrix is mainly composed by Chl. Lenses of deformed Qz recrystallize at the rim in finer grained crystals (Cpx crystals with small size, deformed and angular)
5	Bt, ms, Qz, St (?), Chl, Ep	Well defined foliation defined by coarse grained and elongated Ms and Bt and oriented. Deformed lenses of Qz are wrapped by mica (Ms and Bt).
6	Cal, Qz	That rock sample is banded and composed mainly by Cal and Qz. Cal is coarse grained showing thin twins of type I, while quartz is finer grained and showing a slight preferential orientation.
7	Feld, Grt, Bt, Qz Chl	Thin section formed by alternating bands of only Bt or Bt and Chl in quartzo-feldspatic layers. Big porphyroclasts of garnet are deformed and broken in several angular pieces and filled with Qz, Bt and Chl all along its fractures. Occasional inclusions of muscovite can be found within the Grt. Pl and Bt wraps around the garnet. Two generations of Qz can be observed: 1) one coarse grained, randomly oriented and one medium to fine grained slightly foliated. Deformed crystals of quartz are wrapped by Bt and Chl and they contain straight inclusions either parallel or at an angle with respect the wrapping foliation. Muscovite, where present, is medium sized, deformed (undulatory extinction and bended) with grain boundaries corroded and surrounded by fine grained crystals of Bt.
8	Amp, Qz, Feld, Scp, Cpx, Ep, Cal	Fine grained foliated rock with a matrix composed by 40% of Qz and Feld. Cpx is coarse grained and always with a reaction rim around (composed by the fine grained aggregates). Scapolite display straight boundaries with feldspar but it seems not stable with Pl. Ep formation overprint previous crystals and fabrics. Hornblende not stable with feldspar. Minor calcite with irregular shape. (pseudomorphs of maybe Cpx - (hexagonal shape) but in fine grain aggregates.)
9	Feld, Qz, Bt	Highly altered and deformed. It contains large crystals of Feld, QZ and Cal. Qz display undoluse extinction and is generally highly deformed. Occasionally, very fine grained layers of Bt wraps around fine grained aggregates of Feld, alternating bands composed of Qz and Feld.
10	Cal (60- 70%), Grt, Amp, Cpx Scp, Bt	The sample is mainly composed by coarse grained Cal showing well developed twinning. Crystals of garnet are broken and strongly fractured with the development of a micro crystalline-greenish aggregate of green minerals. Its fractures are filled with Feld and Cpx. Crystals of green Hbl are medium to coarse grained, displaying a preferential orientation. Bt is generally fine grained and randomly oriented. Cpx is medium to coarse grained.
11	Cal, Scp, Cpx, Qz Bt, Ep	Elongated Ep with irregular grain boundaries. Crystals of calcite are coarse grained exposing thick twins of type II. Scp is coarse grained. Cpx is coarse grained with irregular grain boundaries (not deformed but with gulfs). Crystals of Bt are small and randomly orientated. Qz is coarse grained and has straight boundaries. Cpx has the same preferential orientation as quartz.
12	Cal, Scp, Amp, Cpx, Feld	Recognizable foliation within bands alternating layers mainly composed of 1) Coarse grained Cal (around 60%) and grains of Scp. Cal forms thick twins of type II and III. 2) Green amphiboles define the foliation. Crystals of amphibole are elongated and appear in bands showing irregular grain boundaries. Clinopyroxene is coarse grained and broken.

13	Amp, Feld, Cpx,	Slightly foliated sample defined by slightly elongated crystals of amphibole. Crystals of Pl are medium grained and equidimensional. Cpx can be recognized from the shape and the birefringent colors
14	Amp, Pl, Qz	-Slightly foliated and banded rock with green amphibole oriented, medium grained plagioclase. Aggregates of green amphibole and plagioclase are clustered together after a previous mineral (pseudomorphose).
15	Feld, Qz, Bt	Foliation is defined by elongated Bt which is bended and wraps around Feld. Plagioclase is big and defined by twins and mirmikite structures. Similar to P16 but the plagioclases are coarser.
16	Feld, Qz, Bt, Amp, opaque	-Feld crystals are euhedral and equidimensional (in many cases kaolinised) and displays clear twinning. Qz is fine grained and deformed, whereas Bt and green Amp are elongated defining the foliation in thin layers (they are not deformed)
17	Feld, Qz Bt, Ms	Foliated rock with equidimensional grain size in which coarse grained rounded Pl have straight boundaries, crystals of Qz and Bt wraps around the Feld. Pl contains random inclusions of white mica not deformed; some of them show a slight zoning and their diameter can reach 0.5 cm. Qz is slightly deformed.
18	Pl, Amp, Bt	Well defined foliation defined by coarse grained Pl (clear zoning pattern) and Amp
19	Pl, Amp, Bt, Qz Chl, Ep	Well defined foliation defined by coarse grained Pl and Amp with minor Qz and Bt is oriented showing straight boundaries. Crystals of Chl and Ep cut Qz crystals. They seem to be formed in the later stage. Medium grained rounded equidimensional crystals of Feld can be found in a fine grained matrix of Qz (deformed showing undoluse extinction) NOTES: the impression is that the Amphibole is about to be replaced by biotite. Hence they are not stable together.
20	Cal (80%), Amp Qz, Scp, Amp, Feld	Alterning layers richer in calcite or amphibole/pyroxene.-Coarse grained calcite shows twins of Type iii whereas green Hbl is clearly oriented.
21	Pl (30%), amp (70%) Cpx	Well defined foliation defined by coarse grained Pl and medium grained Amp with Cpx not oriented, showing reaction rims with amp. It contains oriented inclusions of Amp and has no straight boundaries.
22	Grt, Kfs, Pl, Qz, amp, Scp Spn, mag, ep, Cal, Chl	Qz: crystals with preferential orientations and undoluse extinction. In two generations; one fine grained fills the fractures of garnet; the other one forms veins parallel to the main foliation. Cpx is coarse grained and wrapped by Qz whereas Amp, Chl and Pl are slightly oriented.
24	Pl, Feld, Cal, Cpx, Amp, Scp, Grt Bt, Chl, Ep	Amp is not oriented and the Cpx is anhedral with corroded grain boundaries. Grt is broken and filled with Feld. Scp is medium to coarse grained with straight grain boundaries
26	Qz, Feld, Ms, Cpx (?)	Protomylonitic structures with badly developed foliation defined by Ms (might form after) and Amp surrounding large relics of Cpx. Qz veins are cut by calcite veins
27	Cal, Amp, Qz, Scp, Cpx, Pl	Weak foliation due to the presence of coarse to medium crystals of Cal, Amp, Pl, Cpx and Scp. Cal clusters in bands and is defined by regular grain boundaries and twinning. The green Amp is slightly oriented, elongated and with regular shape and grain boundaries (seems to be stable with Scp but not with Pl). Qz is fine grained and Scp appears in both large grains and smaller grains (recrystallized?). Large grains of Cpx have irregular shape and are not stable with Pl.
28	Amp, Pl	The sample is composed only by Amp and Pl. It is slightly foliated. Amp is elongated along a preferential orientation and has a regular shape. Feldspar are equidimensional and generally medium grained.
29	Cal, Bt, Amp, Scp, Qz, Feld	Bt and Amp define a weak foliation with irregular occurrence of Scp with irregular shape and fine grained Qz (deformed showing undoluse extinction). Large Pl is broken and wrapped by Bt.

32	Scp, Qz, Grt, Cpx, Amp, Feld	Massive rock showing no sign of foliation. Grt is broken and filled with Qz whereas Amp is randomly oriented.
33	Cal, Scp, Bt, Amp, Cpx	Sample defined by compositional bands with clear foliation. Bands are composed by Amp + Bt and Cal+Qz, respectively. Cpx is not stable and shows irregular boundaries (seems not stable with feldspar).
35	Ep, Chl, Cpx (?), Feld, Qz, Bt Cal, Bt	Mylonite to ultramylonite texture (>90% matrix) with matrix composed by very fine grained crystals outlining a well developed foliation. Large Ep are broken and filled with fine grained aggregates. Chl wraps around relics of Cpx (seems to form in a later stage). Feld and Qz grains have straight grain boundaries whereas Bt is fine grained and randomly oriented
	Qz, Bt, Amp, Feld, Ms	Coarse grained, slightly foliated rock with magmatic texture. Coarse grained Feld and Qz along with Bt and Ms. Pl twinning is well developed.
38	Qz, Bt, Amp, Feld, Ms	Rock with clear magmatic texture defined by the presence of large grains of Feld and Pl with straight grain boundaries and euhedral shape (in Qz rich domains). Qz is slightly deformed (undoluse extinction) whereas fine grained Ms and Bt are randomly oriented.

Appendix 3.3

P3

Dryos Unit, Phyllite

Mineral	D1	D2	D3
Plagioclase	--------	x	
Opaque		x	
Muscovite	x	---	
Quartz		x	
Chlorite		x	

P4 Dryos Unit, amphibolite/greenschist

Mineral	D1	D2	D3
Calcite		x	
Feldspar		x	
Epidote	x	x	
Opaque		x	
Pyroxene	X		
Chlorite		x	

P5

Dryos unit, Biotite-muscovite micaschist

Mineral	D1	D2	D3
Feldspar		x	
Biotite		x	
Opaque			
Muscovite		x	
Quartz		x	

P6

Dryos Unit, marble

Mineral	D1	D2	D3
Calcite		x	
Muscovite		x	
Quartz		x	

P7
Marathi unit, micaschist (on the field)?

Mineral	D1	D2	D3
Garnet	x		
Feldspar	x	x	
Muscovite	x		
Chlorite	x	x	
Garnet	x		
Biotite	x	x	
Opaque	x	x	
Muscovite	x		

P8
Marathi Unit, amphibolite

Mineral	D1	D2	D3
Epidote		x	x
Feldspar	x..	x	
Green amphibole		x	
Scapolite		x	
Cpx	X?		
Chlorite			x
Biotite			?
Calcite		x	
Quartz		x	x

P9 Dryos unit

Mineral	D1	D2	D3
Calcite		x	
Feldspar		x	
Epidote			
Biotite		x	
Opaque			
Quartz		x	

P10 Marathi unit

Mineral	D1	D2	D3
Calcite		x	x
Scapolite			x
Feldspar	x	x	
Green amphibole (Hornblende)	x	x	
Clinopyroxene	x		
Garnet	x		
Biotite			x
Opaque		x	
Talc		x	

P11 Marathi Unit

Mineral	D1	D2	D3
Clinopyroxene	x	x	
Scapolite	x	x	x
Quartz	x	x	
Calcite		x	x
Biotite			x
Epidote	x	x	

P12 Marathi Unit

Mineral	D1	D2	D3
Calcite			x
Plagioclase		x	
Scapolite			x
Green amphibole (Hornblende)		x	
Diopside	x	x	
Biotite			x
Biotite			x
Quartz			x

P13 Marathi Unit

Mineral	D1	D2	D3
Plagioclase		x	

Green amphibole (Hornblende)		x	
Pyroxene	?		

P14 Marathi Unit

Mineral	D1	D2	D3
Plagioclase/Scapolite		x	
Epidote			
Green amphibole (Hornblende)		x	
Opaque		x	

P15 Marathi Unit

Mineral	D1	D2	D3
Feldspar		x	------
Biotite		x	
Quartz		?	

P16 Marathi Unit

Mineral	1	2	3
Feldspar		x	
Green amphibole (Hornblende)		x	

P17 Marathi Unit

Mineral	D1	D2	D3
Bt+Ms	x		
Feldspar		x	x
Quartz	x	x	

P20 Marathi Unit

Calcschist. Layer richer in calcite or amphibole/pyroxene

Mineral	D1	D2	D3
Calcite		x	
Feldspar		x	

Epidote		x	
Green amphibole (Hornblende)		x	
Opaque		x	
Scapolite		x	

P21 Marathi Unit

Mineral	D1	D2	D3
Plagioclase	??	x	
Epidote		x	
Green amphibole (Hornblende)		x	
Opaque		x	
Pyroxene	x		

P22 Marathi Unit

Mineral	D1	D2	D3
Calcite	x	x	
K Feldspar	x		
Plagioclase		x	
Epidote	x		
Sphene	x		
Chlorite		x	
Green amphibole (Hornblende)		x	
Garnet	X		
Clinopyroxene	x		
Quartz	x	x	

P24/b Marathi Unit

Mineral	D1	D2	D3
Calcite		x	x
Feldspar	x	x	
Epidote			x
Green amphibole (Hornblende)	x		
scapolite		x	x
Garnet		x	

Biotite			x
Chlorite			x
Pyroxene		x	

P26 Marathi Unit

Mineral	D1	D2	D3
Epidote		x	
Green amphibole		x	
Pyroxene	x	x	
Feldspar		x	
Chlorite		x	
Quartz		x	x
Muscovite			x

P27 Marathi Unit

Mineral	D1	D2	D3
Calcite		x	
Feldspar	x	x	
Epidote			
Green amphibole (Hornblende)		x	
Biotite			x
Opaque			
Pyroxene	x		

P28 Marathi Unit

Mineral	D1	D2	D3
Plagioclase		x	
Epidote		?	
Green amphibole (Hornblende)		x	
Pyroxene	?	x	

P29 Marathi Unit

Mineral	D1	D2	D3

quartz			x
Scapolite		x	x
Calcite			x
Biotite	x	x	
Plagioclase	x	x	
Green hornblende		x	

P32 Marathi Unit

Mineral	D1	D2	D3
Scapolite	x	x	
Feldspar	x		
Green amphibole (Hornblende)		x	
Biotite			x
Clinopyroxene	x		
Quartz	x	x	
Garnet	x		

P33 Marathi Unit

Mineral	D1	D2	D3
Calcite		x	x
feldspar		x	
Epidote?		x	
Green amphibole (Hornblende)		x	
Diopside	x		
Quartz		x	
Biotite		x	x

P35 Marathi Unit

Mineral	D1	D2	D3
Epidote	x	x	
Calcite			x
Clinopyroxene	x		
Feldspar		x	x
Quartz		x	x
Biotite			x
Chlorite	x	x	

P37 Marathi Unit

Mineral	D1	D2	D3
Calcite			
Plagioclase/Scapolite		x	
Epidote		x	
Green amphibole (Hornblende)			
Quartz		x	
Garnet			
Biotite		x	
Opaque			
Muscovite		x	

P38 Marathi Unit

Mineral	D1	D2	D3
Plagioclase		x	
Amphibole		x	
Quartz		x	
Biotite		x	
Muscovite		x	
Pyroxene		x	

Appendix 3.4

Sample	Position	Unit	Lithology	Mineralogy
P001	36º59'31''N 25º13'9''E	Dryos unit	greenschist	chlorite, amphibole
P002	37º59'31''N 25º13'9''E	Dryos unit	greenschist	chlorite, amphibole
P003	36º59'30''N 25º13'10''E	Dryos unit	phyllite	(white) mica, quatrz, chlorite
P004	37º0'15''N 25º12'36''E	Dryos unit	amphibolite	amphibole, chlorite or epidote
P005	37º0'15''N 25º12'36''E	Dryos unit	phyllite	(white) mica, quatrz, chlorite
P006	37º0'15''N 25º12'36''E	Dryos unit	marble	calcite, mica
P007	36º59'5''N 25º11'30''E	Marathi unit	mica shcist	garnet, mica, quartz, feldspar
P008	36º59'1''N 25º10'50''E	Marathi unit	Amphibolite (?)	amphibole and chlorite or epidote
P009	36º59'41''N 25º7'17''E	Dryos unit	phyllite	chlorite, mica, quartz
P010	37º3'29''N 25º10'38''E	Marathi unit	amphibolite	amphibole, plagioclase
P011	37º4'45''N 25º11'59''E	Marathi unit	amphibolite	amphibole, plagioclase
P012	37º4'53''N 25º11'58''E	Marathi unit	amphibolite	amphibole, plagioclase
P013	37º5'4''N 25º12'37''E	Marathi unit	amphibolite	amphibole, plagioclase

P014	37º4'54''N 25º12'40''E	Marathi unit	amphibolite	amphibole, plagioclase
P015	37º3'1''N 25º12'8''E	Marathi unit	amphibolite	amphibole, plagioclase
P016	37º3'1''N 25º12'8''E	Marathi unit	amphibolite	amphibole, plagioclase
P017	37º2'23''N 25º12'33''E	Marathi unit	gneiss	quartz, feldspar, mica, amphibole
P018	37º4'45''N 25º12'49''E	Marathi unit	amphibolite	amphibole, plagioclase
P019	37º2'23''N 25º12'33''E	Marathi unit	amphibolite	amphibole, plagioclase
P020	37º5'54''N 25º13'32''E	Marathi unit	Amphibolite (?)	amphibole, plagioclase
P021	37º66'29''N 25º12'37''E	Marathi unit	amphibolite	amphibole, plagioclase
P022	area of the quarrier	Marathi unit	Amphibolite (?)	amphibole, plagioclase
P023	37º2'32''N 25º9'16''E	Marathi unit	amphibolite	amphibole, plagioclase
P024	37º2'39''N 25º9'35''E	Marathi unit	Amphibolite (?)	amphibole, plagioclase, garnet, chlorite, epidote, quartz
P025	37º1'28''N 25º8'58''E	Marathi unit	Amphibolitic shcist	mica, quartz, garnet, amphibole?
P026	37º01'39''N 25º9'11''E	Marathi unit	amphibolite	epidote, chlorite, garnet, plagioclase, amphibole?
P027	37º01'40''N 25º09'14''E	Marathi unit	greenschist	epidote, chlorite, garnet, plagioclase, amphibole
P028	37º01'36''N 25º09'13''E	Marathi unit	amphibolite	Amphibole, plagioclase.

P029	37º0'26''N 25º09'24''E	Marathi unit	amphibolite	Amphibole, plagioclase.
P031	37º0'38''N 25º10'26''E	Marathi unit	amphibolitic schist	amphibole, plagioclase, garnet, quartz, mica
P032	37º01'02''N 25º10'26''E	Marathi unit	Amphibolite (?)	garnet, plagioclase, amphibole, chlorite, epidote, quartz
P033	37º0'47''N 25º10'26''E	Marathi unit	Amphibolite schist	
P034	37º0'22''N 25º10'36''E	Marathi unit	amphibolitic schist	amphibole, plagioclase, garnet, mica, quartz
P035	37º0'15''N 25º12'36''E	Marathi unit	greenschist	amphibole, plagioclase, chlorite, epidote.
P036	monatiri tou ai giwrgi	Marathi unit	meta-bauxite(?)	
P037	25º11'42''N 37º2'14''E	Marathi unit	migmatite	
P038	25º11'42''N 37º2'14''E	Marathi unit	migmatite	